Regime shift in sediment concentrations in the Loire estuary

R.J.A. de Goede

TU Delft

Deltares
Enabling Delta Life

REGIME SHIFT IN SEDIMENT CONCENTRATIONS

IN THE LOIRE ESTUARY

by

Roel Johannes Antonius DE GOEDE

to obtain the degree of Master of Science,
at the Delft University of Technology,
to be defended publicly on Thursday February 6, 2020 at 15:30.

Student number: 4382064

Thesis committee:		
	Prof. dr. ir. Z.B. Wang,	TU Delft, chair professor
	Dr. ir. B.C. van Prooijen,	TU Delft, assistant professor
	Dr. ir. Y. Dijkstra,	TU Delft, daily supervisor

An electronic version of this thesis is available at
http://repository.tudelft.nl/

Cover photo: Nantes et l'estuaire de la Loire, ©ImaginEarth.

ACKNOWLEDGEMENTS

By handing in this MSc thesis, an end will come to my life as a student, which comprises the past 5.5 years of my life. Before you start reading the work which concludes my MSc studies in Hydraulic engineering, I would like to use this opportunity to express my gratitude to everyone who, deliberately or not, contributed to my thesis or simply made my student life as fantastic as it was.

More than a year ago, I received an e-mail from Bram van Prooijen whether I was interested in writing my master thesis about hyperturbidity in the Loire, under supervision of Yoeri Dijkstra. Although I still had to start my 5-month internship at Royal HaskoningDHV, I decided to have a little chat with Yoeri. His tremendous enthusiasm (and of course my interest in sediment dynamics) formed the start of what eventually resulted in this thesis. Yoeri, I owe you a big thank you for the weekly sessions, constructive feedback (even during your holidays) and your endless positivity at moments when I doubted the results. This master thesis would not have been the same without your contributions, and I really enjoyed working with you. I would like to thank the other members of my graduation committee, Bram van Prooijen and Zheng Bing Wang, for their constructive feedback and critical questions during the progress meetings. Your refreshing insights especially improved the comprehensiveness of the report. And Bram in special, I would like to thank you for your faith in me as a researcher when you put me up for this project. In addition, I would like to thank the people at Deltares for providing a working environment in which I was able to get the most out of this project.

Furthermore, I would like to thanks my fellow students at Deltares. Day after day lunching at noon followed by a 'bakkie koffie' was always something to look forward to. Sometimes you just need to share the problems you face, and what is better than sharing them with people that face similar problems. Of course, sharing problems was only minor part of the lunch, where mainly a lot of nonsense was discussed. I really enjoyed it guys!

I would also like to thank my other friends from Delft. Most of you, I have known since the first year's introduction weeks. Over the last few years, we have experienced and done a lot together: from making assignments together (especially COZ in the first year) to multiple trips we made together (and of course when you visited me in Munich). I hope that we continue our tradition in the last weekend of August, despite the fact that a working life is waiting for me, and I can't wait to see you guys graduating as well!

Last but not least, I would like to thank my family and friends from back home (Papendrecht). I owe many thanks to my parents for their love, faith and support, which all contributed to the carefree student life I had. I would like to thank my brother and sister for always being there for me. And finally, I would like to thank my friends for all the fun time we had over the last years. It is nice to know that there is always someone there for you in good and in hard times.

In front of you is the report that concludes my time in Delft. I have had a great time being a student at the TU Delft, including an extraordinary exchange semester in Munich. But now, the time has come to enter the next phase of my life and to start exploring the field of hydraulic engineering in the real world. Enjoy reading!

R.J.A. (Roel) de Goede
Delft, January 2020

CONTENTS

SUMMARY

An estuary is often defined as a semi-enclosed coastal body of water, freely connected with the open sea, in which sea water is measurably diluted by fresh water derived from land drainage (Pritchard, 1967). Some of the largest ports around the world are located within estuaries. Over the last century, narrowing and deepening operations have taken place to allow bigger ships to reach these ports. In the Loire (France) estuary, a significant increase in tidal range and a dramatic increase of suspended sediment concentrations have been observed along with the ongoing narrowing and deepening of the estuary. Suspended sediment concentrations in estuaries often have local maxima, also called estuarine turbidity maxima (ETMs). The dramatic increase in sediment concentrations in these ETMs is often referred to as a regime shift towards a hyperturbid state. While it is generally accepted that the increase in tidal range is a consequence of deepening and narrowing, it is not clear whether deepening is a potential cause for the hyperturbidity observed in the Loire.

The goal of this research was to investigate the role that deepening of the Loire estuary played in the observed regime shift to a hyperturbid state. To be able to perform a model study, data from many sources and decades has been brought together into a literature study. Although very little observations of sediment concentrations have been reported over the 20th century, literature clearly shows that sediment concentrations increased drastically over the years. The scarcity of data not only applied for the sediment concentrations over the years, but also for bathymetry and hydrodynamics, resulting in uncertainty about the historical states of the estuary. To cope with the large range of uncertainty and variability in the reported observations and model parameters, an idealised model called iFlow has been used. The strength of the iFlow model for this research was twofold. Firstly, iFlow allowed to investigate the essential physical processes driving the estuarine sediment dynamics in isolation, which contributes to actually understand the observed changes. Secondly, iFlow is computationally efficient, allowing to perform extensive sensitivity studies. This way, we could determine which processes play a role in the current state of the Loire estuary and how they are affected by deepening. Furthermore, by mapping the effects of the uncertainty on the different physical processes, robust conclusions could be drawn about the effects of deepening despite the given uncertainty.

The results of this research consist of two parts. At first, an iFlow model was set-up to describe the current state of the Loire estuary. Regarding the sediment dynamics in the Loire, distinction is made between the along-channel sediment transport and local resuspension. The transport capacity, the sediment transport that would occur if there was plenty of sediment on the bed everywhere along the estuary, is used to evaluate the importance of different along-channel processes. The sum of the contributions due to the different physical processes is called the total transport capacity. The along-channel sediment transport in the Loire is governed by the importing contributions due to a baroclinic pressure gradient and tidal asymmetry induced by an external M_4 tide, an exporting contribution induced by the river and an along-channel varying contribution due to spatial settling lag. Both importing contributions got amplified once sediment-induced turbulence damping is of importance, whereas the exporting contributions remain equal. Results have shown that fine sediments are most likely imported during neap tide. In this research, local resuspension is assumed sufficiently high to be able to model the observed sediment concentrations.

Secondly, the effects of deepening on the physical processes have been assessed. This was done by only varying the depth of the model. Although deepening sometimes locally resulted in an increased exporting contribution due to one of the physical processes, it generally resulted in enhanced sediment import or decreased sediment export. Hence, the transport capacity in the Loire became much more favourable for the import of sediment initiated by deepening. In order to determine the robustness of these findings, an extensive sensitivity study was performed of 14.157 simulations (1287 conditions for 11 bottom profiles over time) to capture the influence of uncertainties in multiple input parameters. For the bottom profile representing the bathymetry in the year 1900, none of the conditions resulted in a hyperturbid state, whereas independent of the conditions, the likelihood to find a hyperturbid state always increased for increasing depth. From this we can conclude, that the observed regime shift towards high sediment concentrations, would not have happened without the deepening of the Loire estuary.

1

INTRODUCTION

Riverine- and coastal areas have been subject to anthropogenic influences since time immemorial (Mays, 2008). The desired effects of human interventions show large variety; from safety against flooding to navigability and from prevention of coastal erosion to irrigation. Although hydraulic engineering works are suitable to create economic value or to solve or prevent problematic situations, it often occurs that new problems arise as a consequence. Construction of a coastal groyne to prevent coastal erosion for example, often results in erosion on the downstream side (which doesn't have to be problematic of course) (Bosboom and Stive, 2012). Another example is a decline of the groundwater table as a consequence of river-deepening, which could eventually result in the exposure of wooden pile foundations and hence accelerated decay of the foundation (Klaassen, 2015). In complex systems where multiple mutually interacting physical processes are involved, such problems are often unforeseen and poorly understood.

An example of this is the effect of deepening on the sediment dynamics in estuaries. An estuary is often defined as a semi-enclosed coastal body of water, freely connected with the open sea, in which sea water is measurably diluted by fresh water derived from land drainage (Pritchard, 1967). In other words, the estuary extends landward as far as the salinity reaches. However, according to the definition of Fairbridge (1980), the estuary extends landward as far as tidal motions are observed. The part of the estuary in which tidal motion is still present, but where the water is entirely fresh, is often called the tidal river. Figure 1.1 shows an overview of these definitions. The definition based on tidal motions is used in this thesis, hence the estuary includes both the brackish zone and the tidal river.

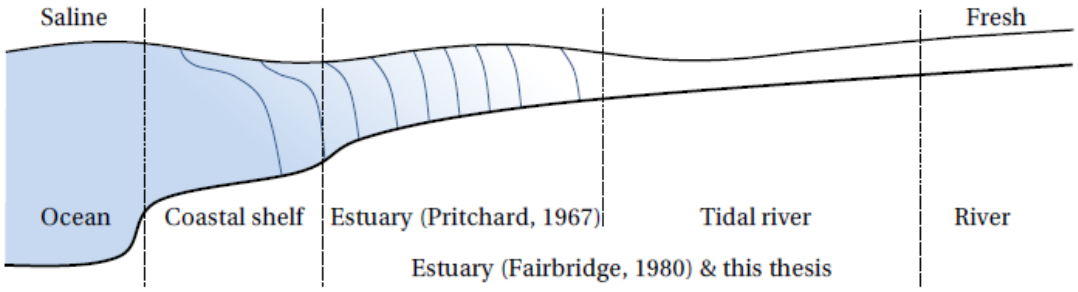

Figure 1.1: Schematic representation of an estuary, freely connected to the sea on one side and enclosed by the river on the other side. Saline water is presented in blue with the blue lines indicating equal salinity, whereas fresh water is shown in white. Source: Dijkstra (2019)

Suspended sediment concentrations in estuaries often have local maxima, also called estuarine turbidity maxima (ETMs). A formal definition of an ETM has been introduced by Burchard et al. (2018), stating that an ETM is a local maxima of the cross-sectionally and tidally averaged suspended sediment concentration. The existence of an ETM depends on a combination of horizontal sediment transports and the vertical balance between resuspension from and deposition to the bed. The magnitude and direction of the along-channel transport of sediments varies over a tidal cycle. However, when averaged over a tidal cycle, an upstream or

downstream directed residual transport is found which varies with the along-channel location. Fine sediment tend to accumulate in zones where this residual transport converges. These zones are called *trapping zones*. Next to the accumulation of fine sediment, which governs the availability of fine sediments, an ETM requires that the sediments are brought and kept suspension. The ability of the flow to keep sediments in suspension depends on the mixing energy, which is often provided by the tide or wind. In this thesis, the term ETM will also be used to describe the local maxima in near-bed or near-surface sediment concentrations, which is in contrast to the definition of Burchard et al. (2018).

According to Ross (1995), 22 of the 32 largest cities around the world are co-located with estuaries. Therefore, it is not surprising that estuaries have been heavily engineered over the years. Both restricting the flow area (narrowing) and deepening are common measures to improve the navigability or to control flood safety. However, estuaries are complex systems with lots of physical processes involved, due to which not all effects of such measures are foreseen. A study of five European estuaries by Winterwerp and Wang (2013) shows that tidal ranges increased significantly along with the ongoing narrowing and deepening of these estuaries. Next to an increase in tidal range, dramatic increase in suspended sediment concentrations has been observed in the Ems (Germany) and Loire (France) estuaries, often referred to as a *regime shift* towards *hyperturbid* state. While it is generally accepted that the increase in tidal range is a consequence of deepening and narrowing, it is not generally true that deepening and narrowing leads to a dramatic increase in sediment concentrations. For example, Dijkstra et al. (2019b) provides proof that deepening plays an important role in the observed regime shift in the Ems, whereas Dijkstra et al. (2019a) shows that this is not the case in the Scheldt. Whether deepening is a potential cause for the high sediment concentrations observed in the Loire is still unclear. This will be investigated in this thesis.

This includes an extensive model study to understand the behaviour of the present-day system, as well as the behavioural changes over time. One of the main difficulties in understanding the observed regime shift in the Loire estuary is the lack of observations of depth, tidal range and sediment concentrations. Therefore, to nevertheless do a robust investigation, sensitivity studies are used capture the effects of this uncertainty in the data on the processes that govern the sediment dynamics within the Loire estuary. By understanding the role of the uncertainties on the individual physical mechanisms, insight can be gained in whether deepening is a potential cause for the observed regime shift, or if unknown developments in the uncertain parameters might play a role. Before the model study is addressed, an introduction to the Loire estuary, including the observations that led to this research, is presented in section 1.2. Some general definitions and common knowledge about sediment dynamics within estuaries are introduced in section 1.3. And finally, this chapter will be concluded with the actual problem statement, followed by the accompanying research questions and the approach to investigate these questions throughout this thesis.

1.1. THE IMPORTANCE OF SEDIMENT DYNAMICS IN ESTUARIES

According to the Millennium Ecosystem Assessment (2005), the benefits humans experience from an ecosystem are called ecosystem services. Estuaries provide many ecosystem services, such as food supply, water supply, regulating of water quality, flood prevention and recreation (Wilson et al., 2005; O'Higgins et al., 2010). Related to sediment dynamics, two ecosystem services of estuaries are most relevant: primary production and commercial shipping.

Estuaries provide habitats for all kinds of aquatic flora and fauna. Microalgae (e.g. phytoplankton) and macrophytes (aquatic plants) are able to produce glucose (food) and oxygen out of carbon-dioxide and water using energy from sunlight through photosynthesis (Adams et al., 1999). The consequent accumulation of inorganic matter (CO_2 and H_2O) into organic matter is called primary production and forms the basis of the food web. Since estuaries receive large amount of nutrients and organic carbon from land, they are characterized as hot spots concerning primary production all around the world (Cloern et al., 2014). Because few organisms are capable of photosynthesising without the energy from solar radiation, a reduction of light intensity can have pronounced impacts on the primary production within estuaries. Moderate suspended sediment concentrations in the order 10-100 mg/l already block enough sunlight to reduce primary production (Wofsy, 1983). Observations in the Bristol Channel by Joint and Pomroy (1981) show a decrease of over a factor 20 in primary production for high sediment concentrations compared to low sediment concentrations. Similar reductions in primary productions due to high turbidity have been observed in the Loire estu-

ary (Relexans et al., 1988; Abril et al., 2003). Furthermore, increased turbidity often coincides with depletion of oxygen levels, reducing the livability of estuaries for aquatic fauna. According to Talke et al. (2009a) and Etcheber et al. (2007), the oxygen is consumed by bacterial degradation of organic matter which is present within the suspended matter. The reduction of primary production due to turbidity might eventually result in even further lowering of oxygen levels (Yoshiyama and Sharp, 2006).

Next to the natural value of estuaries, they are also of importance regarding economical aspects. Some of the largest ports around the world are located within estuaries (e.g. Shanghai Port in the Yangtze estuary, Port of Rotterdam in the Rhine-Meuse estuary) (Wang and Andutta, 2013). Navigational channels towards ports need to be maintained at a certain depth. Increased sediment concentrations could result in enhanced deposition of sediments within ports or shipping channels, and hence increase in dredging costs.

1.2. INTRODUCTION TO THE LOIRE ESTUARY

Although human interventions in the Loire have taken place for centuries, our focus will mainly be on the 20th century. On the one hand, the main channel has been deepened, and on the other hand side channels have been cut-off and again recreated later (Maquet, 1974; Charrier, 2000). All these changes caused changes in depth. This section provides a short introduction to the Loire estuary, focusing on these past large-scale changes in the depth and their effect on the water motion and sediment dynamics.

The Loire River Estuary is located on the West coast of France and mouths into the sea at Saint-Nazaire, see Figure 1.2. These days (during a spring tide high water and low river discharge), the tidal influence reaches between 90-110 km from the mouth, whereas the salt-water influence reaches less far and typically stops around Nantes (50 km inland). A hyperturbid zone may be present up to 70 km inland. The overview depicted in Figure 1.2 not only gives the present day situation, but also some historical details. It can be seen that the Loire estuary has been narrowed (by cutting of side-channels and removing intertidal areas) significantly since 1850. In addition to that, the figure clearly shows that the tidal influence, the salt intrusion and the turbid zone extended further inland over the last decades. To be able to discuss the various human interventions and their effects, distinction is made between five parts of the estuary following Migniot (1993). These are the exterior, lower(downstream), intermediate, embanked, and upstream sections.

Before the start of the 20th century the navigability of the Loire has been improved mostly by restricting the flow to one main channel; multiple side channels have been cut-off and embankments have been created to stabilise the river banks (Moatar and Dupont, 2016). At the end of the 19th century however, the depth of the Loire river did not suffice any more for ships to reach the commercial ports of Saint-Nazaire and Nantes. For that reason, multiple deepening operations have been executed since that time, of which the most significant are summarized below (SAR, 1993; Paape, 1994; Sogreah, 2006; Briere et al., 2011; Artelia, 2013):

- 1890-1899: the exterior channel has been deepened to CM96[1] -5.6 m and the embanked section to CM96 -1.2 m.
- 1906-1912: the intermediate channel has been deepened from CM96 +0.9 m to CM96 -2.1 m.
- 1913-1920: a 'Bassin de Marée'[2] was created upstream of Nantes.
- 1940: the exterior channel has been deepened to CM96 -8 m and the lower channel to CM96 -6.5 m.
- 1948-1968: the intermediate and embanked sections are deepened from CM96 -2.6 m to CM96 -5.1 m.
- 1969-1973: the exterior channel is deepened to CM96 -9.4 m, the lower channel to CM96 -9.35 m and the intermediate and embanked channel to CM96 -5.6 m.
- 1978-1980: the exterior and lower channel are deepened to CM96 -12.85 m.
- 1985-1986: the exterior channel has been deepened to CM96 -13.7 m.

As a consequence of these deepening operations, the tidal range has increased significantly since the early 1900s (see Figure 1.3). The maximum amplification of the tidal range can be found around Nantes with an amplification of over 4 m. Different sources show slightly different tidal ranges during approximately the

[1] CM96 is an old French reference level, data presented by Jalón-Rojas et al. (2016) shows that present mean sea level at Saint-Nazaire is 4 meters above CM96.

[2] Tidal basin which has been created by large-scale sand extractions to promote tidal intrusion, which on its turn promoted navigability (Hubiche, 2002).

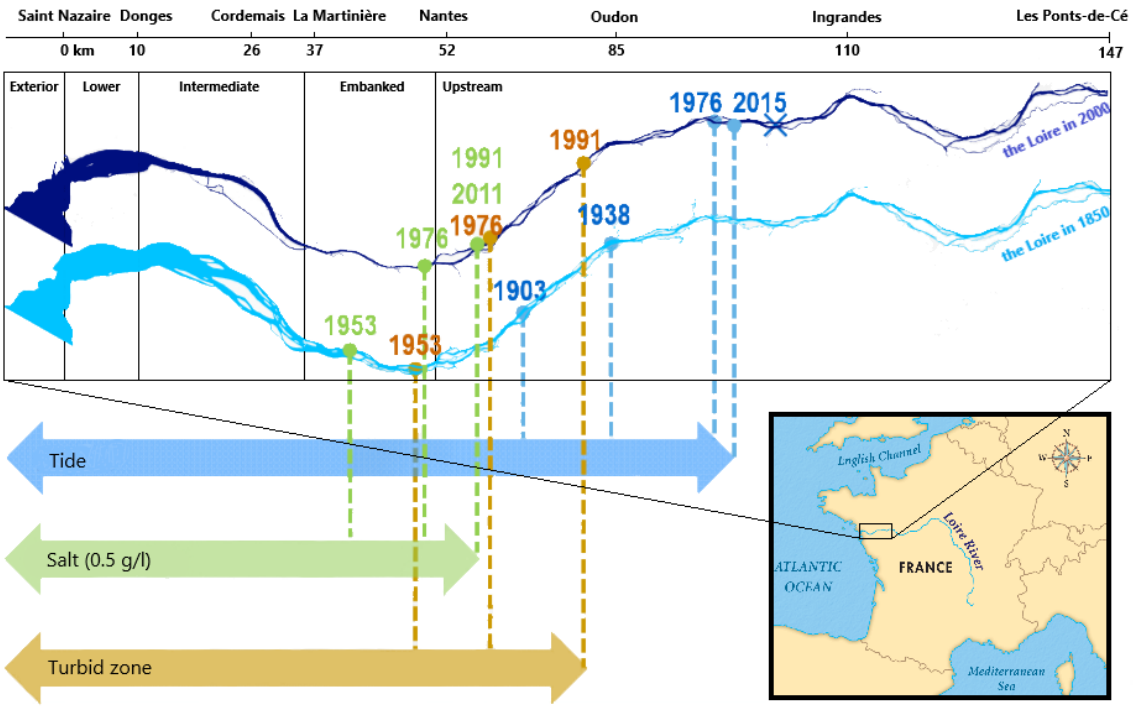

Figure 1.2: Maximum observed intrusion of tide, salt and estuarine turbidity maximum during high water spring tide and low river discharge over the last 150 years. Furthermore, distinction is made between the exterior, lower (downstream), intermediate, embanked and upstream section of the estuary. Based on: GIP (2017)

same periods, which is because of daily variations. In France, the amplitude of the tidal oscillation is expressed with a 'Coefficient de marée' (EN: tidal coefficient), which is a measure of the actual tidal oscillation to its mean. For spring tides, this coefficient varies between 90 and 100, whereas values between 40 and 50 are common for neap tides (Hubiche, 2002). The differences between the two examples of tidal ranges around the year 2000 in Figure 1.3 are due to a slightly higher tidal coefficient for the 2000 case than for the 2002 case. The differences between 40-60 km for the cases of 1903 are probably due to difference in river discharge, which affects the tidal propagation through complex non-linear interactions.

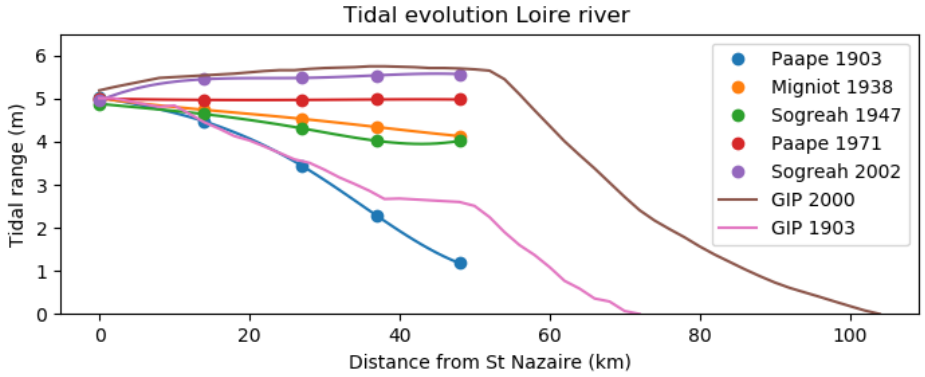

Figure 1.3: Development of tidal range (spring tide), for low river discharge along the Loire estuary. Sources: Migniot (1993), Paape (1994) and Sogreah (2010)

Besides the amplification of the tidal range, sediment concentrations also changed considerably in the 20th century. For the first part of the century, hardly any measurements were found regarding turbidity. Probably the first extensive reports about turbidity in the Loire estuary were by Leopold Berthois in the 1950s (Guilcher, 1988). Berthois and Barbier (1953) and Berthois (1955b) present measurements showing that the turbid zone

could be found up to Le Pellerin (39 km inland) with its maximum around Cordemais (26 km from the mouth) during periods with low river discharge and spring tide. Over an entire ebb-flood cycle, maximum concentrations in the order of 700 mg/l (surface) and around 3 g/l (bottom) are found during low water (Berthois, 1954, 1955b). Averaged over a tidal cycle, these values can be a factor 2 to 3 smaller. Although most of the concentrations mentioned by Berthois do not exceed 3 g/l (or 1 g/l when tidally averaged), Berthois (1955b) mentions maximum turbidity values near Cordemais (26 km inland) of 20 g/l during summer. Unfortunately, no clarification is provided about the exact moment and position in the water column at which these measurements are taken, but it shows that high sediment concentrations were already observed occasionally in the 1950s. Based on these sources, a curve has been drawn with typically tidally averaged sediment concentrations at the surface along the Loire estuary around 1950 (see Figure 1.4).

After Berthois, several other researchers have reported about the turbidity in the Loire estuary. In the 1970s, Gallenne (1974a,b) show that although the concentrations remain unchanged, the turbid zone could reach up to Nantes with its maximum still around Cordemais. Comparable data was found by Saliot et al. (1984) as presented in Figure 1.4. According to Migniot (1993) and Paape (1994), tidally averaged concentrations near the surface in the range 0.3-0.7 g/l were still common in the early 1990s. However, the turbid zone did extend further inland and reached up to 60 km from Saint-Nazaire.

In 2007, six monitoring stations have been installed 1 meter below the surface in the Loire estuary from Saint-Nazaire up to Bellevue (62 km upsteam), called the SYVEL network. One of the characteristics that has been monitored with a high frequency (measurements every 10 minutes) by these stations is turbidity. Based on data gathered between 2007 and 2013, Jalón-Rojas et al. (2016) have been able to track the turbid zone in the Loire estuary. As was already observed in the 1990s, the turbid zone may reach (more than) 60 km inland. However, in contrast to the measurements performed before 2000, much higher concentrations are observed. For low river discharges, the ETM can be found between 25 and 40 km inland, with maximum concentrations in the order of 5 g/l. An indication of tidally averaged concentrations near the surface for periods of low river discharge and spring tidal conditions is added to Figure 1.4.

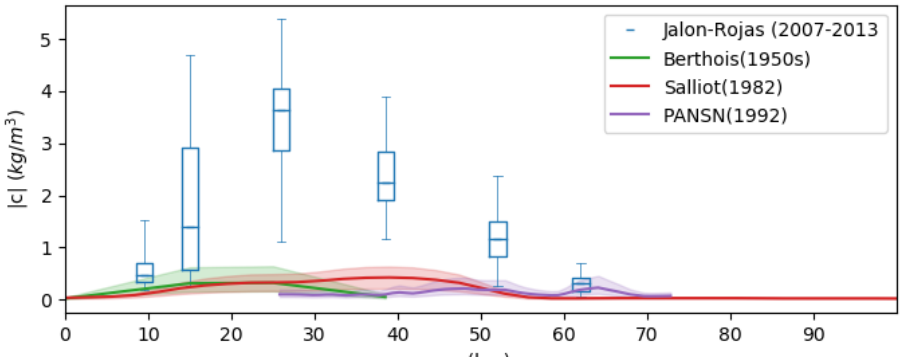

Figure 1.4: Evolution over the last decades of the sediment concentrations near the water surface for low river discharges and spring tidal conditions. The green curve represents an estimation of tidally averaged concentrations in the 1950s, based on instantaneous measurements of Berthois (1954, 1955b). The shaded area is used to indicate the observed spread. A similar estimation has been presented for 1982 and 1992, based on data presented by Saliot et al. (1984) and Paape (1994). Boxplots (containing minimum,q1,median,q3 and maximum) are used to describe recent turbidity measurements at the surface, obtained with the SYVEL network and presented by Jalón-Rojas et al. (2016).

1.3. GENERAL CONCEPTS AND DEFINITIONS

Some general definitions and common knowledge about physical processes governing the sediment dynamics within estuaries should be introduced before going into detail in the upcoming chapters.

1.3.1. WHAT IS HYPERTURBIDITY?

There is no clear general definition of a hyperturbid state. In order to find a useful definition for this thesis, a classification of sediment concentrations in estuaries is considered following Winterwerp and Van Kesteren (2004). Firstly, low-concentration mud suspensions (LCMS) are defined as suspensions with sediment con-

1

centrations typically in the order of 10 mg/l- 1 g/l. Such concentrations are too low to affects the flow field. Secondly, high-concentration mud suspensions (HCMS) are defined as suspension with sediment concentrations in the order of 100 mg/l or higher. In HCMS, the vertical distribution of sediment becomes stratified with significantly higher concentrations near the bed than near the surface. This suppresses turbulent motions, which in turn may have a significant influence on the flow field (Geyer, 1993). For even higher sediment concentrations (typical order of 10-100 g/l), the presence of one sediment floc reduces the effective settling velocity of another floc, called hindered settling (Richardson and Zaki, 1954). In the higher end of this concentration range, a dense network of sediment particles causes the viscosity of the fluid to increase, limiting the turbulent character of the flow, which is often referred to as mobile mud (or fluid mud) (Bruens, 2003). Finally, for concentrations exceeding 100 g/l, the so-called gelling concentration, consolidation starts and the sediment mixture gradually builds up strength.

The term hyperturbidity was first mentioned by Winterwerp (2011) and although Winterwerp and Wang (2013) elaborated on the subject, no formal definition is provided. Dijkstra (2019) introduces a qualitative description stating that an estuary may be called hyperturbid when fluid mud is present over a sufficiently large stretch of the estuary such that it significantly affects the estuary-scale water motion during a significant portion of the year. For this research, a combination of the classification by Winterwerp and Van Kesteren (2004) and the qualitative description of Dijkstra (2019) is used:

"*The Loire is considered hyperturbid when concentrations in the order of 100 mg/l to 10 g/l are found near the surface, and 5-100 g/l near the bottom over a stretch of at least 10 kilometer for a couple of months per year.* "

1.3.2. WHAT IS A REGIME SHIFT

A *regime* can be described as a dynamic equilibrium state of a system. If the external conditions for a system remain constant for a long time, the system might eventually reach a stationary equilibrium state. However, systems are often exposed to dynamical forcing, hence the equilibrium state of a system may vary as well. The transition from one state to another as a consequence of changing conditions is called a regime shift.

According to Scheffer et al. (2001), regime shifts can be classified as smooth, abrupt or discontinuous. When small changes in the external conditions have relatively small consequences for the state of the system, we speak about a smooth regime shift. However, it might also be the case that small change in external conditions results in a large change of the state, which is the case for both abrupt and discontinuous regime shifts. The difference between these two types of regime shifts is mainly the reversibility of the changed state. While an abrupt regime shift initiated by a small increase in external forcing could be reversed by an equal decrease of this forcing, reversing a discontinuous regime shift requires a much larger decrease of the forcing (see Figure 1.5). This asymmetrical behaviour of the regime shifts between the two states is called hysteresis.

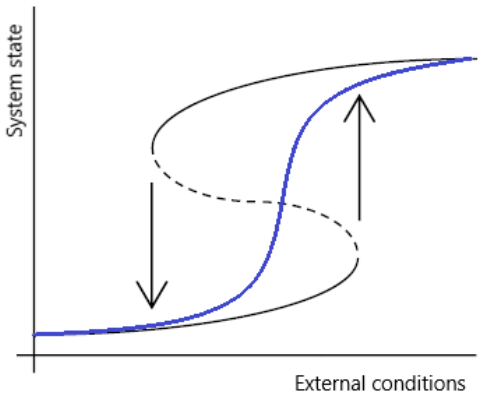

Figure 1.5: Abrubt (in blue) and discontinuous regime shift (in black) of the system state as a function of external conditions, based on Scheffer et al. (2001).

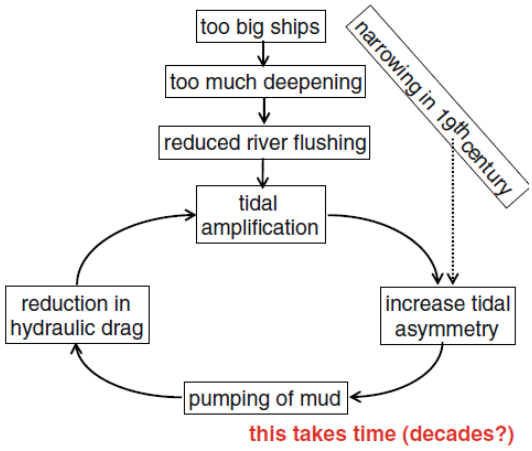

Figure 1.6: Conceptual feedback loop that might be the cause for the hypertyrbid conditions in the Loire estuary these days. From: Winterwerp and Wang (2013)

The regime shift investigated in this thesis concerns the shift from low to moderate concentrations of suspended sediment (order of 100-500 mg/l near the bed) towards the hyperturbid state as defined before. According to Winterwerp and Wang (2013) observed regime shifts in sediment concentrations can be explained by the feedback mechanism depicted in Figure 1.6. Deepening of the estuary to increase navigability may result in reduced flushing of sediment by the river and amplification of the tidal motions (further introduced in the next section). As a consequence of the tidal amplification, tidal asymmetry may increase in such a way that more sediments are pumped into the estuary. Increased sediment concentrations reduce the hydraulic drag within the estuary, which in turn enhances the tidal amplification, which closes the feedback loop. The existence of such a feedback loop has been confirmed by Dijkstra et al. (2019b) by showing that deepening can be held responsible for a regime shift (discontinuous character) in the Ems.

1.3.3. TRANSPORT AND RESUSPENSION OF SEDIMENT

For the formation of an ETM, two conditions should be met. At first, sufficient sediment should be trapped within the estuary, and secondly, the water motion should be capable of bringing/keeping the sediments in suspension. A short overview of the general knowledge about both aspects is presented in this section.

SEDIMENT TRAPPING

Estuaries are complex systems in which various flow processes play a role. We can easily imagine that suspended sediments are carried along with the flow, hence the transport of sediments depends on the strength of the flow and the amount of suspended sediments. However, the interplay of various flow processes result in complex flow patterns. Consequentially, some of the processes always tend to transport sediments towards the sea, whereas other processes always contribute to the import of sediments. Furthermore, several processes can be exporting or importing depending on for example time (variation over a tidal cycle) and/or location (variation in along-channel direction). On a subtidal scale, the sum of the residual transports of all processes might result in convergence of sediment transport somewhere along the estuary, where an ETM will appear. Flow processes that are generally considered to play a significant role in transport of sediments are introduced below.

- As already mentioned while introducing the positive feedback loop presented by Winterwerp and Wang (2013), *tidal asymmetry* could play an important role in the transport of suspended sediments. Tidal asymmetry is characterized by a difference in maximum velocities during flood and ebb. Due to a non-linear relation between flow velocities and sediment transport, tidal asymmetry causes a subtidal residual transport in the direction in which maximum velocities occur (Wang et al., 1999). Tidal asymmetry in estuaries can either originate from asymmetrical external forcing, or can be internally generated due to interactions with bathymetry and river flow e.g. (Guo et al., 2014).
- Next to a temporal asymmetry of the velocity signal, spatial velocity gradients may cause residual transport as well. Due to *spatial settling lag*, sediments are transported towards locations with minimum tidal velocity amplitudes (see Postma (1954); Pritchard and Hogg (2003)).
- Another process that plays an important role is the intrusion of salinity. An along-channel density gradient (induced by decreasing salinity in landward direction) drives an estuarine circulation, called *gravitational circulation*, with a landward directed flow near the bed and a seaward flow near the surface. For an increasing sediment concentration from surface to bottom, gravitational circulation causes a net landward flow, which was first noticed by Postma and Kalle (1955). In case of a highly stratified flows, turbulent motions are suppressed, and as a consequence sediments are even more concentrated near the bottom, enhancing the before mentioned net landward transport of sediments (Geyer, 1993).
- Although the *river* induced velocities are always directed seaward, hence causing an export of sediments, the river contribution is of importance regarding hyperturbidity in estuaries. Firstly, large riverine sediment supply increases the availability of sediments in estuaries, e.g. Yangtze River (Wang et al., 2015). Secondly, an ETM occurs where sediment transport converges. Having the river as one of the main exporting contributions makes the location of the ETM therefore strongly dependent on the river discharge. Thirdly, river flow might affect the tidal asymmetry through non-linear interactions, generally enhancing sediment export (Wang et al., 1999; Guo et al., 2014), and restricting salinity intrusion (Savenije, 1992).
- There are many other processes that might contribute to an along-channel residual transport, e.g. gravitational circulation induced by along-channel gradients in sediment concentrations (Talke et al., 2009b), lateral circulation (e.g. Burchard and Schuttelaars (2012)) and tidal straining (see Simpson et al.

(1990) and Burchard and Baumert (1998)). No further details are discussed since these processes will not be treated throughout this thesis.

RESUSPENSION OF SEDIMENTS

In one of the simplest, yet widely used conceptual views of resuspension, the amount of resuspension depends on the strength of the flow versus the strength of the bed. According to Partheniades' formulation for resuspension (e.g. Kandiah (1976)), sediments can be eroded when a certain critical shear stress, which can be seen as a strength parameter of the bed, is exceeded. Some of the main factors influencing the critical shear stress are cohesion, grain size and the degree of consolidation. The strength of the flow is typically expressed in a near-bed velocity, which is related to the exerted shear stress on the bed (Winterwerp and Van Kesteren, 2004). When describing erosion, often an erosion rate coefficient (or erosion parameter) is included to parametrize all processes that are not explicitly considered in this simple model. A more detailed description of the erosion formulation used in this research is provided in chapter 2.

1.4. RESEARCH QUESTIONS AND APPROACH

1.4.1. RESEARCH QUESTIONS

The goal of this thesis is to determine the role that deepening of the Loire estuary played in the observed regime shift from low to high sediment concentrations. Only limited observations of depth, tidal range and sediment concentrations are available, resulting in significant uncertainties in the model input. By determining the effects of these uncertainties on the various processes that govern the sediment dynamics, the robustness of the model results can be indicated. Consequentially, due to the awareness of the effects of uncertainty in the model input, the effects of deepening can be investigated, and hence the hypothesis of Winterwerp and Wang (2013) can be evaluated. The main questions that I would like to answer throughout this thesis are:

- What are the governing processes regarding sediment dynamics in the Loire estuary?
- How are these processes affected by deepening in the Loire?
- Can these effects be the potential cause for the regime shift in the Loire estuary?
- Does the hypothesis of Winterwerp and Wang (2013) hold for the Loire estuary?

1.4.2. APPROACH

To find an answer to these research questions, a model study is performed. According to Murray (2003), models can be classified along a spectrum ranging from 'simulation models' to 'exploratory models'. Simulation models on the one end, also referred to as complex models, are designed to reproduce the behaviour of a system as detailed as possible. Optimal quantitative similarity between model results and reality can be achieved by including all the physical processes determining the behaviour of the natural system in the model. Processes that remain unresolved in complex models need to be accounted for with state-of-the-art parametrisations. High detailed model results are clearly very useful when small scale phenomena are of interest within the system to be studied. Nevertheless, the high complexity also has its downsides. At first, the numerical character of such models results in relatively long computation time, which makes it unattractive to perform extensive sensitivity studies. Secondly, such models are often non-linear, which makes it hard to identify the importance of individual physical processes and therefore understand which processes are most important. Exploratory models on the other end, also referred to idealised models, are characterised by a high degree of simplification. The basic idea behind idealised models is to only include the physical processes essential for the specific behaviour of the system that is studied. By including only the essential physical processes, idealised models are complex enough to reproduce the behaviour, but they remain often simple enough to construct analytical solutions. This makes idealised models perfectly suitable for studying isolated physical mechanisms. Since these models can often be solved analytically or with simple numerical procedures, computation time remains relatively short (Chernetsky et al., 2010).

The iFlow modelling framework aims to combine the best of both approaches. On the one hand, several complex physical processes and interactions are included, whereas on the other hand iFlow is computationally efficient and physical processes can be studied in isolation (Dijkstra et al., 2017). The combination of these characteristics makes iFlow an attractive model to investigate the research questions, since we are interested in the effects of uncertainty (need for sensitivity studies) on the governing processes.

Due to the idealised character of iFlow, the data needed to create a model of the Loire estuary should correspond to the main characteristics of the real Loire estuary in a qualitative manner. To create a model for the current state of the Loire, data should be collected about the hydrodynamics (water level amplitudes and phases), salinity and turbidity distributions, the geometry including both width and depth, and the external forcing (tides and river discharge). Once the model is capable of qualitatively reproducing the hydrodynamics and sediment dynamics, analysing the physical processes separately should provide insight in which processes are governing the sediment dynamics within the Loire estuary in the current state. However, some parameters are prone to large uncertainties (e.g. the erosion parameter) or natural spread (e.g. river discharge). By performing sensitivity studies to the effects of these variabilities, the robustness of the model results can be investigated (Schuttelaars et al., 2013).

In essence, the only model parameter that has to change to investigate the effect of deepening on the sediment dynamics in the Loire estuary is the depth. For this, we need to know how the depth of the Loire developed over time, hence bathymetrical profiles capturing the global depth along the estuary (e.g. thalweg levels) are needed. Single deepening campaigns are of minor importance to describe the global bathymetry, but they can provide useful information about the depth in certain years. By assuming a gradual transition between the topography in years for which data was available, a bottom profile can be reconstructed for every point in time since 1900. When the hypothesis of Winterwerp and Wang (2013) holds for the Loire estuary, there should be a critical depth profile at which the regime shifts. By combining the findings of the sensitivity studies concerning the uncertainty in the input and the studies to the effects of deepening, we will be able to draw robust conclusions, despite the given uncertainty.

1.5. OUTLINE

Some more background, the governing equations and practical implications of the iFlow model for this research are discussed in chapter 2. Subsequently, chapter 3 presents an extensive description of the available data about the Loire estuary (both actual and historical), necessary for the set-up of an iFlow-model. In chapter 4, an analysis of the system and the governing processes in the Loire will be discussed based on the present-day situation. The robustness of the model results will be tested with various sensitivity studies. The actual effects of deepening activities in the Loire estuary are elaborated in chapter 5, therefore to the main question whether deepening can be held accountable for the regime shift to the hyperturbid state. Finally, critical notes to the obtained results and answers to the research questions conclude this report in chapter 6.

2

INTRODUCTION TO IFLOW

iFlow is a width-averaged model describing the hydrodynamics and sediment dynamics within estuaries and tidal rivers, focussing on the global estuarine processes in the longitudinal direction. The iFlow modelling framework has been based on the idealised model of Chernetsky et al. (2010), which solves the width-averaged shallow water equations (see subsection 2.2.1) and the width-averaged sediment mass balance equation (see subsection 2.2.2) using a combination of analytical and numerical solution techniques. One of the core features of iFlow is that its complexity can be extended easily by adding modules, which are individual model components to implement certain physical processes or additional tasks (e.g. calibrating, plotting or initiating sensitivity studies), such that the complexity of the model fits the purpose (Dijkstra et al., 2017). However, increasing the complexity often means that numerical solutions are necessary, hence increasing the computational costs. Furthermore, including complex numerical solutions reduces the ability to analyse results. In this, we recognise the trade-off between the desired degree of detail of the results on the one hand and comprehensibility of the results on the other hand, as introduced in chapter 1.

2.1. MODEL DOMAIN AND GRID

The two-dimensional width-averaged (2DV) model domain is sketched in Figure 2.1. The x-coordinate is defined in along-channel direction, starting with x = 0 at the seaward boundary and ending at the landward boundary x = L, whereas a z-coordinate is used to describe the vertical axis. A river discharge must be defined at the landward boundary, so although the landward boundary can be defined freely, it is convenient to define the landward boundary at a location where river discharges are known, and for which no confluences are found in downstream direction. The length of the estuary is the distance between the seaward boundary (x=0) and the landward boundary (x=L). The bed level, -H, and the width, B, can be defined with any arbitrary

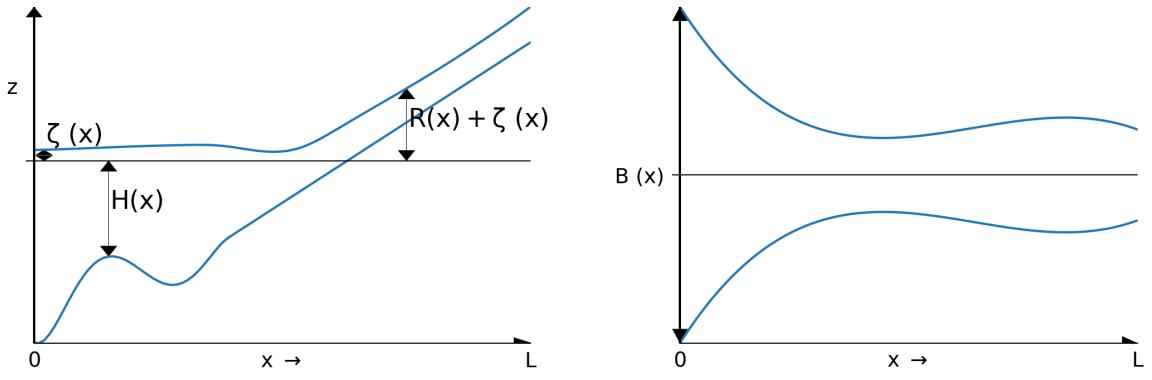

(a) Side view

(b) Top view

Figure 2.1: A typical model domain of an iFlow model, in which smoothly variations are allowed for both depth and width in along-channel direction.

function varying in x-direction as long as the functions are smooth (see Figure 2.1). The bed level -H is measured with respect to mean sea level at the seaward boundary (MSL, defined at z=0).

The surface elevation relative to z = 0 consists of the sum of the reference level R and the surface elevation ζ (see Figure 2.1a). The reference level R can be interpreted as an approximation of the local mean surface level due to the river set-up. The default value of R is 0, i.e. the local mean surface level can by approximated by mean sea level at the seaward boundary. However, once the bed level is above MSL, a non-zero reference level is required such that H+R (estimated mean water depth) remains positive throughout the entire domain. Another case in which a non-zero reference level is required to correct the mean water depth, is when the mean surface elevation ζ and the bed level H are of the same order.

2.2. EQUATIONS

This section provides an overview of the equations and boundary conditions used in iFlow to describe the hydrodynamics and the sediment dynamics.

2.2.1. HYDRODYNAMICS

The Reynolds-averaged width-averaged momentum- and continuity equation are used to describe the water motion. By assuming hydrostatic pressure (restricting ourselves to long waves only), neglecting the effects of wind stress and Coriolis, and assuming that density differences are small compared to the average density (allowing for the Boussinesq approximation), these equations reduce to the following width-averaged shallow water equations:

$$u_t + uu_x + wu_z = -g(R_x + \zeta_x) - g\int_z^{R+\zeta} \frac{\rho_x}{\rho_0} dz + (A_v u_z)_z \tag{2.1}$$

$$w_z + \frac{1}{B}(Bu)_x = 0 \tag{2.2}$$

in which the width-averaged water level elevation is denoted with $\zeta(x,t)$, the reference level with R, the width-averaged horizontal velocity with $u(x,z,t)$ and the width-averaged vertical velocity with $w(x,z,t)$. In addition, time is denoted with t, g is the gravitational acceleration, ρ stands for density, ρ_0 is a constant reference density and A_v represents the vertical eddy viscosity coefficient. Partial derivatives in t, x and z-dimension are denoted with a subscript $(.)_{dimension}$ for the respective dimension.

Regarding the width-averaged momentum equation (Equation 2.1), inertia is captured in the first term while advection is represented by the second and third term. Multiple exerting forces can be recognized on the right hand side of Equation 2.1: the first term represents a barotropic pressure gradient initiated by a gradient in the surface level, the second term represents a baroclinic pressure gradient caused by along-channel differences in density and the last terms represents the internal frictional force due to turbulent motions. In order to solve Equation 2.1 and Equation 2.2, boundary conditions are needed as well as a definition for the along-channel density and a turbulence closure.

At the free surface $z = R+\zeta$, the kinematic boundary condition describes that water particles cannot leave the surface and furthermore the no-stress condition applies, since the wind induced shear stress is neglected.

$$w = \zeta_t + u\zeta_x \tag{2.3}$$

$$A_v u_z = 0 \tag{2.4}$$

At the bottom $z = -H$, the kinematic boundary condition describes that water particles cannot pass through the bottom (impermeable bed) and a partial-slip condition is assumed.

$$w = -uH_x \tag{2.5}$$

$$A_v u_z = s_f u \tag{2.6}$$

The parameter s_f is the stress parameter, describing the partial slip condition at the top of the constant stress layer. This is further explained in Equation 2.2.1.

In order to derive a differential equation for the water level, the depth averaged continuity equation (presented in Equation 2.7) is considered as well.

$$\zeta_t + \frac{1}{B}\left(B\int_{-H}^{R+\zeta} u\,dz\right)_x = 0 \tag{2.7}$$

On the seaside of the estuary, $x = 0$, the water motion is forced by a tidal signal containing a semi-diurnal M_2 and a quarter-diurnal M_4 constituent. We would like to express the tidal signal as a sum of the M_2 signal with phase 0 and an M_4 signal with relative phase ψ:

$$\zeta(0,t) = A_{M2}\cos(\sigma t) + A_{M4}\cos(2\sigma t - \phi) \tag{2.8}$$

in which A_{M2} and A_{M4} are the amplitudes, σ is the M_2 tidal angular frequency and ϕ is the relative phase difference. The derivation of A_{M2}, A_{M4} and ϕ from an M_2 and an M_4 signal, is presented in Appendix A.

At the landward boundary of the estuary, $x = L$, a constant river discharge Q is imposed. The tidal discharge is required to vanish so the boundary condition can be written as:

$$B\int_{-H}^{R+\zeta} u\,dz = -Q \tag{2.9}$$

DENSITY GRADIENT ALONG THE ESTUARY

It is assumed that the along-channel density gradient is purely caused by a decreasing salinity in landward direction, which means that the density gradient induced by suspended sediment concentrations and temperature are neglected. In analogy to Talke et al. (2009b), the estuary is assumed to be well-mixed regarding salinity. With these assumptions, we can express the along-channel density as

$$\rho(x) = \rho_0\left(1 + \beta_s S(x)\right) \tag{2.10}$$

in which ρ_0 is the reference density, β_s is a coefficient to convert salinity into density and $S(x)$ is the salinity along the estuary.

TURBULENCE CLOSURE

To parametrise the turbulent motions (captured by the eddy viscosity) and the roughness, a turbulence closure is introduced obtained by fitting results to results obtained with a $k-\epsilon$ closure. A dimensionless roughness height z_0^* is used as a calibration parameter. In this thesis, the value of z_0^* may vary along the estuary using a predefined function that varies with x, e.g. a tangent-hyperbolic function to make distinction between two regions with different roughness characteristics. Expressions for the eddy viscosity and the roughness read according to Dijkstra et al. (2017)

$$A_v = \alpha U(H + R + \zeta) f_1(z_0^*) \tag{2.11}$$

$$s_f = \beta U f_2(z_0^*) \tag{2.12}$$

where U is the depth-averaged velocity and α, β, $f_1(z_0^*)$ and $f_2(z_0^*)$ are parameters and functions approximated by fitting results of the k-ϵ model which are included hard-coded in iFlow (see Dijksta (2017)).

SEDIMENT INDUCED TURBULENCE DAMPING

Nevertheless, within hyperturbid estuaries, the turbulent motions are significantly affected by the high sediment concentrations (e.g. Geyer (1993); Winterwerp (2001); van Maren et al. (2015); Van Maren et al. (2015)). Based on the damping functions introduced by Munk and Anderson (1948), which accounted for suppression of vertical mixing due to a thermocline (large temperature gradient), Dijkstra et al. (2019c) suggested damping functions based on gradients in sediment concentrations to account for sediment induced turbulence damping. This resulted in parametrisations of the eddy viscosity A_v and eddy diffusivity K_v as functions of the depth-averaged velocity, depth and a damping function times a depth-averaged gradient Richardson number $\bar{R}i$:

$$A_v = \left\langle c_{v,1}(z_o^*) U (H + R + \zeta) F(\overline{\mathrm{Ri}}) \right\rangle \tag{2.13}$$

$$K_v = \left\langle \frac{c_{v,1}(z_o^*)}{\sigma_p} U (H + R + \zeta) G(\overline{\mathrm{Ri}}) \right\rangle \tag{2.14}$$

in which $c_{v,1}(z_o^*)$ is a drag coefficient which depends on the dimensionless roughness height z_0^*, σ_p is the Prandtl-Schmidt number (= 1 by default) and F and G are the damping functions as suggested by Dijkstra et al. (2019c). It can be seen that, without the sediment induced damping of turbulence, the eddy viscosity and the eddy diffusivity are equal. The damping functions F and G are defined as

$$F(\overline{\mathrm{Ri}}) = \left(1 + 10\overline{\mathrm{Ri}}\right)^{-1/2} \tag{2.15}$$

$$G(\overline{\mathrm{Ri}}) = \left(1 + 3.33\overline{\mathrm{Ri}}\right)^{-3/2} \tag{2.16}$$

in which the gradient Richardson number reads

$$\mathrm{Ri} = \frac{g\beta_c}{\rho_0} \frac{c_z}{u_z^2 + u_{z,min}^2} \tag{2.17}$$

The gradient Richardson number is a measure for the ratio of the increase of potential energy to the increase in turbulent energy over depth, hence a higher Ri means relatively less turbulent energy or more potential energy, thus reduced eddy viscosity and diffusivity. Like for the conversion of salinity to density, a coefficient, this time β_c, is used to convert sediment concentrations to density. Furthermore, $u_{z,min}$ accounts for unresolved flows and turbulence production. It can be interpreted as a certain background shear to avoid unrealistically large gradient Richardson numbers.

Regarding the bed shear stress, distinction is made in the bed shear stress felt by the water motion $\tau_{b,w}$ and the bed shear stress that causes erosion τ_b. The shear stress felt by the water motion is the shear stress in the lowest part of the bottom boundary layer. The shear stress that governs the erosion of sediments applies at the water-bed interface, and is therefore not affected by the sediment stratification in the boundary layer just above the bed. The bed shear stress felt by the water motion is parametrised as

$$\tau_{b,w} = s_f u_{bed} \tag{2.18}$$

in which the partial slip parameter s_f is defined as

$$s_f = \langle c_{v,2}(z_0^*) c_D U \rangle \tag{2.19}$$

The partial slip parameter s_f depends on the depth-averaged velocity U, a drag coefficient $c_{v,2}$ that is a function of (z_0^*) and a reduced drag coefficient C_D that accounts for the deformation of the bottom boundary layer as a consequence of sediment stratification. The reduced drag coefficient used within iFlow has been based on multiple studies (see Dijkstra et al. (2019c)) and reads

$$c_D = (1 + 5.5(\mathrm{Rf}_{bed}))^{-2} \tag{2.20}$$

with

$$\mathrm{Rf}_{bed} = \frac{K_v}{A_v} \mathrm{Ri}_{bed} \tag{2.21}$$

The drag reduction depends on the flux Richardson number near the bed. Within iFlow, this flux Richardson number can become unrealistically large, which would result in an overestimation of the drag reduction. Therefore, based on the ranges of damping typically observed in laboratory experiments, the maximum value of Rf_{bed} is set to $Rf_{max} = 2$.

As already mentioned before, the bottom shear stress that governs the erosion of fine sediments is not affected by near-bed stratification. In iFlow, τ_b is therefore defined as

$$\tau_b = s_s u_{bed} \tag{2.22}$$

in which s_s is defined like s_f with the reduced drag coefficient $c_D = 1$.

2.2.2. SEDIMENT DYNAMICS

The width-averaged sediment concentration $c(x,z,t)$ throughout the model domain is solved with the width-averaged sediment mass balance, which according to Chernetsky et al. (2010) reads:

$$c_t + uc_x + wc_z = w_s c_z + (K_h c_x)_x + \frac{B_x}{B} K_h c_x + (K_v c_z)_z \tag{2.23}$$

in which w_s describes a constant settling velocity and K_h and K_v are coefficients for the horizontal and vertical eddy diffusivity respectively. On the left hand side of Equation 2.23, we recognize inertia (first term) and advection (second and third term). The terms on the left hand side represent the settling (first term) and diffusive fluxes (other terms).

Like for the hydraulic boundary conditions, there is no transport of sediment particles through the water surface, so the boundary condition at $z = R + \zeta$ reads

$$w_s c + K_v c_z - K_h c_x \zeta_x = 0 \tag{2.24}$$

Furthermore, near the bottom, the diffusive flux equals the erosive flux E. So at $z = -H$, we have the boundary condition

$$K_v c_z - K_h c_x H_x = E \tag{2.25}$$

in which E is the erosion rate, which is based on Partheniades' formulation, but by excluding the necessity of a critical shear stress (shear stress that needs to be exceeded before erosion takes place) (e.g. Kandiah (1976)):

$$E = M|\tau_b(x,t)|f(a(x)) \tag{2.26}$$

with an erosion parameter M and τ_b is defined as

$$\tau_b = \rho_0 A_v u_z = \rho_0 s_f u \tag{2.27}$$

The function f, referred to as erodibility, describes the relation between the erosion and the availability a of sediments on the bed. Within iFlow, a tidally averaged erodibility f is computed, hence f does not contain a time dependency. For small amounts of easily erodible sediment on the bed, the erosion is governed by the availability and hence the erodibility f is a function of the availability a. However, for increasing availability the erodibility tends to saturate at a value 1. Therefore, the erodibility becomes independent of the amount of sediment sediments on the bed. This relation is depicted in Figure 2.2, in which the amount of sediment on the bed is expressed with a dimensionless sediment stock $\tilde{S}$ following Brouwer et al. (2018).

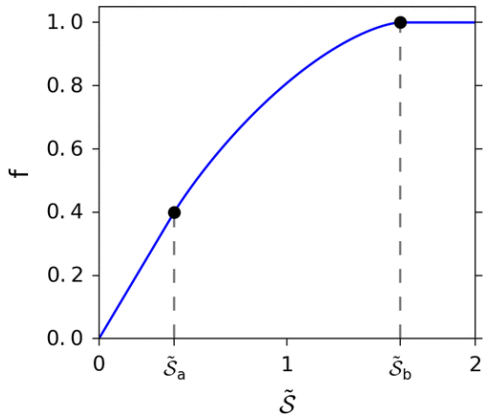

Figure 2.2: The erodibility f as a function of the amount of sediment available on the bed expressed in a dimensionless sediment stock $\tilde{S}$. Source: Brouwer et al. (2018)

The availability $a(x)$ is an unknown. A solution can be found when a *sediment concentration equilibrium condition* is imposed. Such an equilibrium condition has been based on the *morphodynamic equilibrium*

condition of Friedrichs and Aubrey (1988), which states that the amount of sediment in an estuary varies on a timescale much longer than the timescale at which easy erodible sediments are redistributed over the estuary. In other words, tidally averaged erosion and deposition balance each other. The sediment concentration equilibrium condition only requires that the amount of *suspended* sediment does not change on this time scale. The amount of sediments on the bed, sometimes called the bottom pool, is allowed to grow assuming this does not result in significant bed level changes. According to Dijkstra et al. (2019c), the expression for this this equilibrium reads

$$f_a \left\langle B \int_{-H}^{R+\zeta} (uc - K_h c_x) dz \right\rangle_x = 0 \tag{2.28}$$

in which f_a is the partial derivative of the erodibility f with respect to the availability a, B is the width, uc represents the advective sediment transport and $K_h c_x$ the diffusive transport. From this equation we can see that equilibrium exists either when the sum of the advective and diffusive transport terms is constant in x-direction, or when f_a equals 0, which is the case for a large bottom pool (see Figure 2.2).

Regarding the boundary conditions for Equation 2.28, a depth averaged concentration must be imposed at the seaward boundary ($x = 0$). At the landward boundary, $x = L$, the amount of sediments carried by the river can be prescribed.

$$\frac{1}{H+R} \int_{-H}^{R+\zeta} c dz = c_{sea} \tag{2.29}$$

$$B \int_{-H}^{R+\zeta} uc - K_h c_x = -\mathscr{F}_{river} \tag{2.30}$$

2.3. SOLUTION METHOD

Solutions to the equations presented in section 2.2 have been derived by Dijkstra et al. (2017) using a perturbation approach. This first step in that approach is scaling the equations using typical scales for the variables, such that the relative importance of different terms in the equations can be determined. For this scaling, it is assumed that the ratio of a typical water level amplitude ζ over the depth H is much smaller than 1:

$$\epsilon = \frac{\zeta}{H} \ll 1 \tag{2.31}$$

The most dominant terms in the equations will be called leading order terms, and are of $\mathcal{O}(1)$. After separating the leading order terms, the remaining terms contributing the most are called first-order terms and these are typically of $\mathcal{O}(\epsilon)$. The higher the order of the term, the less dominant its effects. Higher order terms are typically of $\mathcal{O}(\epsilon^n)$ $(n > 1)$.

The next step is to write the solutions for u, w, ζ and c as a power series of the small parameter ϵ like:

$$\begin{aligned} u &= u^0 + u^1 + u^2 + ... \\ w &= w^0 + w^1 + w^2 + ... \\ \zeta &= \zeta^0 + \zeta^1 + \zeta^2 + ... \\ c &= c^0 + c^1 + c^2 + ... \end{aligned}$$

in which u^0, w^0, ζ^0 and c^0 are of $\mathcal{O}(1)$, u^1, w^1, ζ^1 and c^1 of $\mathcal{O}(\epsilon)$ and so on. Additionally, the density ρ, settling velocity w_s, partial slip parameter s_f, eddy viscosity A_v and diffusivity K_v, and the forcing by the tide A and river discharge Q are written as similar series. By substituting these expressions into the scaled equations, a system of equations can be found in leading order, first order and higher orders. It turns out that this procedure leads to a system of linear equations at each order, which is much easier to solve than the original non-linear equations. Hence, by doing so, non-linearities can be approximated by a series of linear estimates. The linear character of the equations makes it possible to determine the effects of a single forcing mechanism, while the sum of the individual mechanisms is considered as the total solution. In this way, the relative importance of specific physical mechanisms can be evaluated by iFlow. Only the main results of the perturbation approach are presented in the next subsections. More detailed derivations are presented in Appendix A (for the hydrodynamics) and Appendix B (for the sediment dynamics).

2.3.1. HYDRODYNAMICS

Following the approach of the perturbation method, the different terms in the momentum equation have the following scales

$$\underbrace{u_t}_{\mathcal{O}(1)} + \underbrace{uu_x}_{\mathcal{O}(\epsilon)} + \underbrace{wu_z}_{\mathcal{O}(\epsilon)} = -\underbrace{g(R_x+\zeta_x)}_{\mathcal{O}(1)} - \underbrace{g\int_z^R \frac{\rho_x}{\rho_0}d\tilde{z}}_{\mathcal{O}(\epsilon)} - \underbrace{g\zeta\frac{\rho_x(R)}{\rho_0}}_{\mathcal{O}(\epsilon^2)} + \underbrace{(A_v u_z)_z}_{\mathcal{O}(1)} \tag{2.32}$$

Using Equation 2.32, we find the following expression for the leading order momentum equation

$$u_t^0 = -g(R_x^0+\zeta_x^0) + (A_v u_z^0)_z \tag{2.33}$$

with boundary conditions

$$A_v^0 u_z^0 = 0 \qquad \text{at } z = R \tag{2.34}$$

$$A_v^0 u_z^0 = s_f^0 u^0 \qquad \text{at } z = -H \tag{2.35}$$

Scaling the depth-averaged continuity equation results in the following typical scales

$$\underbrace{\zeta_t}_{\mathcal{O}(1)} + \underbrace{\frac{1}{B}\left(B\int_{-H}^R u dz\right)_x}_{\mathcal{O}(1)} + \underbrace{(B\zeta u_{z=R})_x}_{\mathcal{O}(\epsilon)} = 0 \tag{2.36}$$

from which the leading-order depth-averaged continuity equation can be derived as

$$\zeta_t^0 + \frac{1}{B}\left(B\int_{-H}^R u^0 dz\right)_x = 0 \tag{2.37}$$

with boundary conditions

$$\zeta^0 = \underbrace{A^0}_{\text{tide}} \qquad \text{at } x = 0 \tag{2.38}$$

$$B\int_{-H}^R u^0 dz = \underbrace{-Q^0}_{\text{river}} \qquad \text{at } x = L \tag{2.39}$$

A comparison of the leading-order equations (Equation 2.33 and Equation 2.37) with the original equations (Equation 2.1 and Equation 2.7) teaches us that the non-linear advection terms are not considered (yet). Furthermore, the dependency on ζ is neglected as well as the baroclinic forcing. By omitting these terms, the leading order equations have become linear and the only forcing terms left are the tidal forcing and river discharge. These forcing terms are denoted by underbraces in the above equations.

In a similar way, first-order equations can be derived for the momentum and depth-averaged continuity equation. Although Equation 2.32 shows that the non-linear advection terms will return into the first-order equations, the equations remain linear as a consequence of the power series for the parameters u, w, t and c. The first order momentum equation becomes

$$u_t^1 + u^0 u_x^0 + w^0 w_z^0 = -g\zeta_x^1 - g\int_z^0 \frac{\rho_x}{\rho_0}dz + (A_v^0 u_z^1)_z \tag{2.40}$$

Since the leading order terms already can be solved with the leading-order equations, the only unknowns in the first-order momentum equation are u^1, w^1 and ζ^1. Rewriting the first order equation such that known 'forcing' terms are on the right hand side gives:

$$u_t^1 + g\zeta_x^1 - (A_v^0 u_z^1)_z = -\underbrace{(u^0 u_x^0 + w^0 w_z^0)}_{\text{advection}} - \underbrace{g\int_z^R \frac{\rho_x}{\rho_0}dz}_{\text{baroclinic pressure}} \tag{2.41}$$

in which the forcing terms on the right hand side are recognised as the advection terms and the pressure gradient due to density gradients in along-channel direction. The following boundary conditions apply

$$A_v^0 u_z^1 = -\underbrace{(A_v^0 u_z^0)_z \zeta^0}_{\text{vel.-depth asym.}} \qquad \text{at } z = R \tag{2.42}$$

$$A_v^0 u_z^1 - s_f^0 u^1 = 0 \qquad \text{at } z = -H \tag{2.43}$$

Based on the scaling approach, the first-order depth-averaged continuity equation can be formulated as

$$\zeta_t^1 + \frac{1}{B}\left(B \int_{-H}^{R} u^1 \, dz + \underbrace{B u_{z=R}^0 \zeta^0}_{\text{tidal return flow}} \right)_x = 0 \tag{2.44}$$

for which the following boundary conditions apply

$$\zeta^1 = \underbrace{A^1}_{\text{tide}} \qquad \text{at } x = 0 \tag{2.45}$$

$$B \int_{-H}^{R} u^1 \, dz = \underbrace{-Q^1}_{\text{river}} - \underbrace{B u_{z=R}^0 \zeta^0}_{\text{tidal return flow}} \qquad \text{at } x = L \tag{2.46}$$

Regarding the first-order boundary conditions for both the width-averaged momentum equation and the depth-averaged continuity equation, multiple additional contributions due to non-linearities are recognized of which the advection term already has been mentioned. The velocity-depth asymmetry captures the effect of different velocity distributions during ebb and flood as a consequence of varying surface elevation, whereas the tidal return flow accounts for the flow compensating the Stokes drift. A more detailed explanation of the hinterlying physical processes is presented when first discussed in the results chapter 4 and chapter 5.

As a consequence of the assumption presented in Equation 2.31, the magnitude of higher order contributions reduces quickly for increasing order. For that reason, it is assumed that the sum of the leading-order and first-order contributions is a fairly accurate estimate of the total solution, as long as the scaling assumptions are valid. Higher order contributions are therefore considered out of scope for this research.

2.3.2. SEDIMENT DYNAMICS

Again using the perturbation approach, the typical order of magnitude of the different terms in the width-averaged sediment mass balance and the sediment concentration equilibrium condition are derived (Dijkstra et al., 2017). The most important findings are repeated below, whereas the derivations are presented in Appendix B.

WIDTH-AVERAGED SEDIMENT MASS BALANCE

The different terms in the dimensional width-averaged sediment balance typically have the following order of magnitude

$$\underbrace{c_t}_{\mathcal{O}(1)} + \underbrace{u c_x}_{\mathcal{O}(\epsilon)} + \underbrace{w c_z}_{\mathcal{O}(\epsilon)} = \underbrace{w_s c_z}_{(\mathcal{O}(1))} + \underbrace{(K_h c_x)_x}_{\mathcal{O}(\epsilon^2)} + \underbrace{\frac{B_x}{B} K_h c_x}_{\mathcal{O}(\epsilon^2)} + \underbrace{(K_v c_z)_z}_{\mathcal{O}(1)} \tag{2.47}$$

Therefore, we find the following set of equations at leading order, in which the unknown terms are presented on the left hand side of the equation

$$c_t^0 - (w_s^0 c^0 + (K_v^0 c_z^0))_z = 0 \tag{2.48}$$

with boundary conditions (linearised around the reference level R)

$$w_s^0 c^0 + K_v^0 c_z^0 = 0 \qquad \text{at } z = R \tag{2.49}$$

$$K_v^0 c_z^0 = \underbrace{E^0}_{\text{erosion}} \qquad \text{at } z = -H \tag{2.50}$$

At leading order, the erosion E^0 is the only forcing term, hence the leading-order erosion governs the leading-order sediment concentrations. E^0 depends on the erosion parameter M, the erodibility $f(a(x))$ and the leading-order bottom shear stress (which in turn depends on the leading order velocity):

$$E^0 = M|\tau_b^0(x,t)|f(a(x)) \tag{2.51}$$

At first order we find the governing equation

$$c_t^1 - w_s^0 c_z^1 - (K_v^0 c_z^1)_z = -\underbrace{(u^0 c_x^0 + w^0 c_z^0)}_{\text{sed. advection}} + w_s^1 c_z^0 \tag{2.52}$$

with boundary conditions (linearised around the reference level R)

$$w_s^0 c^1 + K_v^0 c_z^1 = -(w_s^0 c^0 + K_v^0 c_z^0)_z \zeta^0 \qquad \text{at } z = R \tag{2.53}$$

$$K_v^0 c_z^1 = \underbrace{-E^1}_{\text{erosion}} \qquad \text{at } z = -H \tag{2.54}$$

It should be noticed that the first-order sediment concentrations are not longer only dependent on the first-order erosion, but multiple different processes. The terms representing the sediment advection are named in the equations. Furthermore, we recognise a correction for applying the no-flux boundary condition at z = R instead of z = ζ. The other processes forcing the first-order sediment concentrations are due to covariances of the leading order sediment concentration with the surface elevation.

SEDIMENT CONCENTRATION EQUILIBRIUM CONDITION

Using a scaling approach for the sediment concentration equilibrium condition, following typical orders of magnitude are found for the different terms

$$\left\langle B \int_{-H}^{R} (\underbrace{uc}_{\mathcal{O}(\epsilon)} - \underbrace{K_h c_x}_{\mathcal{O}(\epsilon^2)}) dz \right\rangle_x = 0 \tag{2.55}$$

It can be observed that the equation vanishes at leading-order. The first-order equation reads

$$\left\langle B \int_{-H^*}^{R} (u^0 c^0) dz \right\rangle_x = 0 \tag{2.56}$$

in which the last term on the left hand side followed from linearisation by a Taylor expansion around the reference level R.

2.3.3. SOLUTION TECHNIQUES

To obtain maximum accuracy, the functions describing the width and the depth are computed analytically. However, not all modules included in the iFlow model used in this research can be solved analytically. Once numerical calculations are used, a computational grid is necessary. Different types of grids can be defined in iFlow, but only an equidistant grid is used. More accurate solutions are found using a finer computational grid, but the finer the grid, the longer the computational times. For both analytical and numerical results, an output grid needs to be defined on which the demanded parameters are saved. Dependent on the purpose of the output, the grid resolution can be defined, lower resolution limits the size of the output data. When multiple modules show a mutual dependency, e.g. sediment-induced turbulence damping which depends on the sediment concentrations which in turn depend on the turbulence, iFlow constructs an iteration loop. This iteration loop continues until a convergence criterion has been reached, after which the computation continues with the next step. Inclusion of such a mutual dependency results in a significant increase of the computational time as a consequence of the iterative character of the solving procedure.

2.4. ANALYSIS FRAMEWORK

The availability of sediments in the estuary depends on the along-channel transport. To reach high concentrations of suspended sediment however, available sediment should also be brought and kept in suspension. According to Dijkstra et al. (2018), sediment concentrations within an estuary can therefore be restricted due to either limited supply or due to limited erosion. Both aspects will be treated in the upcoming subsections.

2.4.1. TRANSPORT CAPACITY

By making certain assumptions about the external forcing (tides and river discharge), the solutions of the before introduced equations become well-analysable. Firstly, we restrict the external forcing to only consist of a subtidal signal, semi-diurnal and quarterdiurnal signal. As a consequence, the solutions to the set of equations can be written as a sum of the same components plus overtides. By only having an M_2 tidal forcing at leading-order, the leading-order velocities can be described with an M_2 tidal velocity signal. Leading-order hydrodynamics therefore describe the linear propagation of the M_2 tide through the estuary. At first order, the external forcing contains a subtidal (due to the river) and a quarterdiurnal (M_4 tide) velocity signal. Furthermore, the forcing by the baroclinic pressure and advection can be described as the sum of a M_0 and a M_4 signal as well (see derivation in section A.4). These first-order contributions are responsible for the tidal asymmetry.

Likewise, leading- and first-order sediment dynamics can also be described with (sub)tidal components (see section B.3). We found that the leading order sediment concentration only depends on the leading order erosion. The leading-order erosion is a function of the leading-order bed shear stress, which in turn depends on the absolute value of the leading-order velocities. The absolute value of the M_2 tidal velocities can be approximated using a Fourier series (see Appendix C). Consequentially, leading-order sediment concentrations contain M_0, M_4, M_8 etc. components. The first-order sediment concentration is not only forced by the first-order erosion, but also contains contributions due to sediment advection and due to covariances of the leading order sediment concentration with the surface elevation. All terms contain a similar correlation between a M_2 signal and the sum of a M_0 and M_4 signal. The first-order erosion can again be approximated by a Fourier series (see Appendix C). It follows that the first-order sediment concentrations contain M_2, M_6, M_{10} etc. components. An overview of the dependencies of the leading- and first order velocities and sediment concentrations is presented in Table 2.1.

Table 2.1: Components describing the velocities and concentrations at leading- and first order.

	$\mathcal{O}(1)$	$\mathcal{O}(\epsilon)$
u	M_2	M_0,M_4
c	M_0,M_4, etc.	M_2,M_6, etc.

Using the overview of Table 2.1, we can easily see that the sediment concentration equilibrium condition vanishes at first order (see Equation 2.56), since $\langle u^0 c^0 \rangle = 0$. Therefore, the second-order equation is necessary to calculate the erodibility of sediments, which reads, after integrating with respect to x using the upstream boundary (assuming $\mathcal{F}_{river} = 0$)

$$\left\langle B \int_{-H}^{R} (u^1 c^0 + u^0 c^1 - K_h^0 c_x^0) dz + [\zeta^0 u^0 c^0]_{z=R} \right\rangle = 0 \tag{2.57}$$

where c^0 and c^1 depend on f. According to Brouwer et al. (2018), c^0 and c^1 can be written as

$$c^0 = c_f^0 f \tag{2.58}$$

$$c^1 = c_f^1 f + c_{f_x}^1 f_x \tag{2.59}$$

in which c_f is the suspended sediment concentration at capacity conditions (i.e. with an abundance of easy erodible sediment on the bed), and c_{f_x} is the along-channel dispersion at capacity conditions.

From this, f can be solved by rewriting Equation 2.57 into

$$Tf + Ff_x = 0 \tag{2.60}$$

in which

$$T = \left\langle \int_{-H}^{R} (u^1 c_f^0 + u^0 c_f^1 - K_h^0 (c_f)_x^0) dz + [\zeta^0 u^0 (c_f)^0]_{z=R} \right\rangle = 0 \tag{2.61}$$

$$F = \left\langle \int_{-H}^{R} u^0 c_{f_x}^1 - K_h c_f^0 dz \right\rangle = 0 \tag{2.62}$$

The equations for T and F both contain advective and diffusive transport terms, in which c_f and c_{f_x} mean that the concentration scales linearly with the erodibility f or with its gradient in along-channel direction respectively. Regarding the transport function T, see Equation 2.61, three different terms can be recognised. We start by discussing $\langle\int_{-H}^{R} -K_h^0 c_x^0 dz$, in which the horizontal eddy diffusivity is recognised. This diffusive transport term describes a horizontal background diffusion, representing flows (e.g. lateral circulation) which is not solved for. Then there is the term, $\langle\zeta^0 u^0 c^0\rangle$, representing the sediment transport due to Stokes drift, which is counteracted by a tidal return flow. This tidal return flow is included in the remaining terms, $\langle\int_{-H}^{R}(u^1 c^0 + u^0 c^1)dz\rangle$, mainly describing the transport due to interactions between first-order velocity and leading-order sediment concentration, and leading-order velocities and first-order sediment concentration. We have seen that these velocities and concentrations are influenced by multiple contributions of which an overview is presented in Table 2.2. Since the first-order erosion depends on the first-order velocity, the first-order erosion contains contributions of all processes that contribute to the velocity at first-order. These contributions are not presented individually in the overview below, but will be referred to as $(c_{ero}^{12})_{contribution}$ when used in the remainder of this report.

Table 2.2: An overview of the forcing mechanisms and and the frequencies for the leading- and first order velocities and sediment concentrations.

	Velocity u			**Sediment concentration c**		
	Mechanism	Frequency	Notation	Mechanism	Frequency	Notation
Leading-order	Tide	M_2	u^{02}	Erosion	M_0, M_4	c_{ero}^{00}, c_{ero}^{04}
First-order	Baroc. press.	M_0	u_{baroc}^{10}	Sed. adv.	M_2	c_{sedadv}^{12}
	River	M_0	u_{river}^{10}	Erosion	M_2	c_{ero}^{12}
	Advection	M_0, M_4	$u_{adv}^{10}, u_{adv}^{14}$			
	Vel.-depth asym	M_0, M_4	$u_{vel.dep}^{10}, u_{vel.dep}^{14}$			
	Tidal return flow	M_0, M_4	$u_{return}^{10}, u_{return}^{14}$			
	Tide	M_4	u_{tide}^{14}			

The magnitude of the sediment transport due to the different processes described before depends on the actual sediment concentrations, which in turn depend on the erodibility f. Using the transport function T, called the transport capacity, and assuming that there is an excessive amount of easy erodible sediment on the bed, this sediment concentration dependency can be excluded. The transport capacity can then be interpreted as the tendency of the system to redistribute sediments over the estuary, which is mainly governed by the hydrodynamics and sediment parameters (distribution over water column). Sediments tend to accumulate in so called trapping zones; locations where the transport capacity converges. Expressions for the individual contributions to the transport capacity are found by substituting the terms presented in Table 2.2 into Equation 2.61. An overview of the individual contributions to the transport capacity is presented below:

$$T_{tide} = \int_{-H}^{R} \left\langle \underbrace{u^{02}(c_{ero}^{12})_{tide}}_{\text{external } M_2 \text{ tide}} + \underbrace{u_{tide}^{14} c_{ero}^{04}}_{\text{external } M_4 \text{ tide}} \right\rangle dz \tag{2.63}$$

$$T_{baroc} = \int_{-H}^{R} u_{baroc}^{10} c_{ero}^{00} + \langle u^{02}(c_{ero}^{12})_{baroc}\rangle dz \tag{2.64}$$

$$T_{sedadv} = \int_{-H}^{R} \langle u^{02} c_{sedadv}^{12}\rangle dz \tag{2.65}$$

$$T_{return} = \int_{-H}^{R} u_{return}^{10} c_{ero}^{00} + \left\langle u_{return}^{14} c_{ero}^{04} + u^{02}(c_{ero}^{12})_{return} - \underbrace{[\zeta^{02} u^0 2 c_{ero}^{00} + \zeta^{02} u^0 2 c_{ero}^{04}]_{z=R}}_{\text{Stokes drift}} \right\rangle dz \tag{2.66}$$

$$T_{vel.-depth} = \int_{-H}^{R} u_{vel.dep}^{10} c_{ero}^{00} + \left\langle u_{vel.dep}^{14} c_{ero}^{04} + u^{02}(c_{ero}^{12})_{vel.dep} \right\rangle dz \tag{2.67}$$

$$T_{river} = \int_{-H}^{R} u_{river}^{10} c_{ero}^{00} + \langle u^{02}(c_{ero}^{12})_{river}\rangle dz \tag{2.68}$$

Towards the landward boundary of the estuary, the erosion due to the tidal velocities reduces, and the erosion by the river becomes important. Sediments eroded by the river, are transported downstream by the river. Although this term is of fourth-order, it is included by the model with the subtidal transport capacity term which reads

$$T_{river-river} = \int_{-H}^{R} \langle u^1_{river} c^2_{river-river} \rangle \, dz \tag{2.69}$$

Note: including only one fourth-order term breaks the consistency of the scaling approach, hence model results must be treated with care.

To investigate the influence of a spring-neap tidal cycle on the trapping of sediments within estuaries, Bouwman (2019) derived expressions for the subtidal dependency of the different contributions to the transport capacity as a function of the tidal amplitudes at the seaward boundary. Since the difference between spring and neap tidal conditions is addressed in this research as well, the most important outcomes are repeated in Table 2.3.

Table 2.3: Overview of the subtidal dependency for the contribution to the total transport capacity of different physical processes. Source: Bouwman (2019)

Contribution		Subtidal dependency
$T_{ext.M2-tide}$	$\propto$	$\lvert A_{M_2}\rvert \cdot \lvert A_{M_4}\rvert e^{-i(\phi_{M_4}-2\phi_{M_2})}$
$T_{ext.M4-tide}$	$\propto$	$\lvert A_{M_2}\rvert \cdot \lvert A_{M_4}\rvert e^{i(\phi_{M_4}-2\phi_{M_2})}$
T_{baroc}	$\propto$	$\lvert A_{M_2}\rvert$
T_{sedadv}	$\propto$	$\lvert A_{M_2}\rvert^3$
$T_{vel.-depth}$	$\propto$	$\lvert A_{M_2}\rvert^3$
T_{return}	$\propto$	$\lvert A_{M_2}\rvert^2$
T_{river}	$\propto$	$\lvert A_{M_2}\rvert$

2.4.2. DIMENSIONLESS EROSION PARAMETER AND HINDERED SETTLING

By only focussing on the vertical processes, the ability of the flow to bring or keep sediments in suspension is based on a balance between erosive and depositional fluxes. For high sediment concentrations, interaction between sediment flocs results in hindered settling. Richardson and Zaki (1954) presented a parametrisation for this hindered settling which reads

$$w_s = w_{s,0}(1-\phi)^m \tag{2.70}$$

in which $w_{s,0}$ is the clear-water settling velocity, ϕ the volumetric fraction of flocs defined as c/c_{gel} and m an empirical based value, often chosen $m = 5$ for fine sediments. The gelling concentration c_{gel} is characterised as the concentration at which the fluid-sediment mixture starts to develop strength, typically around concentrations of 100 g/l.

By assuming periodic conditions for the flow and concentrations, Dijkstra et al. (2018) has been able to describe a relation between the tidally averaged near-bed concentration ϕ_{bed} and a dimensionless erosion parameter $\tilde{E}$ including the effects of hindered settling.

$$\langle (1-\phi_{bed})^m \phi_{bed} \rangle = \Bigg\langle \underbrace{\frac{M}{w_{s,0} c_{gel}} |\tau_b|}_{\tilde{E}} \Bigg\rangle \tag{2.71}$$

The maximum near-bed concentration can be found by taking the derivative of the left hand side and setting this equal to zero

$$\begin{aligned} \langle \rangle \left((1-\phi_{bed})^5 \phi_{bed} \right)_{\phi} \rangle &= 0 \\ \langle -5(1-\phi_{bed})^4 \phi_{bed} + (1-\phi_{bed})^5 \rangle &= 0 \\ \rightarrow \langle \phi_{bed} \rangle &= \frac{1}{6} \end{aligned}$$

Likewise, the value of the dimensionless erosion parameter for which such concentration can be found equals

$$\left(1-\frac{1}{6}\right)^5 \frac{1}{6} = 0.067$$

which is referred to as $\tilde{E}_{crit}$. It should be noted that this value only holds when fluctuations on the tidal scale are not considered.

By assuming an abundance of easy erodible sediment on the bed, for $\tilde{E} < \tilde{E}_{crit}$ the near-bed sediment concentration depends on the dimensionless erosion parameter. However, another solution exists within the same range of values for $\tilde{E}$, resulting in much higher near-bed concentrations. Nevertheless, these solutions do not describe a stable state and the system tends to move towards the earlier described state in which the near-bed concentration depends on the dimensionless erosion parameter. For $\tilde{E} > \tilde{E}_{crit}$, the near-bed concentration becomes theoretically unbounded, which in practice results in supply limited concentrations. These high sediment concentrations could be reached due to a positive feedback loop caused by the effects of hindered settling. Increased erosion results in higher sediment concentrations, and accordingly lower deposition rates due to hindered settling, hence an increasing net erosion rate. This increase in the net erosion rate further increases the sediment concentrations and therefore increases the effect of hindered settling.

3

DATA ANALYSIS AND MODEL SET-UP

In this chapter, all data necessary for setting up an iFlow model describing the Loire estuary will be discussed. An overview of the parameters that are actually used in the iFlow model is presented in section 3.3. Regarding the current state of the estuary, data is necessary which represents the essential hydrodynamics and sediment dynamics in a qualitative way, i.e. water levels, sediment concentrations, salinity etc. Even coarser data, for example general trends in tidal range, sediment concentrations and bottom levels suffice for historical states, since extensive sensitivity studies can be performed to cover the uncertainty (see section 1.4).

The model domain is bounded on the downstream side where the Loire mouths into the sea (Saint-Nazaire), while the upstream boundary is located at Ponts-de-Cé (147 km from the mouth). An overview with the important measurement stations/locations throughout the Loire estuary (up to Nantes) is presented in Figure 3.1. These stations will be mentioned multiple times throughout this chapter.

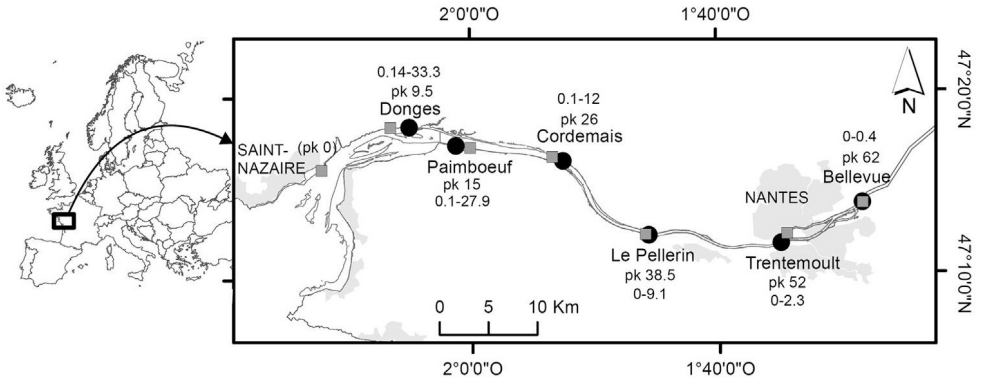

Figure 3.1: Map of the Loire River estuary up to Nantes, with, in black, measurement stations from the SYVEL network and, in grey, tidal gauges. From Jalón-Rojas et al. (2016).

Before the data is presented, we should pay some attention to the different reference levels used in France over the years and how these different reference levels relate to each other. The two most important reference levels found in the data are IGN69 on the one hand, coming from the terrestrial system, and 'Cote Marine' on the other hand, originating from the marine system. Regarding the 'Cote Marine' reference level, distinction can be made between CM (before 1996) and CM96 (after 1996) in which the zero-level of CM is 0.4 m above the zero-level of CM96. According to GIP (2002a), there is a 3.16 m difference between CM96 and IGN69. Data presented by Jalón-Rojas et al. (2016) shows that the current average water level at Saint-Nazaire, referred to as mean sea level (MSL), is 3.6 metres above the old CM between 2007 and 2013. This results in a difference between CM96 and MSL of 4 m and a difference between IGN69 and MSL of approximately 0.8 m. For clarity, we present all data with respect to MSL.

3.1. GEOMETRY

All data concerning depth has been gathered by digitalising graphs describing the thalweg of the Loire, mainly from bulletins presented by the "Groupement d'Intérêt Public (GIP) Loire Estuaire", and converting this to depths with respect to MSL. The data describing the current depth of the Loire estuary is presented in Figure 3.2. The orange dots are based on a graph from GIP (2014a,b), the red dots from GIP (2011a) and the purple dots from GIP (2013). Furthermore, the brown dots correspond to the bathymetry used by Le Hir and Karlikow (1992). It should be noted that the dates of publication and the dates of measurements presented in Figure 3.2 do not match. A smooth curve has been fitted through the data as a representative of the depth for use in iFlow. We have chosen a function that consists of two parts: a fifth-order polynomial and a straight line. The level and the slope of the two parts are equal at the transition point x_l:

$$H = \begin{cases} 6.670 \cdot 10^{-22} x^5 - 1.037 \cdot 10^{-16} x^4 + 5.402 \cdot 10^{-12} x^3 - 1.009 \cdot 10^{-7} x^2 + 1.816 \cdot 10^{-4} x + 17.235 & \text{x} \leq 57.5 \text{ km} \\ -2.462 \cdot 10^{-4} (x - 57453) + 6.726 & \text{x} > 57.5 \text{ km} \end{cases} \tag{3.1}$$

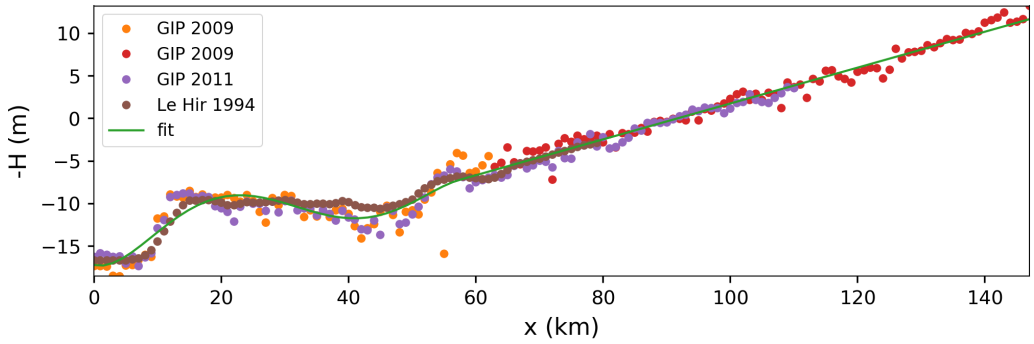

Figure 3.2: Actual Thalweg level with respect to mean sea level at Saint-Nazaire, which is approximately at CM96 +4.0 m. Sources: GIP (2011a), GIP (2013), GIP (2014a,b) and Le Hir and Karlikow (1992).

An overview of the data around the year 1900 is presented in Figure 3.3, in which the orange dots represent a graph presented in GIP (2011a), the red dots are based on data of GIP (2004) and the purple dots are from a report of CSEEL (1984). To represent this depth profile in iFlow, we have again fitted a curve consisting of a fifth-order polynomial and a straight line:

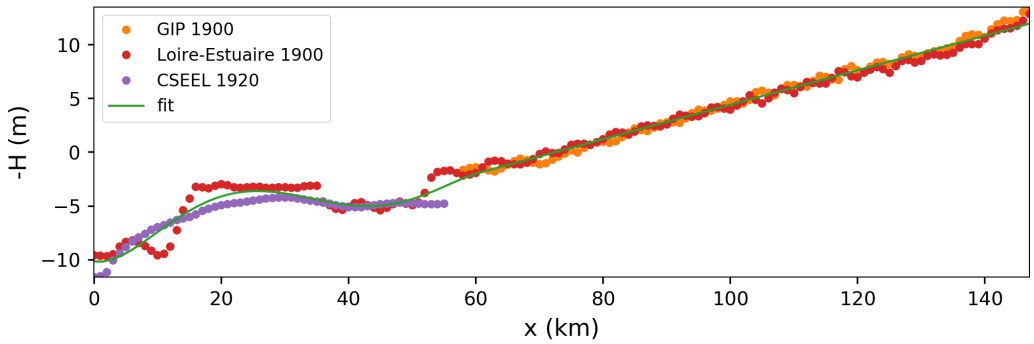

Figure 3.3: Thalweg level around the year 1900 with respect to current mean sea level at Saint-Nazaire, which is approximately at CM96 +4.0 m. Sources: CSEEL (1984), GIP (2004), GIP (2011a)

$$H = \begin{cases} 3.370 \cdot 10^{-22} x^5 - 5.590 \cdot 10^{-17} x^4 + 3.118 \cdot 10^{-12} x^3 - 6.247 \cdot 10^{-8} x^2 + 9.31 \cdot 10^{-5} x + 10.181 & \text{x} \leq 60.5 \text{ km} \\ 1.654 \cdot 10^{-4} (x - 60564) + 1.850 & \text{x} > 60.5 \text{ km} \end{cases} \tag{3.2}$$

Only little bathymetrical data is available for the period between 1900 and 2010, and the data which is available is inaccurate. For example, for the depths of the years 1920, 1949, 1969 and 1976 mentioned in CSEEL (1984), it is unclear how they relate to the thalweg levels, and the bathymetrical maps of the years 1947, 1957, 1969 and 1982 presented by Sogreah (2006) are to coarse to extract depth profiles from. However, if we assume that the deepening was a gradual process, bottom profiles can be made up for intermediate years by means of linear interpolation using Equation 3.3 (Dijkstra et al., 2019c).

$$d_{year}(x, \alpha) = (1 - \alpha) d_{1900}(x) + \alpha d_{2000}(x) \tag{3.3}$$

As already introduced in section 1.2, different dredging campaigns responsible for the deepening of the Loire river have been reported. The most important deepening campaigns are repeated in Figure 3.4. These deepening campaigns are not equally distributed over time. To get an indication of the development of the bottom over the last century, four key years have been selected: 1900, 1949, 1970, 2000. The last four columns of Figure 3.4 present which measures are taken into account for each of the four key years. By comparing the depths reported for the deepening campaigns with the bathymetries corresponding to varying α, we find that α=0.5 more or less corresponds to 1949 and α=0.75 to 1971 (see Figure 3.5). Since significant deviations between the dredging levels and the estimated bathymetries can be observed, this should be interpreted as a first rough indication of the link between alpha and years. A more detailed analysis will be discussed in chapter 5.

Year	Intervention	Historic Scenario			
		1900	1949	1970	2000
1750-1840	Closing off second river arms				
1890	Exterior section at CM96 -5.1 m				
1896	Exterior section dredged to CM96 – 5.6 m				
1898-1899	Embanked section dredged to attain CM96 -1.2 m				
1906-1912	Intermediate channel deepened from CM96 +0.9 m to CM96 -2.1 m				
1913-1920	Creation of 'Bassin de Marée' upstream of Nantes				
1940	Lower section deepened to CM96 -6.5 m				
1942	Exterior section deepened to CM96 -8 m				
1948-1968	Intermediate and Embanked sections deepened from CM96 -2.6 m to CM96 -5.1 m				
1969-1973	Exterior section deepened to CM96 -9.4 m Lower section deepened to CM96 -9.35 m Intermediate and Embanked sections deepened to CM96 -5.6 m				
1978-1980	Exterior section deepened to CM96 -12.85 m Lower section deepened to CM96 -12.85 m				
1985-1986	Exterior section deepened to CM96 -13.7 m				

Figure 3.4: Schematic overview of the different deepening campaigns, with in the last four columns a selection which measures are included in the Loire bottom profiles

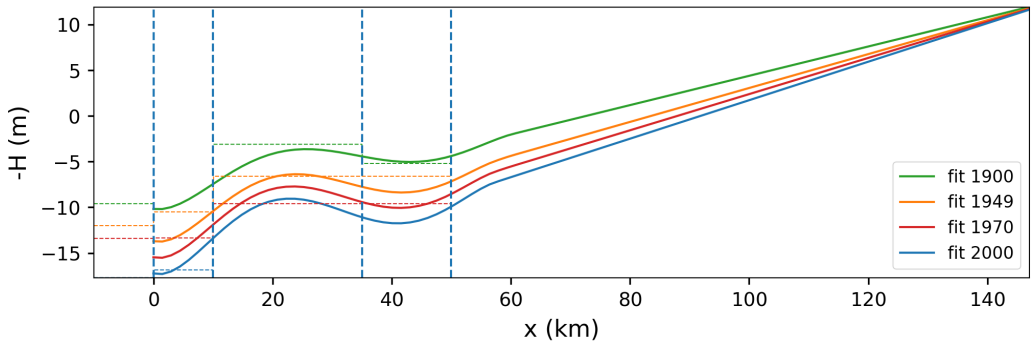

Figure 3.5: Evolution over the last century of the Thalweg level with respect to mean sea level at Saint-Nazaire, which is approximately at CM96 +4.0 m. The horizontal dashed lines correspond to the depth obtained with the deepening campaigns taken into account for the bathymetry of each the key years. The vertical dashed lines represent the five sections in which the estuary can be divided, namely the exterior-, lower-, intermediate-, embanked and upstream section.

The width of the estuary represents the width of the channel, and therefore we do not include intertidal areas in the width of the estuary. The width has been estimated using satellite images (Google Earth) as presented in Figure 3.6. The blue dots represent the full width of the river (without side channels), whereas the red dots resemble the width of the estimated main channel, but without the vast shallow area at the mouth of the estuary. Furthermore, measurements of Van den Bruweane (2019) are shown in Cyan, which correspond well to the estimation of the full river width based on Google Earth images. The best fit through the narrow data set is represented by a third-order polynomial:

$$B = -1.411 \cdot 10^{-12} x^3 + 4.002 \cdot 10^{-7} x^2 - 3.419 \cdot 10^{-2} x + 1.178 \cdot 10^3 \tag{3.4}$$

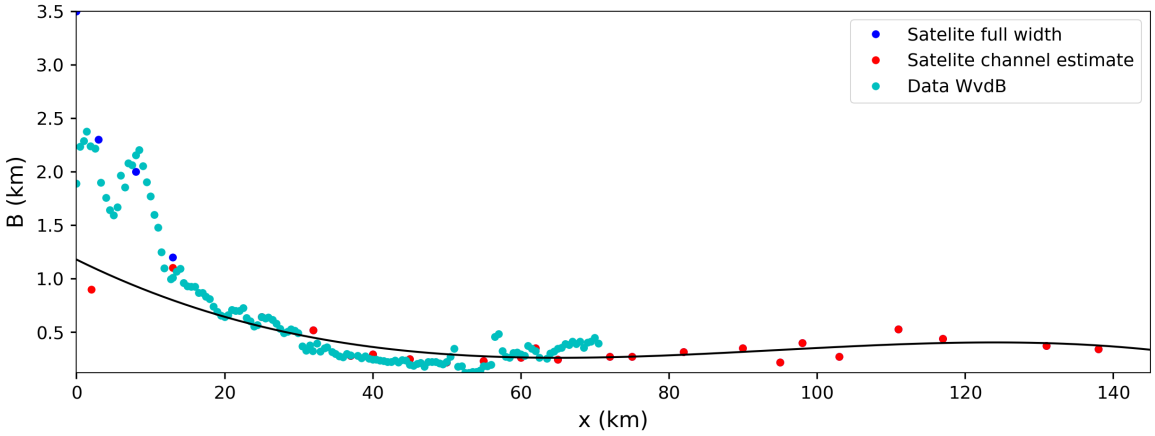

Figure 3.6: The width of the Loire estuary based on satellite images (Google Earth) in 2016

The most important human interventions that directly influenced the flow carrying width of the Loire river date back to before 1915. Measurements presented by Sogreah (2006) show that the river width measured at mean water level only changed slightly in the first 20 km since 1947. The data collected about the current width showed the presence of intertidal areas in the same region. Since intertidal areas are vulnerable to changes in hydraulic conditions, and these hydraulic conditions have changed drastically (recall the large observed tidal amplification), it is likely to account these minor changes in the river width to changes in the intertidal areas. Based on this reasoning, and pointing out that intertidal areas were not taken into account for the river width, it is assumed that the channel width remained more or less constant over the last century.

3.2. HYDRODYNAMICS

In this section, an overview will be presented of the available data on river discharge, propagation of the tide throughout the estuary and subtidal set-up, both for the current situation and for historical situations.

3.2.1. RIVER DISCHARGE

River discharge data of 2007 to 2013, measured at the station of Montjean-sur-Loire, have been used to determine average discharges. This resulted in a long term average discharge of 910 m^3/s, a summer(July-October) discharge of 300 m^3/s and a winter discharge of 1300 m^3/s. These values correspond quite well to the values based on a record of discharges that finds its origin in 1863, mentioned by Artelia (2013), with an average of 844 m^3/s. The deviation between the two mentioned yearly averages can be ascribed to the large observed inter annual variability in the data set of 2007 to 2013, which is clearly visible in Table 3.1 and Figure 3.7. Regarding the measurements performed by DREAL (2019) from 1863 onward, no significant changes in river discharge are observed over the last century.

Table 3.1: Frequency of occurrence per discharge in the Loire river, from DREAL (2019)

Frequency	**0.99**	**0.98**	**0.95**	**0.90**	**0.80**	**0.70**	**0.60**	**0.50**	**0.40**	**0.30**	**0.20**	**0.10**	**0.05**	**0.02**	**0.01**
Discharge m^3/s	3850.0	3240.0	2470.0	1870.0	1300.0	975.0	750.0	570.0	445.0	334.0	247.0	177.0	145.0	115.0	100.0

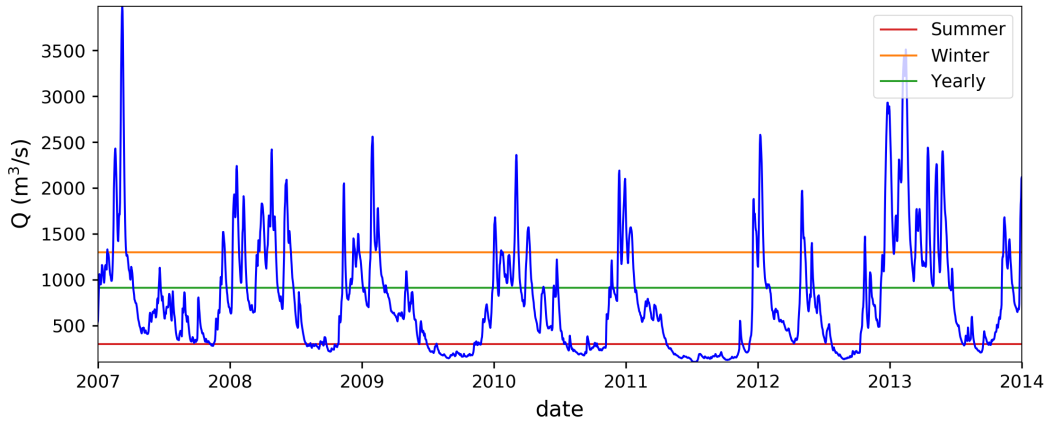

Figure 3.7: River discharge of the Loire between 2007 and 2014 measured at Montjean-sur-Loire, with, in red, the average summer discharge, in cyan, the average winter discharge, and in green, the long term average. Source: Jalón-Rojas et al. (2016)

3.2.2. TIDE

A tidal analysis has been performed by means complex demodulation, based on water levels at seven stations between Saint-Nazaire and Nantes obtained in a study by Jalón-Rojas et al. (2016). The method of complex demodulation as presented by Gasquet and Wootton (1997) provides the possibility to filter out certain tidal time-scales from a signal, instead of strict tidal frequencies. In this way, we are able to capture the variations of the semi-diurnal tide over a spring-neap cycle in terms of an approximately semi-diurnal signal that varies subtidally. In this thesis, we assume that average spring and neap tidal conditions can be approximated by firstly taking the highest and lowest 40 percent of the semi-diurnal water level amplitudes for spring and neap tide respectively, and than taking the median of each as a representative value. These values will be referred to as the M_2 tidal amplitudes for spring and neap tide. Next to M_2 amplitudes, this method of complex demodulation allows to filter out the subtidal set-up (called M_0), and amplitudes and phases of higher harmonics. In this report the only higher harmonic that is considered is the quarter-diurnal (M_4). Based on the highest and lowest 40 percent of the M_2 amplitude, the signals of the M_0 and $M4$ amplitudes as well as those of the M_2 and M_4 phases are divided into spring and neap tidal signals. By taking the median of these signals, representative values are found for the spring and neap tide amplitudes/phases of the remaining tidal constituents.

Further investigation of the tidal data reveals a strong relation between the tidal intrusion and the river discharge. As can be seen in Figure 3.8, during winter conditions (i.e. high river discharges, shaded green area), the low water levels are significant higher than the low water levels during summer conditions (shaded red area). The high water levels are much more constant over the year. Thus, we observe a strong seasonally varying tidal range in the upper part of the estuary.

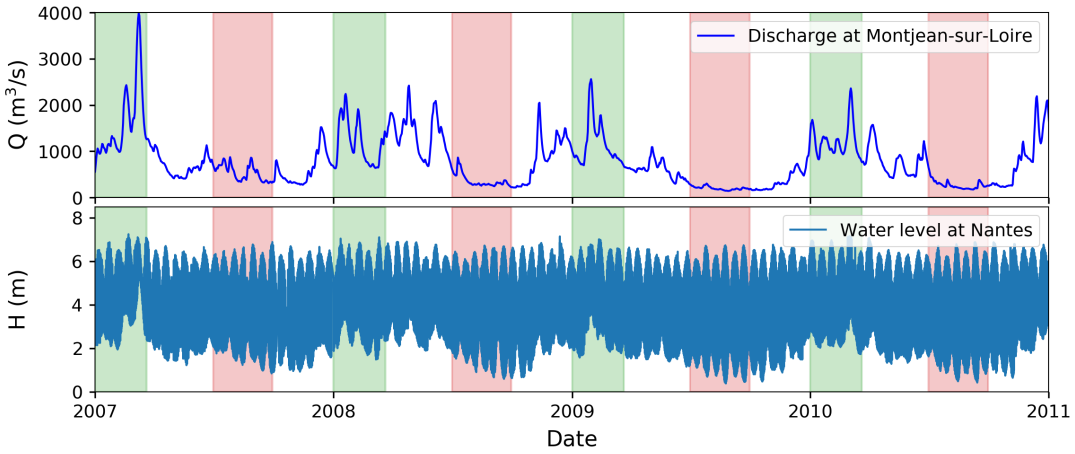

Figure 3.8: The river discharge at Montjean-sur-Loire in m^3/s (upper panel) and the water levels (m CM96) and Nantes (52 km, lower panel) in the period 2007-2011. Summer and winter periods are represented by the red and green shaded areas respectively.

To get a clear image of the seasonal and spring-neap dependency of the tidal intrusion, the tidal analysis has been repeated for summer and winter, and spring and neap data separately. A comparison of the propagation of the tide into the estuary for the different situations is presented in Figure 3.9. Regarding the M_2 water level amplitudes (upper panels) this seasonal dependency is can be seen clearly for both spring and neap tide. The M_4 signal on the other hand does only present some slight seasonal dependency for spring tides. Regarding the phases (lower panels), the M_2 phase is relatively constant over the year, whereas the M_4 phase depends on the season in the more upstream part of the estuary.

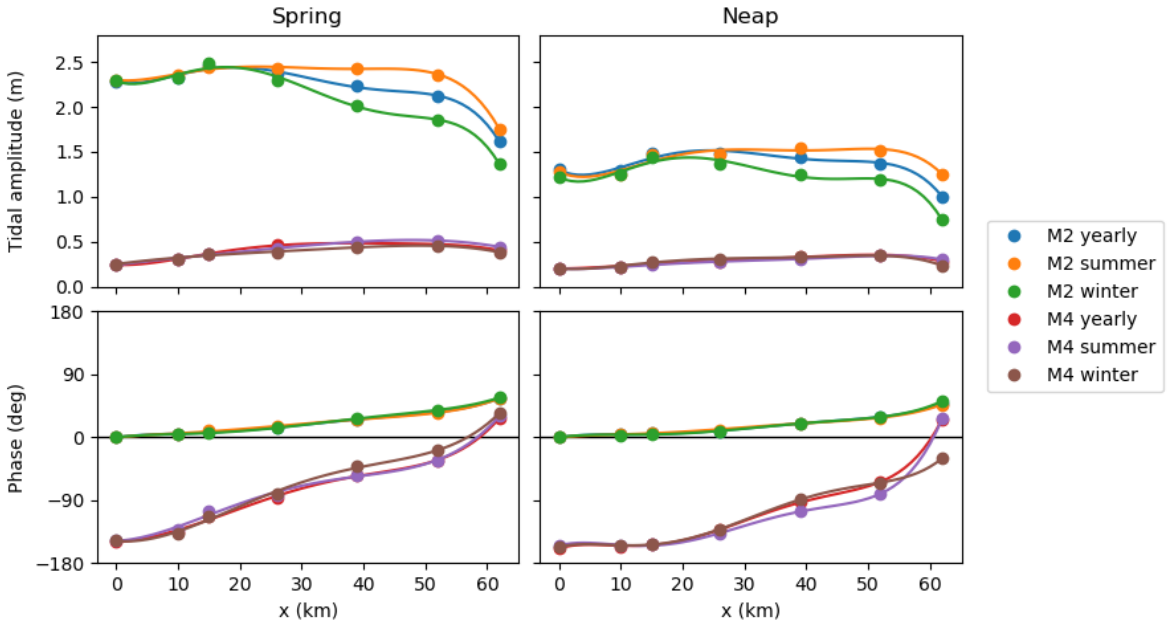

Figure 3.9: A comparison between winter, summer and yearly tidal data of amplitudes and phases of the M2 and M4 tidal components. In the horizontal direction, distinction has been made between spring- and neap tidal data. In the upper half of the figure, the water level amplitudes are presented and in the lower half the water level phases.

Since this research focuses on relatively lower river discharges, we focus on the tidal analysis based on the summer data. The results obtained with the method of complex demodulation are presented in Table 3.2.

Table 3.2: Tidal amplitudes and phases along the Loire estuary based on data obtained during summer conditions. Source: Jalón-Rojas et al. (2016)

			St Nazaire	Donges	Paimboeuf	Cordemais	Le Pellerin	Nantes	St Luce
		km	0	10	15	26	39	52	62
M0	Amp	Spring	0.0	0.02	0.14	0.13	0.20	0.27	0.61
		Neap	0.0	0.02	0.15	0.12	0.18	0.23	0.53
M2	Amp	Spring	2.30	2.35	2.44	2.43	2.43	2.36	1.75
		Neap	1.28	1.24	1.47	1.47	1.54	1.52	1.25
	Phase	Spring	0	4.5	10	15	26	35	56
		Neap	0	3.5	6.5	11	20	28	47
M4	Amp	Spring	0.24	0.31	0.36	0.42	0.50	0.51	0.44
		Neap	0.20	0.21	0.25	0.27	0.31	0.34	0.30
	Phase	Spring	-148	-132	-105	-82	-54	-33	31
		Neap	-155	-155	-154	-138	-106	-81	27

WATER LEVELS IN THE NON-TIDAL RIVER

In a bulletin of GIP (2002b), water levels are presented in the more upstream part (riverine part) of the Loire for multiple conditions in the years 2000-2001. The water levels according to a common summer discharge and a yearly average discharge are presented in Table 3.3.

Table 3.3: Water levels (m IGN69) along the riverine part of the Loire for different river discharges.

	Q (m^3/s)	Ancenis	Saint Florent	Ingrandes	Montjean-sur-Loire	Chalonnes	La Possoniere	La Pointe	Les Ponts-de-Cé
km		90	103	112	116	122	131	139	147
	250	-	6.16	7.55	8.18	10.25	11.33	12.9	15.13
	850	5.75	8.29	9.76	10.33	12.1	13.08	14.73	16.39

The water levels in the upstream part of the estuary have decreased significantly over the last century according to measurements presented in the same bulletin. Measurements obtained between 1900 and 1998 for a river discharge of 177 m^3/s show a drop in water levels which decreases towards Les Ponts-de-Cé. This decrease water level corresponds quite well to the decrease in bottom levels observed in the upstream part of the estuary (see Figure 3.4).

Table 3.4: Change (Δ) in water level (m) along the riverine part of the Loire for a river discharges of 177 m^3/s.

	Ancenis	Saint Florent	Ingrandes	Montjean-sur-Loire	Chalonnes	La Possoniere	La Pointe	Les Ponts-de-Cé
km	90	103	112	116	122	131	139	147
Δ (m)	-3.1	-2.6	-2.4	-2.1	-1.4	-1.6	-1.6	-0.6

3.2.3. VELOCITY

Although no measurements were found regarding flow velocities in the Loire in the current state, an impression is obtained from 3D model results and historical measurements. The measurements presented by CSEEL (1984) are flow velocities near the water surface observed in 1976, and the predictions made with the 3D model of Sogreah (2010) are depth averaged velocities obtained for the current bathymetry. Both the measurements as the model results are depicted in Figure 3.10. The predictions of Sogreah (2010) show relatively high flood velocities between km 10 and 50, whereas the maximum ebb velocities are found in the first 20 km. The measurements of CSEEL (1984) firstly point out the difference in velocities during spring and neap tides. Secondly, the ebb velocities observed at the surface in 1976 were larger than the flood velocities. For discharges larger than 2000 m^3/s, the velocities are even directed seaward throughout the entire tidal cycle (not shown).

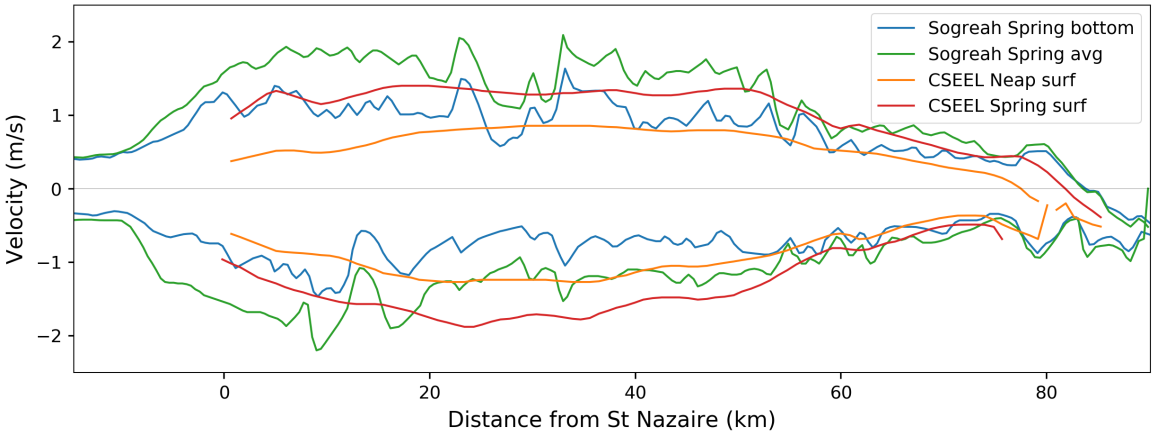

Figure 3.10: Maximal velocity measurements and predictions along the Loire estuary for different tidal conditions and locations in the water column, with positive velocities directed in landward direction. The blue (0.5 m above the bottom) and green (depth averaged) curves represent maximum and minimum velocities predicted by a 3D model of Sogreah (2010) during spring tide conditions and low river discharge (Q=189 m^3/s). The orange and red curves represent velocity measurements at the surface presented by CSEEL (1984) for spring and neap tide respectively, with a river discharge of 80 m^3/s.

3.2.4. TURBIDITY

As already introduced in section 1.2, a significant increase in turbidity at the surface has been observed in the 20th century, especially since the 1990s. This section will treat this development of turbidity along the estuary over time in more detail. Additionally, a certain band width of turbidity values will be provided for the downstream and upstream boundaries, which are necessary for setting up an iFlow model.

DEVELOPMENT OVER TIME

For the first part of the century, hardly any measurements were found regarding turbidity. Probably the first investigator of turbidity in the Loire estuary was Leopold Berthois around 1950 (Guilcher, 1988). Measurements of Berthois and Barbier (1953); Berthois (1955b) show that the turbid zone could be found up to Le Pellerin (39 km inland) with its maximum slightly downstream of Cordemais (26 km inland, see Figure 1.4) in 1952 during spring tide and low river discharges. During low water, sediment concentrations in the ETM could reach 0.7 g/l at the surface and 3 g/l near the bottom. Averaged over a complete tidal cycle these values reduce to approximately 0.25 g/l and 1 g/l, respectively. During winter conditions (high river discharge) the sediment is distributed much more uniform over the water column, but stays below 0.2 g/l and is expelled towards Saint Nazaire (Berthois, 1954, 1955b).

According to Berthois (1958) the location of the turbid zone depends on the tidal coefficient (measure for the tidal range at Saint-Nazaire), the river discharge and the viscosity of the water. Maximal intrusion of the turbid zone will be found if the river discharge remains low for some time (order of months), accompanied with a high tidal coefficient (i.e. large tidal range) and high water temperatures (around 20 °C). Although most of the concentrations mentioned by Berthois do not exceed 1 g/l, Berthois (1955b) mentions maximum turbidity values near Cordemais (26 km inland) of 2.226 g/l during winter and 20.46 g/l during summer. Unfortunately, no clarification is provided about the exact moment and position in the water column at which these measurements are taken, but it is good to note that high sediment concentrations could occur in the 1950s.

In the 1970s, suspended matter in the Loire estuary was extensively studied by Bertrand Gallenne. Measurements presented in his PhD thesis show that the turbid zone could reach up to Nantes with its maximum still around Cordemais (Gallenne, 1974a). A measurement campaign executed in 1972, presented by Gallenne (1974b), provides sediment concentrations that are partly in accordance with those of Berthois and Barbier (1953). On the one hand, concentrations of 0.3 g/l have been recorded at the surface somewhat downstream of Nantes (40 km inland) during low river discharge and at the start of low water, whereas the turbid water is expelled towards the open sea for high river discharges resulting in concentrations at the surface up to 0.9 g/l near Saint Nazaire.

In the early 1980s, ecological observations on plankton of the Loire estuary have been made by Rincé et al. (1989). From their samples, also suspended matter concentrations have been calculated. Their tidally averaged data shows concentrations at the surface between Saint-Nazaire and Cordemais up to 0.7 g/l. When the river discharge remains low for two consecutive months, the concentrations in the downstream estuary (between Saint Nazaire and Donges) drop to 0.1 g/l. Comparable data was found by Saliot et al. (1984), which has been presented in Figure 1.4. According to Migniot (1993) and Paape (1994), tidally averaged concentrations near the surface in the range 0.3-0.7 g/l were still common in the early 1990s. Nevertheless, the turbid zone has been extended further inland and reaches up to 60 km from Saint-Nazaire.

In 2007, six monitoring stations have been installed in the Loire estuary distributed from Saint-Nazaire to Bellevue (62 km upstream), called the SYVEL network. Each station measures salinity, turbidity, temperature and dissolved oxygen 1 m below the surface. Although not all stations have been operational the entire period during 2007-2013, Jalón-Rojas et al. (2016) have been able to track the turbid zone in the Loire estuary in detail using this long-term and high-frequency (measurements every 10 minutes) monitoring data. The turbid zone reaches the last station (62 km from the mouth) during periods of low river discharge and flushes downstream by river floods. To be more precise, Fig 5 in Jalón-Rojas et al. (2016) shows the location of the turbid zone for low, mean and high tidal ranges as well as for low, medium and high river discharges. For low discharges (<200 m^3/s), the turbid zone is found between 25 and 40 km from the mouth. Remarkable however is the fact that the turbid zone is found more towards the sea for a larger tidal range. For medium discharges (500-850 m^3/s), the turbid zone is found between 10-25 km (and again more seaward for large tidal ranges). For high river discharges (1500-4000 m^3/s), the turbid zone is found between 0-15 km for both high and low tidal ranges. In contrast to the concentrations of suspended matter near the surface found before 2000, measurements of the SYVEL network show concentrations up to 5.5 g/l, see Figure 1.4. Model studies of Normant (2000) and Sogreah (2010) show that concentrations at the surface in the order of 1-5 g/l can be accompanied by concentrations near the bottom in the order of 10-20 g/l.

In addition to the qualitative description of the previous section, a graphical representation makes the relation between the ETM and the river discharge even more clear. In Figure 3.11 both the river discharge and the tidally averaged sediment concentrations near the surface are plotted over time at three locations with increasing distance from the mouth from top to bottom. It can be seen that around Donges (km 10) high sediment concentrations coincide with high river discharges, whereas around Cordemais and Trentemoult (km 26 and 50 respectively) high sediment concentrations are only found for low river discharge. This research aims to describe the mechanisms responsible for turning the Loire into a hyperturbid state. It seems like the landward part of the estuary has much higher concentrations than the mouth of the estuary during times of low river discharge. Given that we would like to model the development of high concentrations in the estuary from low concentrations at sea, Figure 3.11 shows that this only makes sense for low river discharge. For high discharge, the development of concentrations in the mouth area and coastal zone also needs to be modelled. This is out of the scope of this study. For this reason, we will mainly focus on river discharges around the average summer discharge of 300 m^3/s.

TURBIDITY AT SAINT-NAZAIRE

In order to set a boundary condition for the sediment concentration at the seaward boundary, we look closer at the turbidity at Saint-Nazaire. Berthois (1955b) shows that the sediment concentrations are in the order of 0.1-0.2 g/l for winter conditions, more or less uniform distributed over the depth. During summer conditions the surface concentration could reduce with a factor 10 while the concentration near the bottom remained unchanged. The observations presented by Rincé et al. (1989) show tidally averaged concentrations at the surface at Saint-Nazaire up to 0.7 g/l during periods of high discharge, and concentrations in the range 0.05 - 0.1 g/l during periods of low river discharge.From remote sensing data, Gernez et al. (2015) also found concentrations at the surface in the range 0.05 - 0.1 g/l. Both Rincé et al. (1989) and Gernez et al. (2015) show that the concentrations at the surface are significant higher during spring tides than during neap tides. Recent measurements near Donges (km 9.5) show sediment concentrations in the range 0.1-1.0 g/l near the surface during periods of low river discharge (Jalón-Rojas et al., 2016). Based on these measurements, a depth-averaged concentration of 0.1 g/l will be used as a starting point in the iFlow model throughout the 20th century.

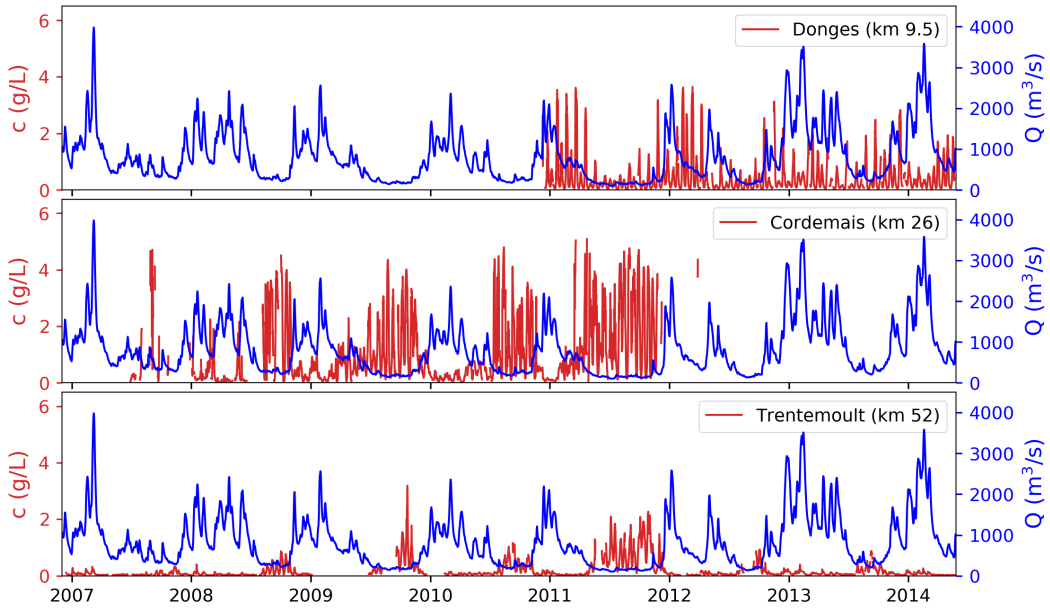

Figure 3.11: Tidally averaged turbidity near the surface at Donges (km 10), Cordemais (km 26) and Trentemoult (km 52) versus the river discharge at Montjean-sur-Loire. Source: Jalón-Rojas et al. (2016)

TURBIDITY AT LES PONTS-DE-CÉ

Where the sea acts as a source of sediments at the downstream side of the domain, the river brings sediments into the domain at the upsteam boundary (at Les Ponts-de-Cé). The concentration of suspended matter carried with the river depends on the river discharge according to Hamm and Walther (2009). For discharges below 500 m^3/s, a concentration has been found of 10 mg/l. During floods this concentration can reach up to 200 mg/l. It should be noted that the measurements they used (e.g. Berthois (1955a) and Manickam and Barbaroux (1987)) are mainly taken at Montjean-sur-Loire and not at Les Ponts-de-Cé. Although the Maine river confluences with the Loire river in between these points, this is not considered important since the Maine river hardly carries sediments.

Due to sand mining activities, some minor fluctuations in the sediment concentrations carried by the river have been observed. Nonetheless, the trapping effects of these sand minings disappeared with the ongoing regulation of the river profile (Lefort, 2010). Since we focus on relatively low river discharges, sediment input at the upstream boundary is expected to be of minor importance.

3.2.5. SALINITY

The SYVEL network also recorded salinity. Using the measurements of this dataset presented in GIP (2011b), we have been able to derive simple subtidal constant salinity fields. Though strong stratification can be observed, especially for higher discharges (GIP, 2011b), we assume the salinity to be well mixed throughout the water column. Because we are mainly interested in the summer season, this assumption seems reasonable. A summary of the mean values of salinity for the spring-neap cycle is presented in Table 3.5.

Table 3.5: Salinity values (g/l) along the Loire estuary

		Donges	Paimboeuf	Cordemais	Le Pellerin	Trentemoult	Bellevue
	km	10	15	26	39	52	62
Winter	Spring	10	5	0.2	0.2	0.2	0.1
	Neap	5	3	0.2	0.2	0.2	0.1
Summer	Spring	30	25	10	2	0.4	0.2
	Neap	20	15	5	1	0.2	0.2

Based on the data mentioned in Table 3.5, curves have been fitted describing the salinity along the estuary following a tangent-hyperbolic function which has the form:

$$s = \frac{1}{2} s_{sea} \left(1 - \tanh\left(\frac{x - x_c}{x_l}\right)\right) \tag{3.5}$$

The mean values of salinity at the measurement stations of the SYVEL network are plotted in Figure 3.12 together with the tangent-hyperbolic fits to this data. An overview of the fitted parameters is listed in Table 3.6.

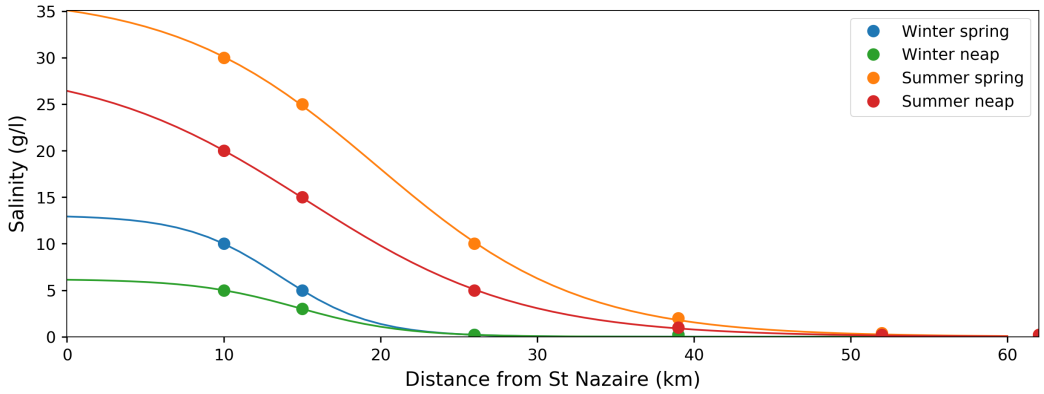

Figure 3.12: Subtidal constant salinity fields for different conditions, based on data presented in GIP (2011b)

Table 3.6: Fitted parameters of tangent-hyperbolic profiles describing the salinity along the estuary

		s_{sea}	x_c	x_l
Winter	Spring	13.1	13,560	6,021
	Neap	6.2	14,781	6,701
Summer	Spring	36.7	19,776	12,943
	Neap	29.3	15,305	13,703

3.2.6. SEDIMENT CHARACTERISTICS

The most important sediment characteristic required for the model is the settling velocity w_s. This settling velocity depends on the size and the shape of sediment flocs. Due to the process of flocculation, a large spread of floc diameters is found in the Loire estuary, leading to a large spread in the fall velocities. However, since flocculation is not explicitly accounted for within iFlow, we will use a representative value for w_s. Multiple measurements have carried out, both in situ with an Owen tube as well as in the laboratory, which related fall velocities to sediment concentrations near the bottom. All measurements as presented by Walther et al. (2012) are presented in Figure 3.13. The in situ measurements provided insight in the fall velocities in a flocculated environment, whereas the laboratory experiments were intended to capture the fall velocities in a deflocculated environment. The figure shows that the settling velocity increases for sediment concentrations < 2g/l due to flocculation and decreases for concentrations > 2 g/l due to hindered settling. Based on all different measurements, Walther et al. (2012) came up with two laws: one describing the fall velocity in a flocculated environment and one that describes the fall velocity in a deflocculated environment.

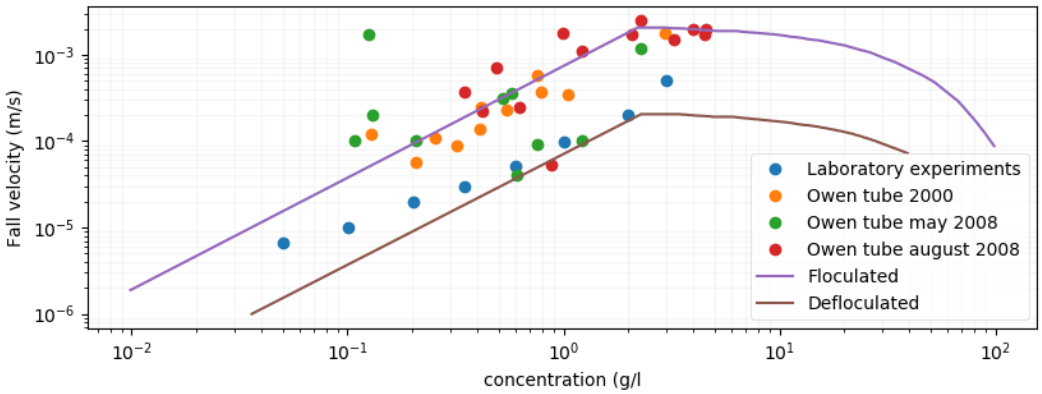

Figure 3.13: Measurements of settling velocity of the Loire, both in situ (with an Owen tube) and laboratory measurements. Two laws have been established for the settling velocity in the Loire. The field measurements resulted in the law of the fall velocity in a flocculated environment, whereas the laboratory experiments were used to establish a law that describes the fall velocity in a deflocculated environment. Source: Walther et al. (2012)

The different measurements already show quite a large spread. Since the sediment concentrations have changed drastically over the last decades, it is likely that the average settling velocities have changed as well during this period. Within iFlow, a settling velocity needs to be defined which would occur without the influence of hindered settling, called clear water settling velocity. We already noticed that hindered settling starts playing a role for near-bed sediment concentrations in the order of 1-2 g/l, and that the settling velocity around that point can be approximated by 2 mm/s. Near-bed sediment concentrations in the order of 1 g/l have been recorded throughout the 20th century, hence a clear water settling velocity of 2 mm/s seems reasonable for both historical and current scenarios.

3.3. MODEL SET-UP

To summarise this chapter we provide an overview of the default model parameters in Table 3.7. Some of the turbulence and sediment parameters were already introduced in chapter 2, but are included in the table as well.

Table 3.7: Default model parameters for the Loire in the current state

	Parameter		Spring	Neap
Hydrodynamics	A^0	M_2 water level amplitude at x=0	2.30 m	1.28 m
	A^1	M_4 water level amplitude at x=0	0.24 m	0.20 m
	ϕ^0	M_2 water level phase at x=0	0	0
	ϕ^1	M_4 water level phase at x=0	-148 deg	-155 deg
	Q	River discharge	<300 m^3/s	
Salinity	s_{sea}	Seaward salinity	36.7 g/l	29.3 g/l
	x_c	Translation	19,776 m	12,943 m
	x_l	Intrusion length scale	15,305 m	13,703 m
Sediment	c_{sea}	Depth-averaged sub-tidal concentration at x=0	0.1 g/l	
	K_h	Horizontal eddy diffusivity	100	
	M	Erosion parameter	0.01 s/m	
	$w_{s,0}$	Clear water settling velocity	0.002 m/s	
	c_{gel}	Gelling concentration	100 g/l	
Turbulence	Rf_{max}	Maximum flux Richardson number to avoid too large drag reduction	2.	
	$u_{z,min}$	Velocity gradient for background turbulence production	0.03 m/s	

4

RESULTS AND SENSITIVITY

4.1. MODEL CALIBRATION

Based on the dominant flow processes, the Loire estuary can be subdivided into two sections: a tide- and a river dominated section. Following Hamm and Walther (2009), a spatially varying bottom roughness is used to match the modelled hydrodynamics to the observed water level data (presented in chapter 3) in both of these sections. The parameter used in iFlow to describe the bottom roughness is the dimensionless roughness parameter z_0^*. By calibrating this dimensionless roughness parameter, first for the river dominated part and then for the tide dominated section, an optimal fit can be found to the data. This results in a roughness profile along the estuary as depicted in Figure 4.1, in which $z_{0,1}^*$ refers to the dimensionless roughness parameter for the tide dominated part and $z_{0,2}^*$ for the river dominated part. The model calibration will be based on the current geometry of the estuary, considering an average neap tide and a low river discharge (=250 m^3/s) as the boundary conditions. An explanation why neap tidal conditions are used for the calibration will follow in a later section.

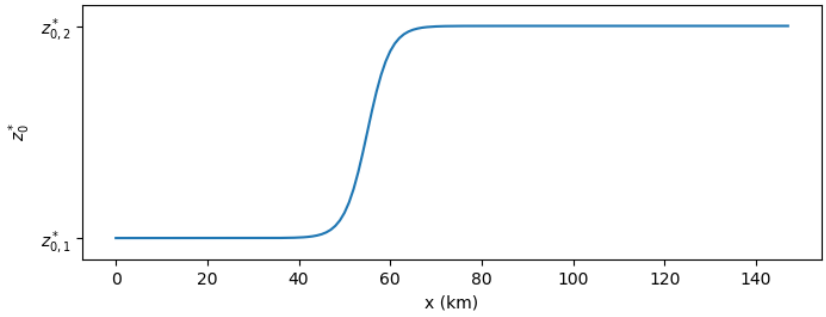

Figure 4.1: Tangent-hyperbolic profile for the roughness parameter z_0^*

4.1.1. HYDRODYNAMICS

RIVER DOMINATED PART

For the river dominated part, water level data are available for various discharges. According to Hamm and Walther (2009), roughness values highly depend on the river discharge. Since this research focusses on low river discharges, the model calibration will only be done for a low river discharge. The subtidal water level in iFlow consist of two parts: a reference level and a subtidal set-up. The reference level, best described as a quick estimate of the mean surface level, consists of the mean sea level (at x=0) plus a backwater curve due to the river discharge. The subtidal set-up, ζ_{M0}, consists of contributions due to nonlinearities. In order to model the correct depths in the river dominated part, the roughness parameter is adjusted such that the reference level fits well to the measurements, as depicted in Figure 4.2. The subtidal set-up due to nonlinearities is assumed to be small and is therefore ignored in the calibration. This results in a dimensionless roughness parameter $z_{0,2}^*$ of 0.11.

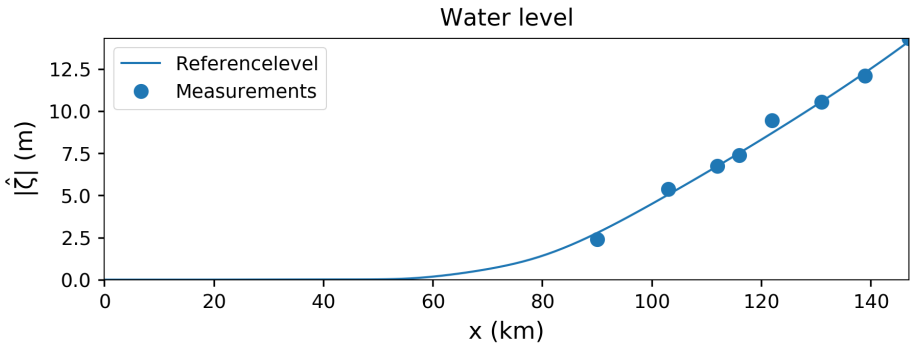

4

Figure 4.2: Best fit of the reference level (solid line) to measurements (dots), found for a roughness value z_0^* of 0.11

TIDE DOMINATED PART

The calibration for the tide dominated part of the estuary is based on the observed M_2 water level amplitudes and phases as presented in Table 3.2. In a similar way as is done for the river dominated part of the estuary, a calibration is performed for neap tidal conditions. The best fit of the model to the data is found for a dimensionless roughness parameter $z_{0,1}^*$ of 0.01. The resulting water level amplitudes and phases of the different tidal constituents are plotted in Figure 4.3. Both for the tidal amplitudes and the tidal phases the observed patterns are reproduced well. However, it should be noted that the M_4 tidal amplitude is overestimated locally up to a factor 1.5.

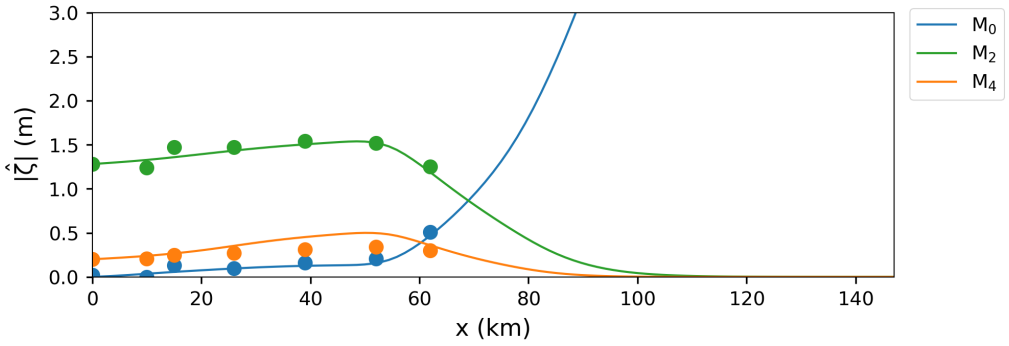

(a) Water level amplitude

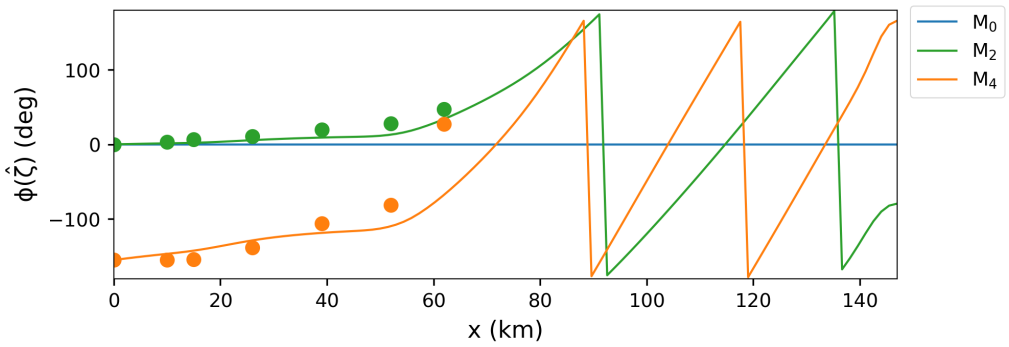

(b) Water level phase

Figure 4.3: Modelled (solid lines) and observed (dots) water level amplitude and phase of the subtidal M_0 (blue), M_2 tide (green) and M_4 tide (orange) for neap tide conditions.

4.1.2. SEDIMENT DYNAMICS

The model parameters $w_{s,0}$ (clear water settling velocity), M (erosion parameter) and c_{cea} (subtidal depth averaged sediment concentration at x=0) are important parameters regarding sediment dynamics within iFlow. Significant variability has been reported in observations for all of these input parameters. Therefore, instead of calibrating the model using (one of) these parameters, they are set to default values within the range of the observations (see Table 3.7). The effects of variations of the parameter values on the model will be investigated by sensitivity analyses in the upcoming sections. Here it is verified whether the proposed values yield reasonable results for the sediment dynamics; modelled tidally averaged sediment concentrations at the surface are compared with the observed sediment concentrations collected with the SYVEL network. It is important to note that for the type of model used in this research, we more focus on a qualitative reproduction than on exact numbers. With other words, the sediment dynamics are captured well if the ETM occurs around the expected location with sediment concentrations in the same order as the observed concentrations.

4.2. ANALYSIS OF NEAP TIDE

The previous section showed that iFlow is able to reasonably reproduce the hydrodynamics. This section provides a closer look at the sediment dynamics and the physical processes important in the Loire estuary. First, modelled sediment concentrations are presented in subsection 4.2.1. Next, considering the underlying physical processes, two different aspects will be discussed. In the first place, sediments should be transported towards and/or be contained within the estuary. Locations at which sediments tend to accumulate are called trapping zones (subsection 4.2.2). Secondly, to obtain high suspended sediment concentrations in those trapping zones, local resuspension should be sufficiently high to bring or keep the sediments in suspension (subsection 4.2.3). Both aspects will be treated first for a neap tide scenario. Finally, the role of sediment-induced damping of turbulence on both aspects is investigated in subsection 4.2.4.

4.2.1. SEDIMENT CONCENTRATIONS

The performance of the model regarding sediment concentrations is evaluated in Figure 4.4. Figure 4.4a clearly shows that the tidally averaged modelled sediment concentrations near the surface are in the same order as the observed concentrations, especially when considering median values. The analysis of Jalón-Rojas et al. (2016) reported that the ETM was found around 40 km from Saint-Nazaire during neap tide conditions, which is also the case in the model. The sediment distribution over depth as presented in Figure 4.4b shows concentrations near the bottom in the order of 10 g/l. Concentrations like this seem reasonable, since Jalón-Rojas et al. (2016) report that concentrations near the bottom may be up to 8 times higher than at the surface. Interesting to note is that the location of the ETM at the surface is not the same as the ETM near the bottom. For the presented case, we can state that iFlow was able to reproduce the observed hydrodynamic and sediment dynamics.

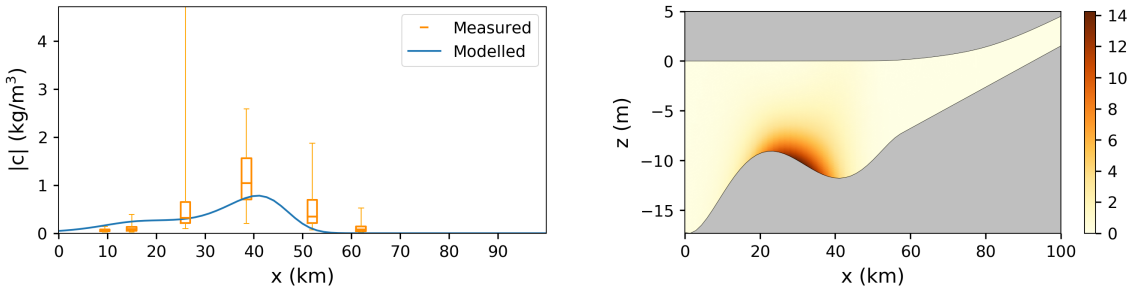

(a) Sediment concentration (g/l) at the surface

(b) Sediment concentration (g/l) over depth

Figure 4.4: Suspended sediment concentrations for neap tide obtained with the dimensionless roughness parameters that followed from model calibration. Figure 4.4a compares measurements (in orange) with modelled values (in blue), in which the measurements are presented as boxplots (containing minimum,q1,median,q3 and maximum).

4.2.2. SEDIMENT TRAPPING

To investigate which processes are responsible for the sediment trapping, individual contributions to the sediment transport need to be known. As presented in the chapter about iFlow (chapter 2), the total suspended sediment transport is defined as the cross-section integrated sum of the advective and diffusive transport. Using the perturbation method, we have been able to develop expressions for sediment transport due to individual processes. Since the suspended sediment transport directly depends on the sediment concentrations, which we found to have changed significantly over time, a comparison of suspended sediment transport between different years will not provide much insight. Instead of looking at the sediment transports, we will therefore look at the sediment transport capacity (Dijkstra et al., 2019c). The transport capacity is the sediment transport that would occur if there was plenty of sediment on the bed everywhere along the estuary. As a result, the transport capacity is mainly determined by the hydrodynamics and sediment parameters, not the actual sediment concentrations. Moreover, when the transport capacity equals zero, the sediment transport equals zero as well. This means that we either have a location where the sediment transport diverges (zero up-crossing), or a location where the sediment transport converges (zero down-crossing). The latter is called a trapping zone.

A selection of the five most important physical mechanisms contributing to the transport capacity in the neap tidal case (Table 3.7) has been plotted in Figure 4.5. The total transport capacity (black dashed line) shows a trapping zone (downward zero-crossing) around 35 km from the mouth. In Figure 4.4b we can see that this trapping zone is in accordance with the depth-averaged ETM. The physical meaning of the individual contributions to the transport capacity and its importance in the Loire estuary is discussed below:

- Sediment transport due to the *baroclinic* contribution is caused by horizontal density gradients following from a prescribed salinity gradient. These horizontal gradients result in gravitational circulation, which is characterised by a landward directed flow near the bottom and a seaward directed flow near the surface. With a non-uniform sediment distribution over the water column, i.e. higher concentrations near the bottom than at the surface, this results in a net import of sediments. The blue curve in Figure 4.5 shows that this is an important mechanism in the Loire, causing sediment import in the first 50 km.
- The contribution to the transport capacity due to the *external* M_4 *tide* reveals another importing mechanism in the Loire estuary. The phase difference between the M_2 and M_4 tide at that propagates into the estuary from the mouth results in tidal asymmetry. The asymmetry of the tidal wave results in different velocities during ebb and flood, which in turn cause a net sediment transport. In the Loire estuary, this asymmetry causes sediment import in the first approximately 65 km, whereas it is an exporting mechanism between km 65-90.
- The *river* contribution to the transport capacity contains two physical mechanisms. At first, we have river-induced flushing which can be described by the river flow (always seaward directed) pushing out sediments that are resuspended by the tidal motion (mainly the $M2$ tidal motion). Secondly, the river flow enhances ebb flows and reduces flood flows resulting in tidal asymmetry, resulting in enhanced sediment export (or reduced import). The green curve in Figure 4.5 shows that the river contribution is the most important exporting mechanism in the Loire estuary.
- The *river-river* contribution is only present after 60 km from the mouth. This term describes the transport capacity of river-induced flushing of sediments that are resuspended by the river flow itself. Since most of the sediments are present in the first 60 km of the Loire estuary, this contribution will not have a major contribution to suspended sediment transports.
- Last important mechanism in the Loire estuary is the *sediment advection* contribution, which represents the transport due to spatial settling lag. To explain this, consider a situation where the tidal velocity amplitude decreases in landward direction. During flood, a sediment particle is carried some distance landward and settles. When during ebb the particle is re-entrained, the velocity of the fluid particle carrying the sediment is lower than during flood, hence for equal settling velocities and depth the particle settles landward from its starting position (Pritchard and Hogg, 2003). In other words, spatially varying velocities result in net sediment transport towards locations with minimum tidal velocity amplitude. The red curve in Figure 4.5 shows that the contribution of sediment advection is characterised by transport roughly toward the trapping zone.

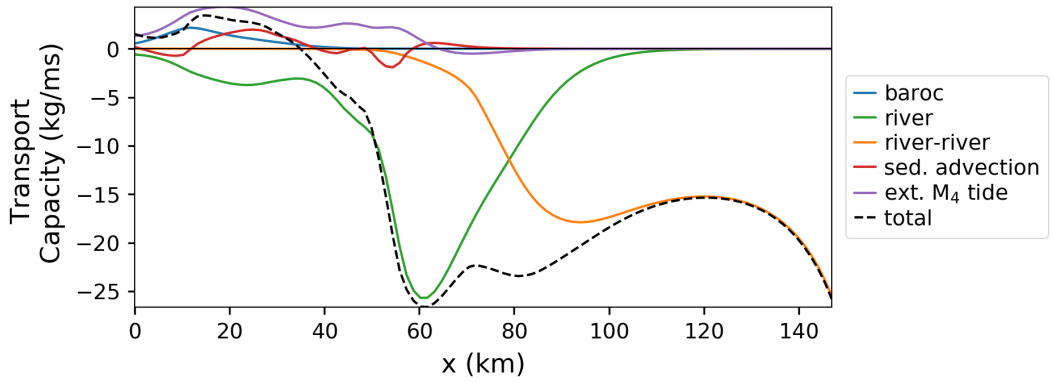

Figure 4.5: Overview of the five most important (coloured lines) contributions to the depth integrated sediment transport capacity per meter width for neap tide conditions and a river discharge of 250 m^3/s. The downward sloping zero-crossing of the total transport capacity (black dashed line) indicates a trapping zone.

4.2.3. LOCAL RESUSPENSION

Another mechanism governing the sediment dynamics within an estuary is the potential local resuspension, i.e. the potency of the flow to bring or keep sediments in suspension. Whether maximum sediment concentrations are actually bounded due to limited resuspension can be derived from the erodibility f, which is a measure of the amount of sediment available for resuspension. Either we have an erodibility $f < 1$, indicating that availability of sediment is restricting the sediment concentrations, also referred to as supply limited, or $f = 1$, indicating that local resuspension is limiting, which is referred to as erosion limited.

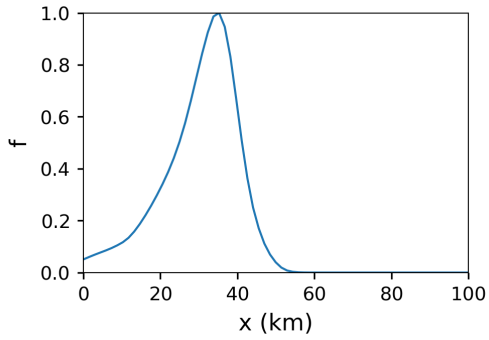

(a) Erodibility f, indicating the amount of sediment available on the bottom for erosion. If f equals 1, easily erodible sediment is available at the bottom so maximum concentrations are erosion limited, whereas all values smaller than 1 indicate that sediment supply is limiting.

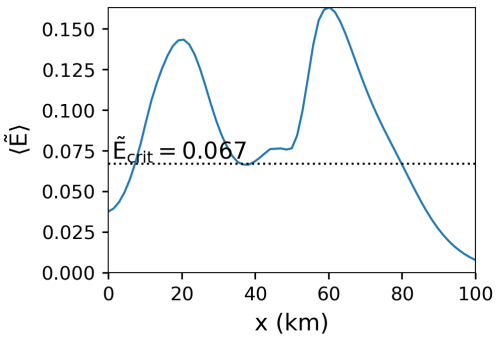

(b) Dimensionless erosion parameter $\tilde{E}$, which indicates whether maximum sediment concentrations can be limited by local resuspension. If $\tilde{E}$ exceeds the treshhold value of 0.067, this is not the case.

Figure 4.6: Erodibility f and dimensionless erosion parameter $\tilde{E}$ along the estuary for neap tidal conditions and an average summer discharge of 250 m^3/s.

Figure 4.6a presents the erodibility along the estuary for the neap tidal case. In the trapping zone, which we found to be around km 35, $f = 1$. With other words, we expect the maximum concentrations at that very point to be bounded by local resuspension. At locations where $f = 1$, sediments are deposited on the bed forming a growing bottom pool. This bottom pool acts as a sediment sink and therefore restricts the amount of sediments available in the rest of the estuary, which can be recognized in the figure since $f < 1$ indicates supply limited state.

Another way to look at local resuspension is by investigating the dimensionless erosion parameter $\tilde{E}$ (see Equation 2.71). Dijkstra et al. (2018) derived that resuspension cannot be restricting the sediment concentrations if $\tilde{E} > 0.067$ within the context of the iFlow model. Figure 4.6b shows that sediment concentrations in the ETM are indeed limited by local resuspension since $\langle \tilde{E} \rangle$ drops below $\tilde{E}_{crit}$ near km 35. However, this is only just, so that ta small change of parameter values could lead to supply limited conditions.

4.2.4. ROLE OF SEDIMENT-INDUCED TURBULENCE DAMPING

As introduced in chapter 2, vertical stratification due to high sediment concentrations has a strong influence on the turbulent motions which influences the hydrodynamics and sediment dynamics. These indirect effects of sediment-induced turbulence damping are hard to capture in a specific contribution to the transport capacity, because it affects all of the sediment transport contributions. By turning off the sediment-induced damping and comparing the contributions to the transport capacity with and without damping, insight is gained in the strength of this effect. This can be done by setting the damping functions Equation 2.15, Equation 2.16 and Equation 2.20 equal to 1. The occurring suspended sediment concentrations along the estuary for the cases with and without sediment-induced turbulence damping are depicted in Figure 4.7a and Figure 4.7b respectively. We find that the role of sediment-induced damping is crucial in obtaining high sediment concentrations around km 35. Without the damping of turbulence, sediment concentrations up to 0.2 g/l are found in the first 25 km of the estuary distributed fairly uniform over the water column. When sediment-induced turbulence damping is taken into account, near-bed concentrations of approximately 14 g/l are found in the ETM around km 35. In addition to that, the sediment distribution over the water column shows a strong stratification.

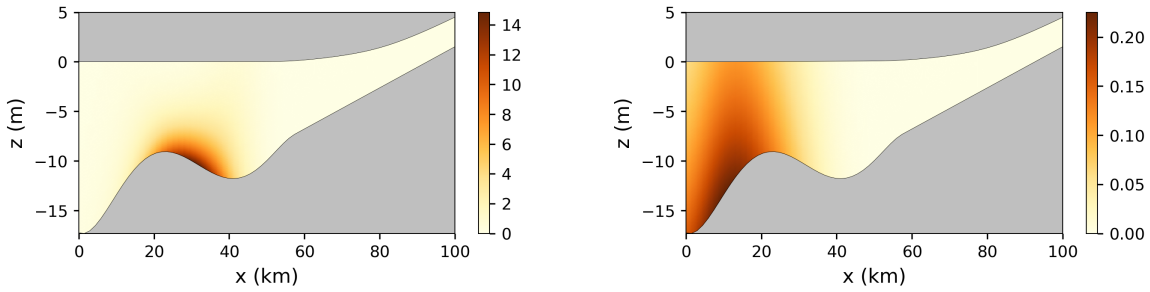

(a) With sediment-induced turbulence damping

(b) Without sediment-induced turbulence damping

Figure 4.7: Suspended sediment concentrations (g/l) for neap tidal conditions and an average summer discharge of 250 m^3/s, obtained with (a) and without (b) sediment-induced turbulence damping.

In Figure 4.8, the comparison of contributions to the total transport capacity is provided for neap tidal conditions. The solid lines represent the contributions including sediment-induced damping and the dashed lines represent the contributions without sediment-induced damping of turbulence. We see that especially the import of sediments increases due to turbulence damping, while the export remains roughly the same. The contribution due to the external M_4-tide has been amplified by over a factor 2 and the baroclinic transport has increased even more. The exporting contribution due to the river even got slightly damped in the trapping zone near km 35 in the case with damping. Also the contribution due to sediment advection shows

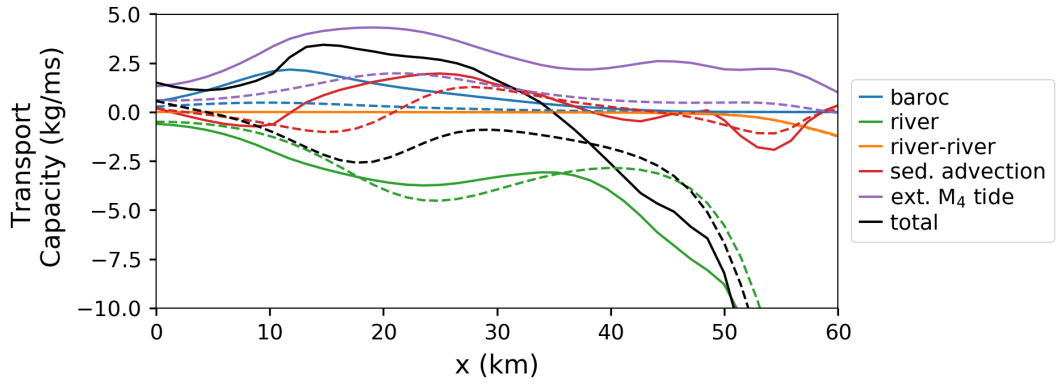

Figure 4.8: A comparison of the various contributions to the total transport capacity (in black) for neap tidal conditions with(solid lines) and without (dashed lines) sediment-induced turbulence damping.

significant variations with and without sediment-induced damping, mostly favouring import. This indicates that the flow velocities are affected as well. These changes in flow velocities can be explained using the partial slip parameter s_f, which is a measure of the friction felt by the water motion, and the eddy viscosity A_v. In Figure 4.9, the partial slip parameter is presented for the cases with and without sediment-induced turbulence damping. It can be clearly seen that this damping significantly reduces the bed friction. Like s_f, the eddy viscosity is reduced between 0 and 50 km when accounting for sediment-induced turbulence damping. A reduction in bed friction results in enhanced sediment import by amplification of the external M_4-tidal contribution, which in combination with a reduced eddy viscosity (reduced turbulent motions, and hence enhanced sediment stratification) even causes further reduction of the bed friction. In other words, when sediment-induced turbulence damping starts playing a role, a positive feedback loop causes the sediment import to increase. This partly confirms the hypothesis of Winterwerp and Wang (2013) (see Figure 1.6).

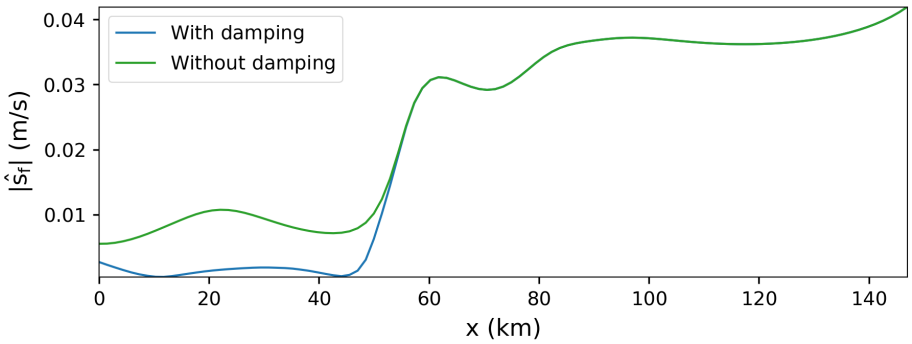

Figure 4.9: Partial slip parameters along the estuary in (m/s). S_f is a measure for the friction felt by the water motion (flow). Near-bed stratification clearly reduces the bed friction, and therefore flow velocities are affected as well.

4.3. ANALYSIS OF SPRING TIDE

Since the tidal forcing on the Loire estuary varies over a bi-weekly spring-neap cycle, we are also interested in the performance of the model for spring tidal conditions. This section elaborates on the results obtained for spring tidal conditions, especially focussing on the different contributions to the total transport capacity.

In comparison with neap tidal conditions, the model forcing for spring tidal conditions exists of a larger semi-diurnal and quarter-diurnal amplitude at the seaward boundary. Furthermore, a more pronounced salt intrusion is observed during spring conditions, and therefore a different subtidal constant salinity field has been prescribed (see Table 3.7 for parameter settings). All other input parameters are kept constant, including the dimensionless roughness parameters that followed from the calibration for neap tidal conditions. The re-

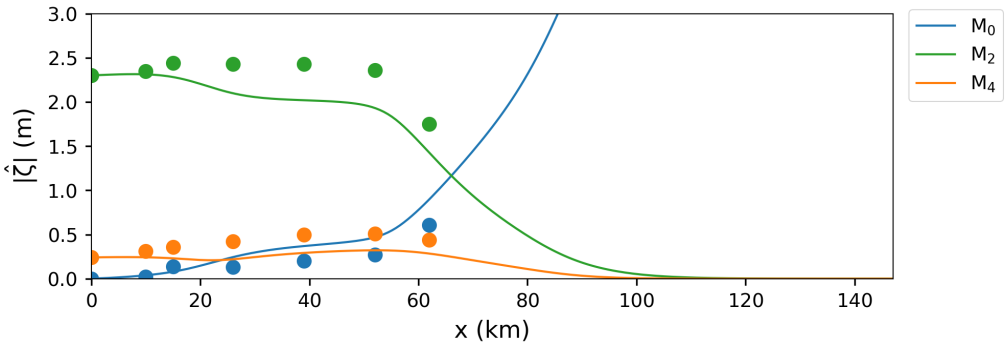

(a) Water level amplitude

Figure 4.10: Modelled (solid lines) and observed (dots) water level amplitude and phase of the subtidal M_0 (blue), M_2 tide (green) and M_4 tide (orange) for spring tide conditions.

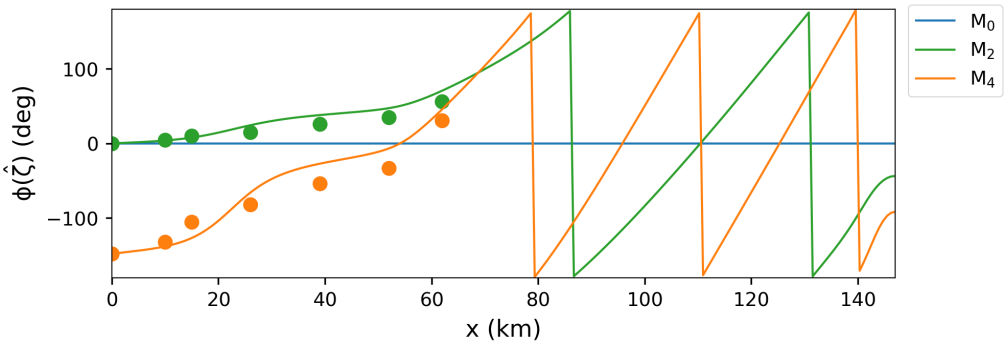

(b) Water level phase

Figure 4.10: Modelled (solid lines) and observed (dots) water level amplitude and phase of the subtidal M_0 (blue), M_2 tide (green) and M_4 tide (orange) for spring tide conditions.

sulting water level amplitudes and phases are plotted against measurements in Figure 4.10. The M_2 and M_4 water level amplitudes are significantly underestimated between 20 and 60 km from the mouth. The general pattern of water level phases is reproduced quite well, although we could argue that both the M_2 and the M_4 tidal phase increase slightly too fast, indicating too slow wave propagation.

Next to an underestimation of the tidal water level amplitudes, modelled suspended sediment concentrations are underestimated as well. Figure 4.11a presents a comparison of modelled and observed suspended sediment concentrations during spring tide at the surface. The modelled suspended sediment concentrations along the estuary are plotted in Figure 4.11b. Both figures clearly show that the sediment concentrations are underestimated by approximately a factor 100.

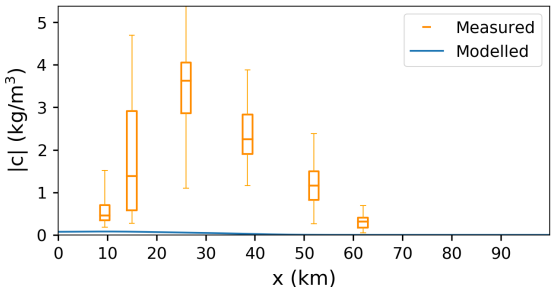

(a) Sediment concentration (g/l) at the surface

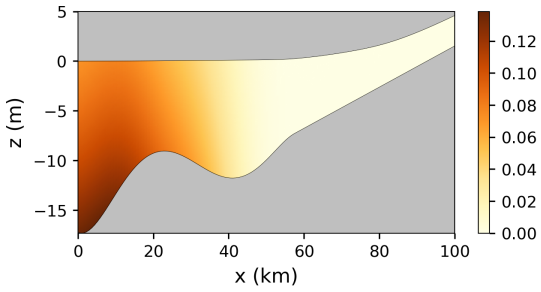

(b) Sediment concentration (g/l) over depth

Figure 4.11: Suspended sediment concentrations for spring tide obtained with the dimensionless roughness parameters that followed from model calibration for neap tide. Figure 4.11a compares measurements (in orange) with modelled values (in blue), in which the measurements are presented as boxplots containing (minimum,q1,median,q3 and maximum)

In the previous section we saw that suspended sediment concentrations can be bounded due to either a lack of supply or a limited resuspension. Using the erodibility parameter f, we can deduce which of the two is the case for spring tidal conditions. Figure 4.12a clearly shows that $f \ll 1$ along the entire estuary, indicating a supply limited state. Additionally, Figure 4.12b shows that the dimensionless erosion parameter exceeds the threshold of 0.067 confirming that local resuspension during spring tidal conditions is capable of producing high sediment concentrations. Hence, sediment trapping is the limiting factor for high sediment concentrations to occur, suggesting we should look at the contributions to the transport capacity.

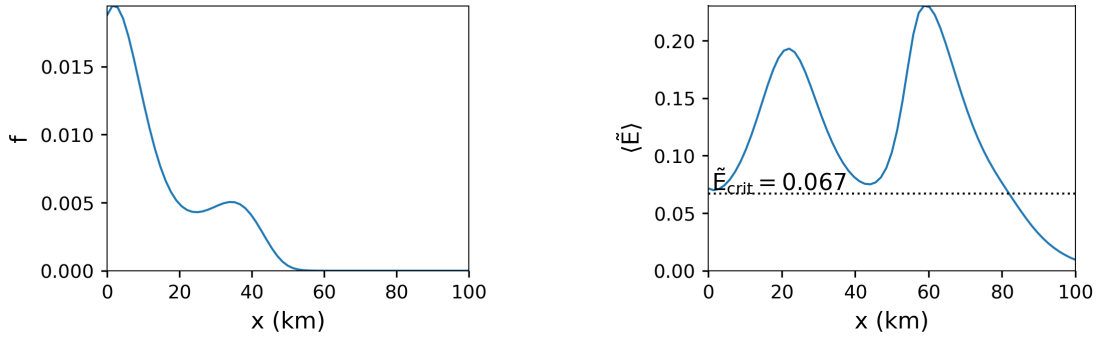

(a) Erodibility f, indicating the amount of sediment available on the bottom for erosion.

(b) Dimensionless erosion parameter $\tilde{E}$, which indicates whether maximum sediment concentrations are limited by local resuspension.

Figure 4.12: Erodibility f and dimensionless erosion parameter $\tilde{E}$ along the estuary for spring tidal conditions and an average summer discharge of 250 m^3/s. With the erodibility $f < 1$ along the entire estuary, and $\tilde{E} > 0.067$, suspended sediment concentrations are found to be supply limited.

To be able to compare the transport capacity contributions for spring and neap tide, we plotted the same 5 contributions for spring tidal conditions in Figure 4.13 as we did for neap tidal conditions in Figure 4.5. The total transport capacity shows trapping zones around km 5 and 35 which corresponds to the locations where the graph of f shows a maximum. Unlike for neap tidal conditions, the presence of the trapping zone around km 35 does not coincide with hyperturbid conditions regarding spring tidal conditions. The question that arises is which processes are responsible for the large differences between the results for spring and neap tide conditions? An analysis of the differences in the individual contributions to the total transport capacity for spring and neap tidal conditions is presented below:

- Considering the transport capacity due to the *baroclinic* contribution, its contribution during spring tidal conditions is both absolutely and relatively much smaller than during neap tidal conditions. At first instance this might be surprising, since we stated earlier that the baroclinic contribution scales linearly with the M_2 tidal amplitude (see Table 2.3). Nevertheless, the transport capacity does take into account the distribution of the sediments over the water column, which is much more stratified during neap tide due to the high sediment concentrations. Combining this stratification due to high sediment concentrations and the gravitational circulation explains the significant larger contribution during neap tidal conditions.
- The transport capacity due to the *river* contribution scales linearly with the M_2 tidal amplitude. As this amplitude increased by almost a factor 2, we expected this contribution to increase with a factor 2 as well. This expectation is confirmed by the green curve in Figure 4.13, indicating that the river induced export is almost twice as large during spring than than during neap tide.

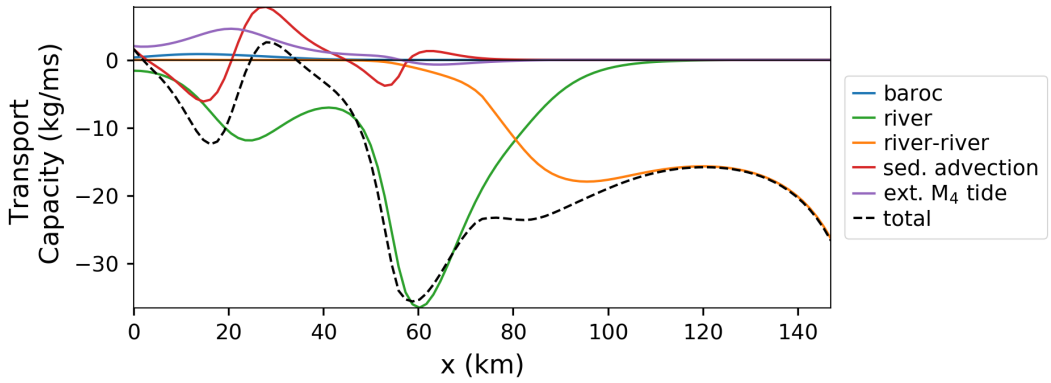

Figure 4.13: Overview of the five most important (coloured lines) contributions to the depth integrated sediment transport capacity per meter width for spring tide conditions and a river discharge of 250 m^3/s. The downward sloping zero-crossing of the total transport capacity (black dashed line) indicates a trapping zone.

- A change in tidal forcing should not directly affect the *river-river* contribution to the transport capacity. Comparing its magnitude during spring and neap tide shows that this is indeed the case.
- According to Table 2.3, we expect the contribution due to *sediment advection* to increase with $|M_2|^3$. This expectation is roughly confirmed by the red curve in Figure 4.13, which shows that sediment advection becomes equally important as the river considering sediment export in the first 20 km, and even more important than the external M_4-tide considering sediment import from km 20 onwards.
- The contribution of the *external* M_4 *tide* to the total transport capacity depends on the amplitudes of both the semidiurnal and the quarterdiurnal component, as well as their phase difference. The phase difference does not differ much between spring and neap tidal conditions, whereas both amplitudes increase during spring tide. However, as was the case for the contribution due to baroclinic transport, we do not observe an increase in transport capacity due to the external M_4-tide for spring tide conditions. A more detailed look in the role of the sediment concentrations on this behaviour will be presented in the next section.

4.3.1. COMPARISON SPRING AND NEAP

The role of sediment-induced turbulence damping made it hard to compare the contributions due to baroclinic transport and the external M_4-tide in the previous section. By again turning off the damping, a more clear comparison is possible of which the results are shown in Figure 4.14. Without the damping of turbulence, it is clearly visible that the proportionality of the specific contributions to the tidal forcing as derived in chapter 2 do hold this time. The total transport capacities show an ETM around km 5 for neap tide and two ETMs around km 2.5 and 35 for spring tide.

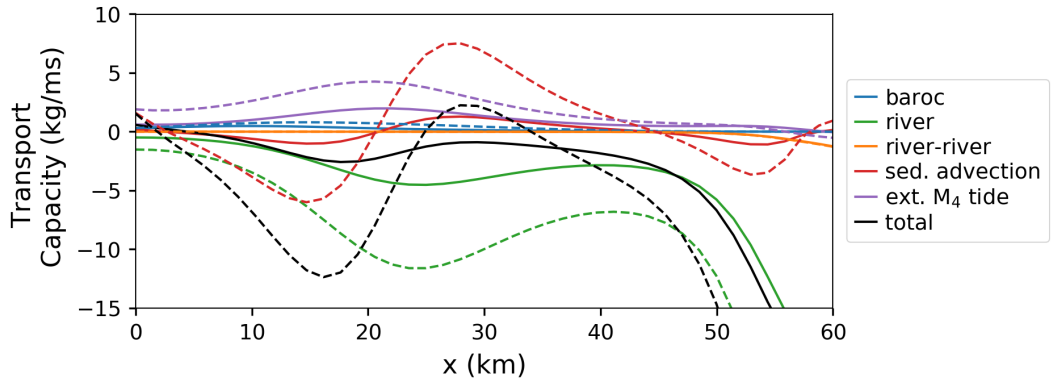

Figure 4.14: A comparison of the various contributions to the total transport capacity (in black) without the influence of sediment-induced turbulence damping between neap- (solid lines) and spring tidal conditions (dashed lines).

The most striking difference between spring and neap tide along the first 30 km of the estuary is the much stronger tidally averaged export during spring tidal conditions. Though iFlow does not include a certain timescale (equilibrium states ar calculated instead), the iterative way in which the sediment-induced turbulence damping is taken into account can be used to come up with a possible explanation how the estuary becomes hyperturbid during neap tidal conditions when turning turbulence damping back on. Low concentrations of sediment ($\mathcal{O}(10^{-1} g/l)$) already have minor influence on the eddy viscosity, eddy diffusivity and bed friction. These effects can be found both during neap and spring tide. The reduced forcing during neap tide however results in lower bed friction (because of the lower velocities) and less turbulence (so more vertical stratification) than the spring tidal forcing. Each loop in the iteration, sediment concentrations and turbulence are calculated. It is easy to imagine that once the bed friction is reduced, the import of sediments in the first five kilometres is enhanced, resulting in higher sediment concentrations and a landward shift of the ETM. In iFlow, this feedback loop continues until equilibrium state has been reached. Apparently, during neap tide the conditions are such that this process continues until sediments can be brought 35 km inland, whereas the strong exporting capacity during spring tide does not allow for tidally averaged sediment import into the estuary. Therefore, the sediment-induced turbulence damping remains low for spring tidal conditions. Nevertheless, based on the findings for neap tidal conditions, we could argue that if we can increase the sediment import during spring tidal conditions there might be a tipping point at which sediment-induced

turbulence damping becomes large enough, and high sediment concentrations could be found. In the upcoming sections, this hypothesis is tested with multiple sensitivity studies.

4.4. SENSITIVITY STUDIES

The parameters M, c_{sea} and $w_{s,0}$ are important parameters regarding sediment dynamics, but may display large variability. Also the river discharge, playing an important role in exporting sediment from the estuary, shows large variability over the year. By varying the values of these parameters in sensitivity studies, we try to explore the robustness of the results so far and verify the hypotheses that hyperturbid conditions during spring tide may occur.

4.4.1. SENSITIVITY TO RIVER DISCHARGE

To gain insight in the sensitivity of the model results to the river discharge, Q_1 has been varied between 50 m^3/s (close to the minimum discharge ever recorded) and 450 m^3/s (high summer discharge). For each experiment, a constant but different river discharge is defined keeping all other parameters constant. The suspended sediment concentrations near the bottom and near the surface along the estuary resulting from all experiments considering neap tide are plotted in Figure 4.15a and Figure 4.15b, respectively. Both near the bottom and near the surface, an increasing discharge results in a seaward shift of the ETM (represented by the grey line). This holds for river discharges up to approximately 300 m^3/s, after which a sudden decrease in sediment concentrations along the estuary can be observed.

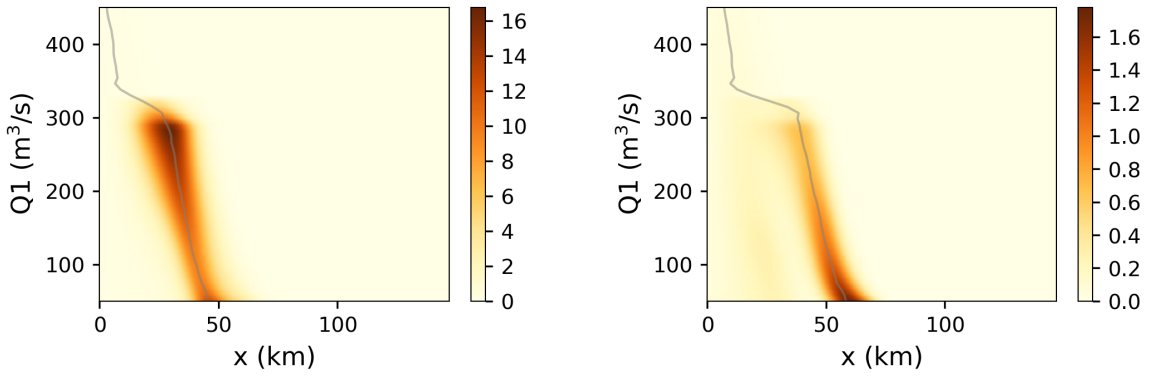

(a) Subtidal near-bed concentration in (kg/m^3)

(b) Subtidal surface concentration in (kg/m^3)

Figure 4.15: Subtidal sediment concentrations in (kg/m^3) for neap tidal conditions near the bed (a) and at the surface (b). The ETM has been indicated by the grey line.

This sudden drop in suspended sediment concentrations asks for some more detailed investigation. Figure 4.16 shows the same results of the maximum near-bed concentration but now by both starting from a low discharge and increasing it and starting from a high discharge and decreasing it. Coming from the hyperturbid state, so starting with low river discharges, sediment concentrations larger than 5 g/l are found up to discharges of 320 m^3/s, whereas such concentrations are only found for discharges below 260 m^3/s when starting in the low concentration state (high river discharge). We thus see hysteresis, indicating that the state of a system depends on its history. As a consequence of the hysteresis, two equilibrium states exist in a certain range of discharges. Considering a discharge of 274 m^3/s, it can be clearly seen in Figure 4.16 that two equilibrium states exist. A comparison of the various contributions to the transport capacity for the two different states has been presented in Figure 4.17. The contributions leading to the low concentrations look much like the concentrations without turbulence damping from Figure 4.8, while the contributions leading to the high concentration are highly similar to those with turbulence damping from Figure 4.8. The contributions due to the external M_4-tide and the baroclinic transport are significantly amplified over the first 40-50 km, whereas a slight dampening of the exporting river contribution can be observed. Based on these findings, we can argue that although the estuary is in supply limited state during spring tide, the initial state of the sediment concentrations in the estuary might be important as well.

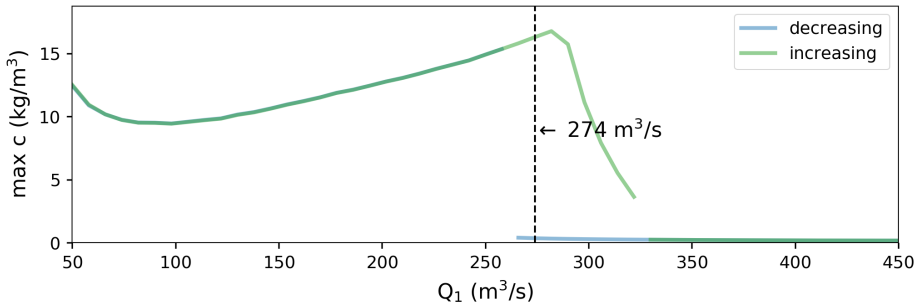

Figure 4.16: Maximum sediment concentrations near the bottom that can be found in the estuary for increasing (green) and decreasing (blue) discharges. The transition from low to high concentrations and vice verse are found to happen for different discharges, so for in a certain range of discharges two equilibrium states can be found (e.g. at Q1 = 274 m^3/s.)

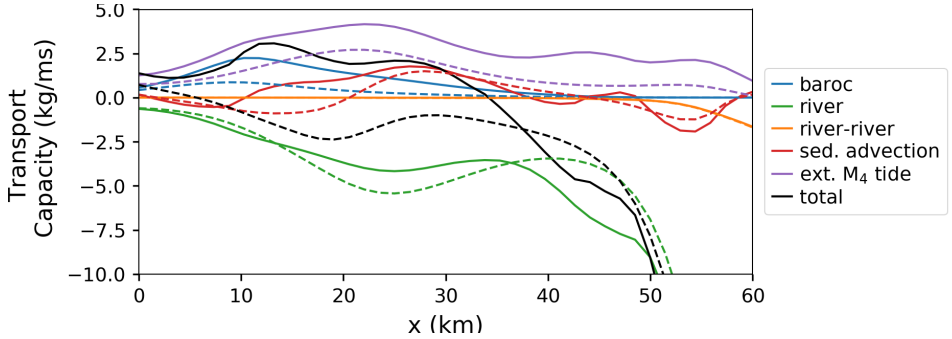

Figure 4.17: Comparison of the various contributions to the total transport capacity considering neap tidal conditions and a discharge of 274 m^3/s for increasing discharge (solid line) and decreasing discharge (dashed line).

A similar sensitivity study has been performed for spring tidal conditions of which the results are presented in Figure 4.18. We already found that for a discharge of 250 m^3/s, sediment concentrations were in the order of 0.1 g/l with its maximum around 2.5 km from the mouth. For discharges larger than 250 m^3/s, the ETM got pushed towards the sea even more. For discharges below 150 m^3/s, a significant landward shift of the ETM can be noticed. Nevertheless, only gradual increase of sediment concentrations (still in the order of 0.1 g/l) were found for further decreasing river discharges. Also for spring tidal conditions, simulations are executed in reverse order, but equal results were found. This strokes with our expectations, since hysteresis is only expected to occur once sediment-induced turbulence damping becomes important.

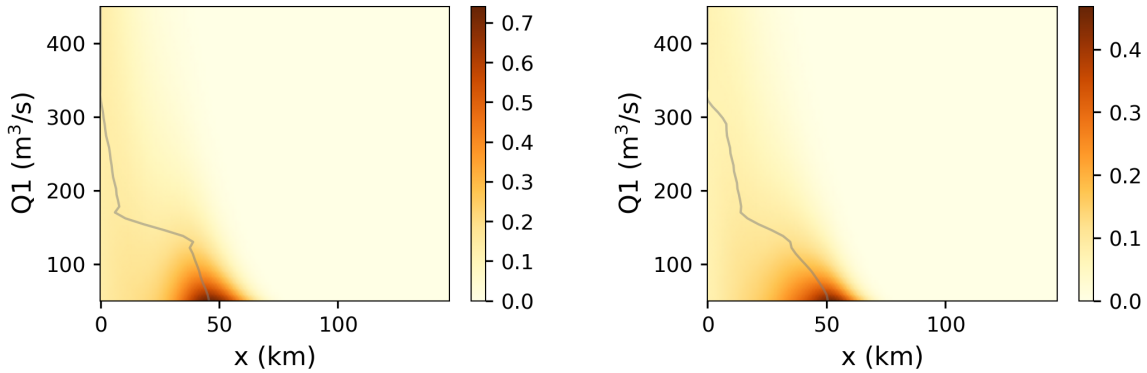

(a) Subtidal near-bed concentration in (kg/m^3)

(b) Subtidal surface concentration in (kg/m^3)

Figure 4.18: Subtidal sediment concentrations in (kg/m^3) for spring tidal conditions near the bed (a) and at the surface (b). The ETM has been indicated by the grey line.

4.4.2. SENSITIVTY TO THE DEPTH AVERAGED SEDIMENT CONCENTRATION AT X=0

Another input parameter that shows quite some spread over the year is the depth averaged sediment concentration at Saint-Nazaire (x=0). The sensitivity of the model results to the sediment concentration at the seaward boundary is investigated by varying the concentration between 0.01 kg/m^3 and 0.60 kg/m^3. The resulting near-bed concentrations along the estuary are plotted for neap and spring tide in Figure 4.19a and Figure 4.19b, respectively. While increasing the sediment concentrations at the seaward boundary from 0.01 g/l onwards, both cases show a sudden jump in sediment concentrations along the estuary at some point. However, this transition from low to high concentrations is found for a seaward sediment concentration of approximately 0.1 g/l for neap tidal conditions and only at 0.5 g/l for spring tidal conditions.

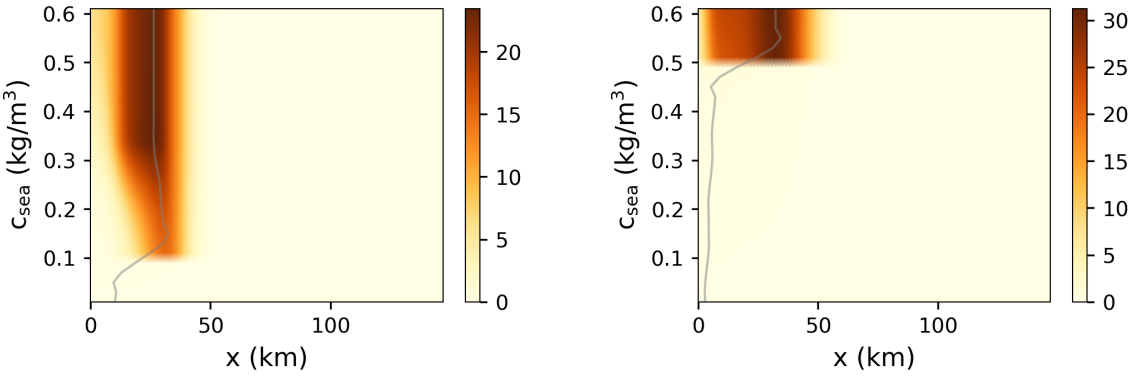

(a) Neap tide

(b) Spring tide

Figure 4.19: Subtidal near-bed concentrations in (kg/m^3) for (a) neap tidal conditions and (b) spring tidal conditions found for varying depth averaged concentrations at the seaward boundary. Note: these results are found by increasing the sediment concentrations.

Like the sensitivity study for river discharge, the sensitivity study for the seaward concentrations has been performed for increasing as well as decreasing concentrations. Considering neap tidal conditions, high sediment concentrations could even be found for a seaward concentration of 0.07 g/l while coming from the hyperturbid state. This influence of the 'history' of the estuary is even more pronounced when we consider spring tidal conditions. In Figure 4.20, the maximum sediment concentration in the ETM has been shown for increasing and decreasing concentrations at the seaward boundary. While increasing the concentrations, sediment concentrations remain low up to 0.5 g/l, whereas the system remains hyperturbid while decreasing the concentrations down to 0.3 g/l.

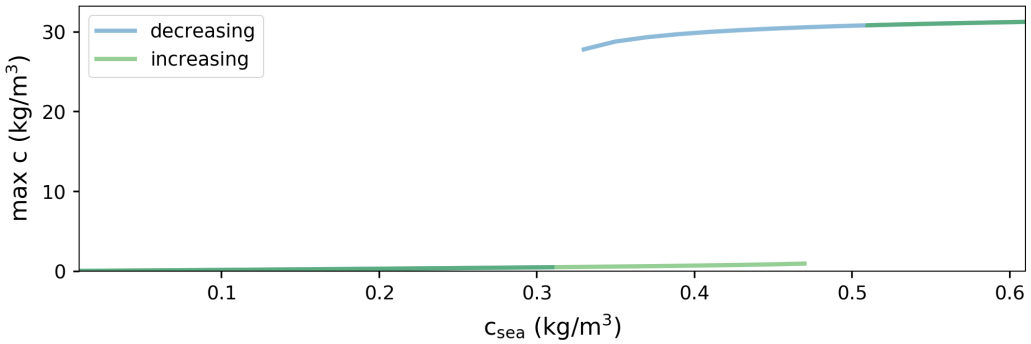

Figure 4.20: Maximum near-bed sediment concentrations that can be found for increasing (green) and decreasing (blue) c_{sea}, considering spring tidal conditions.

If we take a closer look at the sediment concentrations along the estuary for neap tide right after the transition to high concentrations (so for $c_{sea} > 0.1$), sediment concentrations tend to increase accompanied by a seaward shift of the ETM until c_{sea} reaches a value of approximately 0.3 g/l, after which it remains constant. This increase in concentrations might be surprising, since we stated that the sediment concentration in the

ETM was erosion limited (f=1). It should therefore depend on the erosive capacity of the flow, not the concentration at the mouth of the estuary. The key for explaining this phenomenon is the small seaward shift of the ETM for c_{sea} between 0.1 and 0.3. Although the erodibility f equals 1 at the location of the bottom pool, an increasing sediment concentration at the seaward boundary results in an increasing availability in the rest of the estuary. The combination of the erodibility and the potential erosion governs the sediment concentrations, hence it might be possible that an erodibility slightly less than 1, combined with a much higher potential erosion results in higher concentrations than an erodibility of 1 and a limited potential erosion. These thoughts are confirmed by Figure 4.21a and Figure 4.21b, in which the erodibility and the potential erosion along the estuary for increasing c_{sea} are presented respectively. In both figures, the location of the ETM found for neap tidal conditions is presented with a thin grey line. It can be clearly seen that the ETM shifts towards a region with slightly lower erodibility and higher potential erosion.

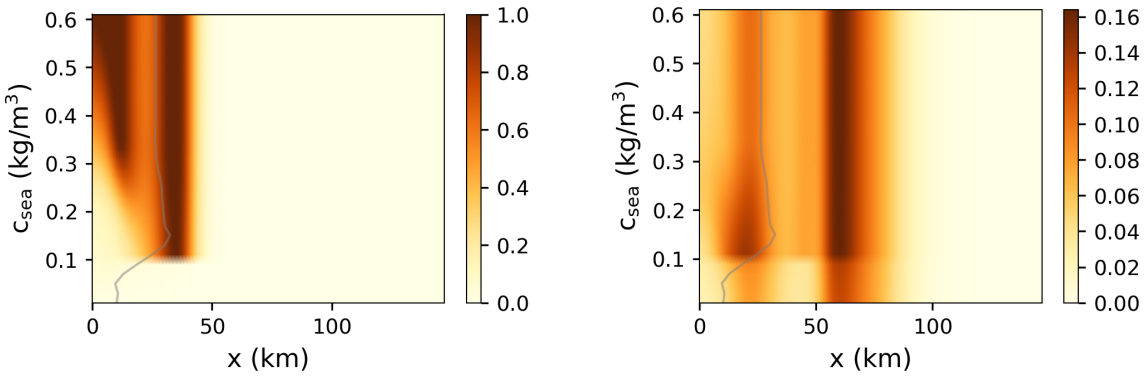

(a) Erodibility f along the estuary for varying c_{sea}

(b) Potential erosion $\bar{E}$ along the estuary for varying c_{sea}

Figure 4.21: Erodibility and potential erosion along the estuary for different c_{sea}, considering neap tidal conditions. For increasing c_{sea}, the ETM (grey line) shifts towards a region with higher potential erosion and lower erodibility.

4.4.3. SENSITIVITY TO THE CLEAR WATER SETTLING VELOCITY $w_{s,0}$

One of the parameters that captures the sediment characteristics in the model is the clear water settling velocity $w_{s,0}$. In reality, the clear water settling velocity might be different for each individual floc and changes over time and space due to flocculation, so if we define it as a single parameter for all sediment in the estuary, it is important to investigate the sensitivity of the model regarding this value. The model sensitivity has been tested for settling velocities between 0.1 and 4.0 mm/s. The resulting near-bed suspended sediment concentrations along the estuary for neap and spring tidal conditions are presented in Figure 4.22a and Figure 4.22b, respectively.

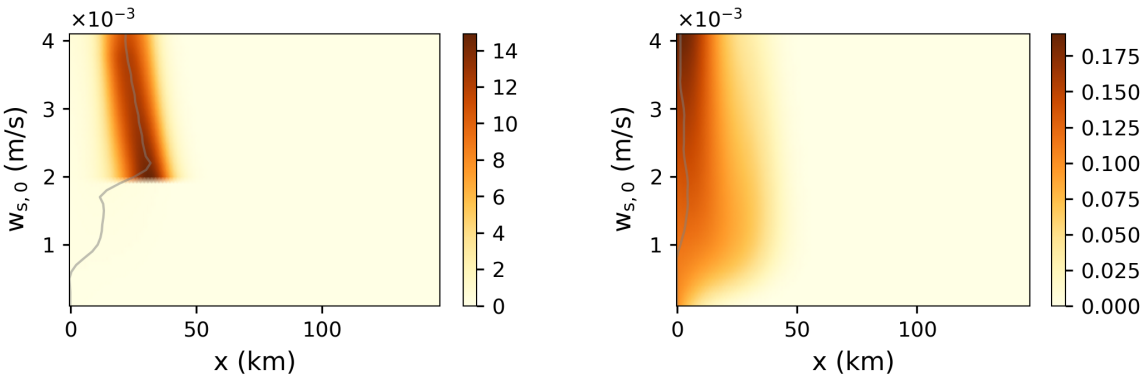

(a) Neap tide

(b) Spring tide

Figure 4.22: Subtidal near-bed concentration in (kg/m^3) along the estuary for (a) neap tidal conditions and (b) spring tidal conditions, considering an increasing clear water settling velocity $w_{s,0}$

For settling velocities below 1 mm/s, both for neap and spring tidal conditions sediment concentrations are low and the ETM is located at or close the seaward boundary. Increasing the settling velocity hardly has any influence for spring tidal conditions, except a slight increase in the sediment concentrations near the bottom (and, although not presented here, decreasing concentrations at the surface). This finding can be explained with the Rouse-number which describes the ratio between the downward (settling velocity) and upward velocity (product of the van Karman constant and shear velocity) of a sediment floc (Rouse, 1938). As long as sediment-induced turbulence damping only is of minor importance, which is the case for spring tide, the hydrodynamic forcing remains more or less constant, and hence the shear velocity remains more or less constant. As a consequence of increasing the settling velocity, the rouse number goes up, indicating a more stratified sediment distribution over the water column. For neap tidal conditions, increasing the settling velocity results in a landward shift accompanied by increasing near-bed concentrations. Once the clear bed settling velocity becomes 2 mm/s, a sudden jump in the sediment concentrations along the estuary can be observed. As we have observed before, this sudden increase in sediment concentrations is found once sediment-induced turbulence damping starts playing a significant role. Further increasing the settling velocity causes a seaward shift of the ETM and a reduction of the maximum concentrations.

4.4.4. SENSITIVITY TO THE EROSION PARAMETER M

The last parameter for which a sensitivity study has been performed is the erosion parameter M, which has a proportional influence on the potential erosion $\tilde{E}$. The initial value of 0.01 was based on research considering hyperturbidity in the Ems (van Maren et al. (2015), Dijkstra et al. (2019c)), but was mainly chosen such that high concentrations could occur. To quantify the influence of the erosion parameter, its value has been varied within the range of 10^{-4} - 10^{-1}. The resulting near-bed sediment concentrations along the estuary for neap and spring tidal conditions are presented in Figure 4.23, with the ETM indicated with a thin grey line.

Looking at the results for neap tidal conditions in Figure 4.23a, we can observe three phases. Starting with an erodibility $M = \mathcal{O}(10^{-4})$, the ETM can be found around 10 km from the mouth. For an erodibility $M = \mathcal{O}(10^{-3})$, a landward shift of the ETM towards km 30 can be observed. Though hard to see in the figure, near-bed concentrations already exceed 1 g/l for $M = 10^{-3}$, so that sediment-induced turbulence damping is responsible for the shift of the ETM. Increasing the erodibility up to $2 \cdot 10^{-2}$ results in proportionally growing sediment concentrations. This is a clear indication that the sediment concentrations were erosion limited for $M < 2 \cdot 10^{-2}$. For values of M larger than $2 \cdot 10^{-2}$, sediment concentrations along the estuary remain constant although the potential increases, the sediment concentrations are supply limited.

Considering the results for spring tidal conditions, the influence of M is limited. If we remember the analysis of the spring tidal case in section 4.3, this is not surprising. The sediment concentrations were found to be supply limited, so increasing the potential erosion by increasing M should not have any effects. Nevertheless, it can be seen that for values of M around 10^{-4}, much lower than the initial value of 0.01, the sediment concentrations become erosion limited.

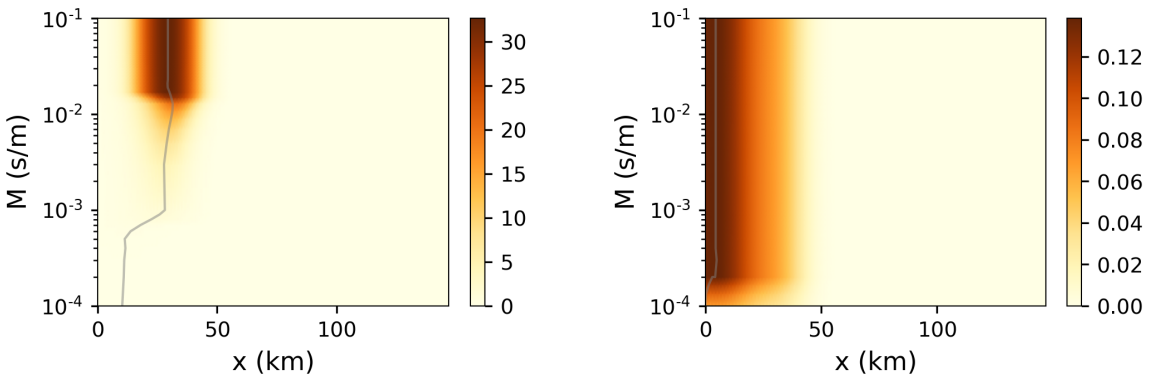

(a) Neap tide

(b) Spring tide

Figure 4.23: Subtidal near-bed concentration in (kg/m^3) along the estuary for (a) neap tidal conditions and (b) spring tidal conditions, considering an increasing erosion parameter M

4.4.5. REMARKS CONCERNING SENSITIVITY STUDIES

In the previous subsections, the results of multiple sensitivity studies were presented to discuss the robustness of the results found in section 4.2 and subsection 4.3.1. In this section, some remarks will be made to wrap-up the findings of the different sensitivity studies for neap and spring tide separately.

NEAP TIDE

For neap tidal conditions, the transitions from low to high sediment concentrations are strikingly close to the default values of c_{sea}, $w_{s,0}$ and M, which are used for calibration. The fact that all transitions happen exactly at or close to the default chosen values raised the question whether this is a coincidence, since these observations create the impression that the choice of the default values is governing for the behaviour of the system. Combined sensitivity studies are used to investigate the role of these default choices in the results discussed so far. Each time, two parameters are varied while keeping all other parameters constant. Only the most eye-catching findings are presented below.

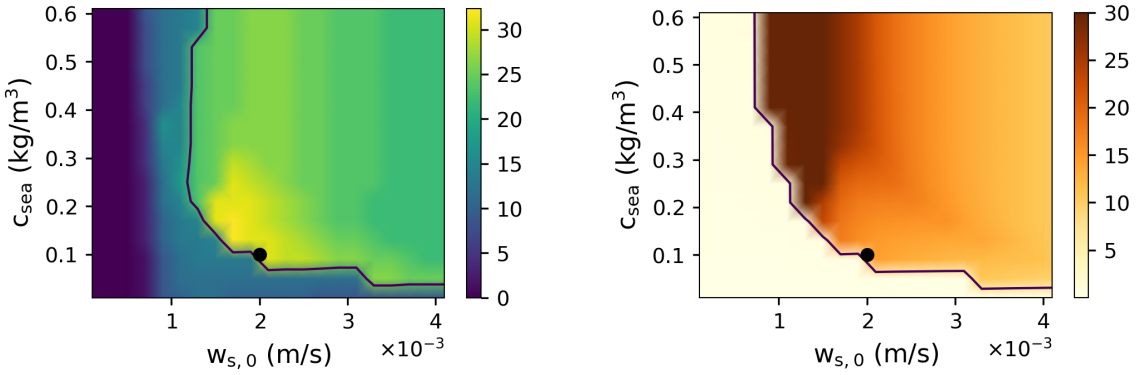

(a) ETM location (km)

(b) Maximum near-bed concentration (kg/m^3)

Figure 4.24: Location of the ETM in km from the mouth (a) and the maximum near-bed concentration in kg/m^3 (b) for varying c_{sea} and $w_{s,0}$, with in black contour lines for 20 km (a) and 5 kg/m^3 (b) and the black dot representing initial values.

In Figure 4.24, the location of the ETM and the maximal near-bed concentration in the ETM are plotted for varying c_{sea} and $w_{s,0}$ (for constant z_0^*). The black contour lines, representing 20 km in Figure 4.24a and 5 g/l (values often mentioned in literature while discussing hyperturbidity in the Loire estuary, see chapter 1) in Figure 4.24b, are used as a distinction between the low sediment concentration state and the hyperturbid state. As expected from the single parameter sensitivity analyses, the black dot representing default values is located at the transition from low to high concentrations. However, it can also be seen that there are much more combinations of these two parameters that result, for an equal value of the dimensionless roughness parameter z_0^*, in hyperturbid conditions.

Comparable results are found, amongst others, for combinations of the seaward sediment concentration with the river discharge and erosion parameter as presented in Appendix D, and river discharge and settling velocity (not shown). These combined sensitivity studies show that although the default chosen conditions resulted in a roughness value such that the M_2 water level amplitude and phase were reproduced optimally, multiple other combinations of default values would have resulted in qualitatively similar results, and hence this coincidence does not affect the robustness of the results.

SPRING TIDE

In subsection 4.3.1 it was suggested that also for spring tidal conditions a tipping point could exist at which the sediment supply became large enough for the system to turn hyperturbid. Such a tipping point was indeed found in the sensitivity analysis for c_{sea} once the depth averaged sediment concentration at the seaward boundary increased 0.5 g/l. Once hyperturbid, c_{sea} could decrease down to 0.3 g/l before the sediment concentrations became low again. As a consequence of this hysteresis, two equilibrium states exist for values of c_{sea} between 0.3 and 0.5 g/l as can be seen in Figure 4.20. For the low concentration state, we stated that

the M_2- and M_4 water level amplitudes were underestimated by the model, whereas the phases were slightly overestimated (i.e. underestimation of the propagation of the tidal waves). In Figure 4.25, water level amplitudes and phases are presented for the estuary in hyperturbid state (c_{sea}=0.39 while decreasing). It can be seen that both the M_2- and the M_4 water level amplitudes got amplified in the hyperturbid state, though this amplification is slightly overestimated. Although the general patterns of the tidal phases are captured well, especially the M_4 tidal phase is underestimated significantly.

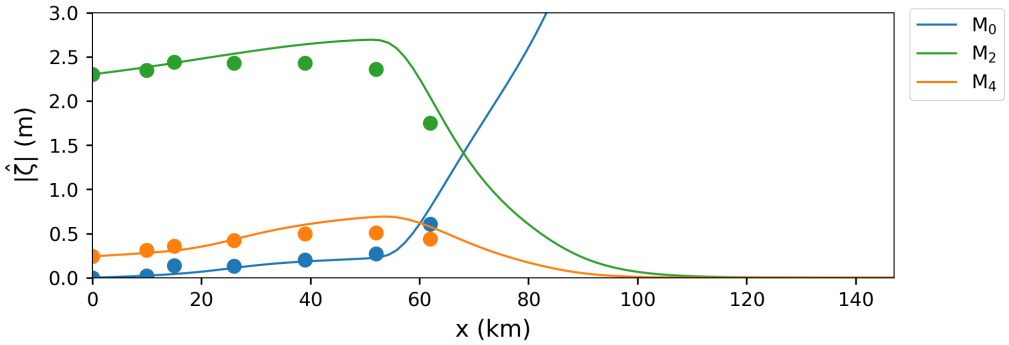

(a) Water level amplitude

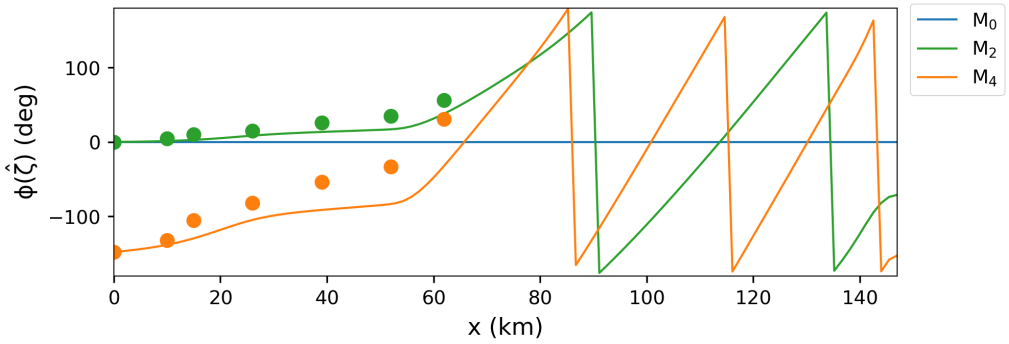

(b) Water level phase

Figure 4.25: Modelled (solid lines) and observed (dots) water level amplitude and phase of the subtidal M_0 (blue), M_2 tide (green) and M_4 tide (orange) for spring tide, in case of hyperturbid conditions.

In Figure 4.26, the individual contributions to the transport capacity are compared between the cases with low- and high sediment concentrations for spring tidal conditions. A comparison was made for a value for c_{sea} of 0.39 kg/m^3 at which the system has two equilibrium states (see Figure 4.20). Like we found for neap tidal conditions, contributions due to the external M_4 tide and the baroclinic pressure gradients got amplified. However, unlike we found for neap tidal conditions, contributions due to sediment advection and river flow are amplified significantly as well. As a consequence, the total transport capacity still shows importing and exporting regions in the first 50 km of the estuary, resulting in a restricted supply of sediments towards the ETM. With other words, even for hyperturbid conditions the Loire estuary remains supply limited ($f < 1$ in the ETM, not shown) for spring tidal conditions.

In this chapter, we have seen that the Loire estuary in hyperturbid state tends to import fine sediments during neap tide. During spring tide however, the Loire still has a strong tendency to export sediments in the first part of the estuary, even when the estuary is in hyperturbid state. In this research, the supply limitation of the sediment concentrations during spring tide has been overcome by increasing the depth averaged sediment concentration at the seaward boundary to 0.5 g/l. Though this concentrations is measured from time to time, it is uncommon during periods of low river discharge. In reality, high concentrations of suspended sediment are especially measured during spring tide. Therefore, based on the findings of this chapter, we hypothesize that sufficient easy fine sediment is imported during neap tide to reach high sediment concentrations in the ETM during spring tide.

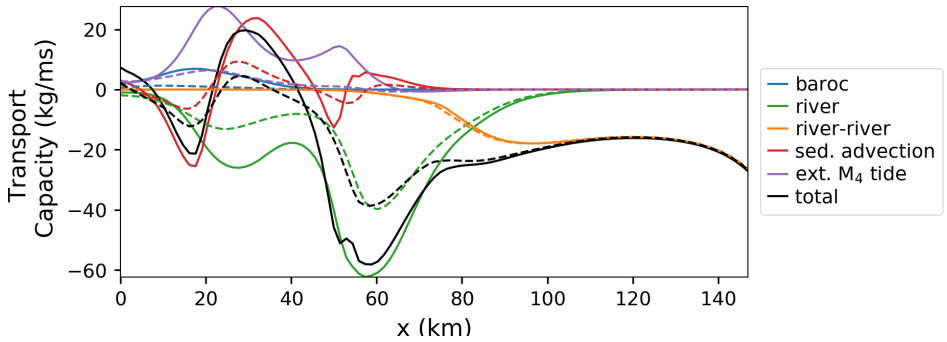

Figure 4.26: A comparison of the various contributions to the total transport capacity (in black) considering spring tidal conditions for low- (dashed lines) and high concentrations (solid lines)

5

CONSEQUENCES OF DEEPENING

Human interventions in the Loire estuary have taken place for centuries. Focussing on the 20th century, these interventions mainly comprised deepening campaigns. Alongside these deepening campaigns, significant amplification of the tidal range and sediment concentrations in the Loire observations are observed. Main question that will be answered in this chapter is whether these deepening activities can be held responsible for these observed changes in tidal range and sediment concentrations.

5.1. RESPONSE TO DEEPENING

To investigate the response of the Loire estuary to deepening activities, model simulations have been performed in which only the depth has been varied. Starting with the 1900 bathymetry (α=0) and increasing the depth towards the current bathymetry (α=1, see Equation 3.3) keeping all other model parameters constant.

5.1.1. TIDAL RANGE

A first indication of the relation of the depth-parameter α to the corresponding year has been given in chapter 3, based on deepening campaigns. Another way to link the value of the depth-parameter α to intermediate years between 1900 and 2010, is to compare observed and modelled tidal ranges. As tidal ranges for low discharges are mainly reported for spring conditions, this comparison is done for spring conditions. However, since the hyperturbid conditions are not captured by the model while using the default settings (see Table 3.7), the model results obtained for c_{sea} = 0.5 g/l are used instead. In addition to that, the tidal coefficient (i.e. the amplitudes of the tidal constituents at the boundary) occurring during measurements and used for model computations do not entirely match. Therefore, the observed tidal ranges are corrected by multiplying with the ratio of the modelled tidal range divided by the observed tidal range at the boundary, such that the tidal ranges at the boundary match for observations and model results. In Figure 5.1 both observed (corrected) and modelled spring tidal ranges along the estuary are plotted. Though the bathymetry around 1900 is represented by α=0, the observed tidal range in 1903 lies somewhere in between the modelled tidal ranges for α=0 and α=0.25. The shapes of the observed tidal ranges of 1938, 1978 and 1998-2011 are reproduced quite well for α-values of 0.7, 0.9 and 1.00 respectively. The overestimation of the tidal range between km 30 and 60 was already presented in subsection 4.4.5, and was caused by the amplification of the tides due to high sediment concentrations.

Figure 5.2 shows the link between the depth-parameter α and the corresponding year between 1900 and 2010, based on two different approaches. In chapter 3, it was already mentioned that significant deviations are observed between the intermediate bathymetries and the depth obtained by dredging campaigns. If we look back at that approach (see Figure 3.5), these deviations are especially found near km 20 and km 40. The current depth around km 20 was already reached around 1970 (see Figure 3.4. The depth of the estuary reaches its minimum around km 20, which makes the depth at that location important for correct modelling the tidal propagation. Apparently, a larger depth around km 20 is necessary to better capture the tidal motions. This explains why we find a faster increase of the α-value when we look at the tidal ranges. Since this approach better captures the hydrodynamics within the first part of the estuary, the link between α and years found with this approach is preferred.

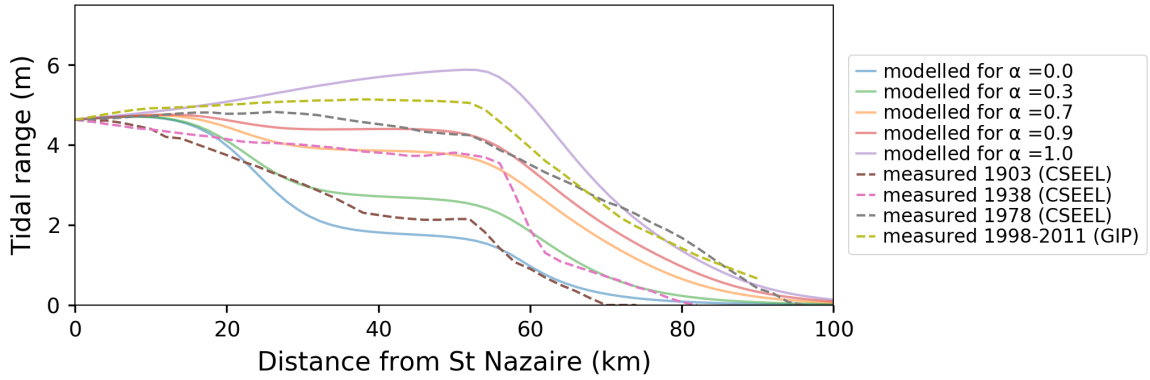

Figure 5.1: Modelled (solid lines) and observed(dashed lines) tidal ranges along the Loire estuary considering spring tidal conditions and an average summer discharge of 250 m^3/s.

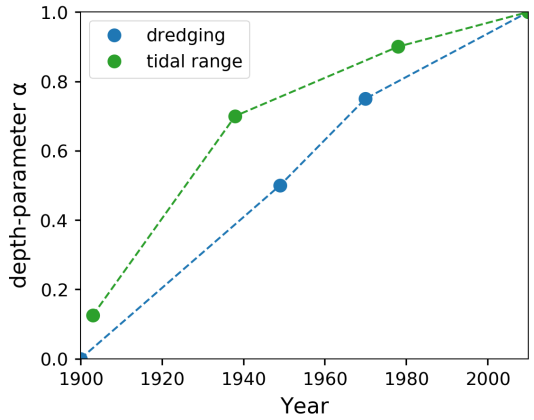

Figure 5.2: Estimation of the link between the depth-parameter α and the corresponding year, based on depths obtained by dredging campaigns (blue) or based on a comparison of observed and modelled tidal ranges (green).

5.1.2. SEDIMENT CONCENTRATIONS

The resulting subtidal near-bed concentrations along the estuary for neap and spring tidal conditions as presented in Figure 5.3. Regarding neap tidal conditions (Figure 5.3a), it can be seen that the ETM starts to shift landward for alpha values larger than 0.5. However, for α-values larger than 0.9, this landward shift is accelerated, followed by a sudden jump in sediment concentrations for $\alpha \approx 0.95$. From this, we can already state that deepening activities were important for the Loire estuary to turn hyperturbid. In chapter 4, we have already seen that such a strong jump in sediment concentrations was found once sediment-induced turbulence damping became important. Based on the data presented in chapter 3, this jump in sediment concentrations was expected for lower α-values. At first, this may be the case because the bathymetry between 1900 and now is approximated by linear interpolation between two bathymetrical profiles, but this doesn't necessarily imply that the relation between alpha and years has to be linear as well (see Figure 5.2). Secondly, we have seen that the history of the estuary has a large influence on the actual state due to the hysteresis phenomenon. And at last, we should be aware of the uncertainties of the model input.

For spring tidal conditions the jump to the hyperturbid regime is not captured by increasing the α-value, but a landward shift of the ETM can be observed accompanied by widening of the ETM (see Figure 5.3b). Simulation results show that further deepening of the Loire estuary might eventually result in hyperturbid conditions, though only in the case of extreme deepening (approximated by extrapolating α to a value of 2.5 (not shown)). In subsection 4.4.2, we have seen that while considering spring tidal forcing for the current bathymetry, hyperturbid conditions could be found for depth averaged sediment concentrations at the sea-

ward boundary exceeding 0.5 g/l. Based on that finding, a sensitivity study has been performed for spring tidal condition with c_{sea} equalling 0.5 g/l. For that case, a sudden jump in sediment concentrations could be observed for α-values larger than 0.95 (like for neap tidal conditions, not shown).

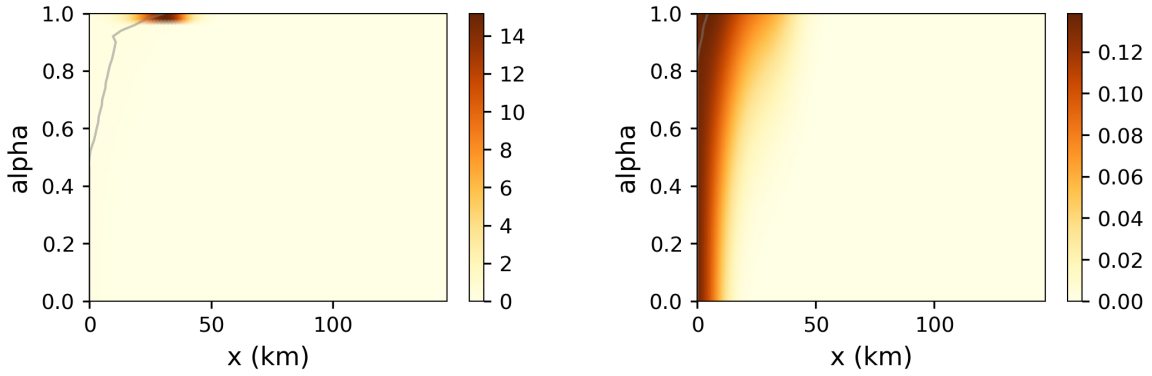

(a) Neap tide

(b) Spring tide

Figure 5.3: Subtidal near-bed sediment concentrations in (kg/m^3) considering neap and spring tidal conditions and an average summer discharge of 250 m^3/s for increasing depth (α), with the location of the ETM represented with a thin grey line. The bathymetry in the year 1900 is represented by α=0, and the bathymetry around the year 2000 by α=1.

Figure 5.4 shows the maximal sediment concentrations in the estuary considering both deepening and undeepening (increasing- and decreasing α respectively) for the neap tidal case. Coming from the hyperturbid state, we can see that hyperturbid conditions can be found until alpha drops below 0.7. We have already seen that the history of the estuary plays an important role in the actual state of the estuary. So when conditions exist for which high sediment concentrations already occur for lower alpha values, we see that for the default settings (average summer conditions) the estuary could remain hyperturbid for α larger than 0.7. Whether it is likely that such conditions exist will be investigated more thoroughly in section 5.3.

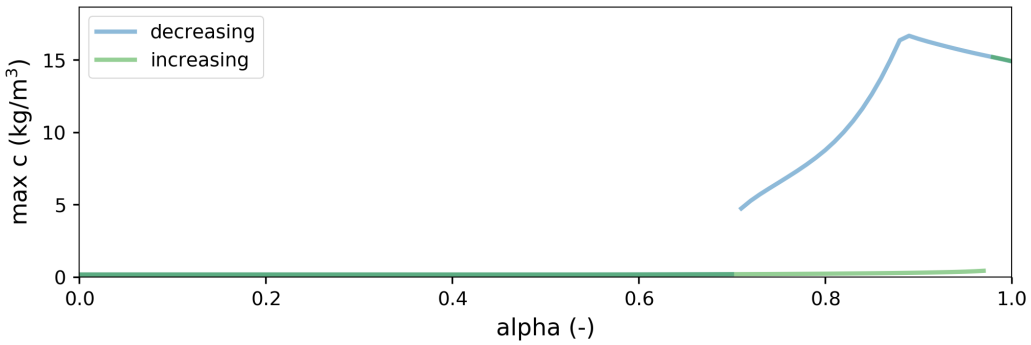

Figure 5.4: Maximum near-bed sediment concentrations that can be found for increasing (green) and decreasing (blue) α considering neap tidal conditions.

5.2. ANALYSIS OF PHYSICAL MECHANISMS

In Figure 5.5 the total transport capacities for increasing α-values considering neap tidal conditions are depicted. For α-values increasing from 0 to 0.97, an increasing sediment import can be observed along the first 5 km of the estuary, whereas the exporting transport capacity between km 5 and 40 reduces significantly. For $\alpha > 0.98$, the transport capacity of the Loire estuary becomes importing along the first 35 km. We already know that this sudden jump in the total transport capacity coincides with the sudden jump from low to high sediment concentrations. A closer look to the various contributions to the total transport capacity and their development over time should provide some more insight in the actual causes of this transition.

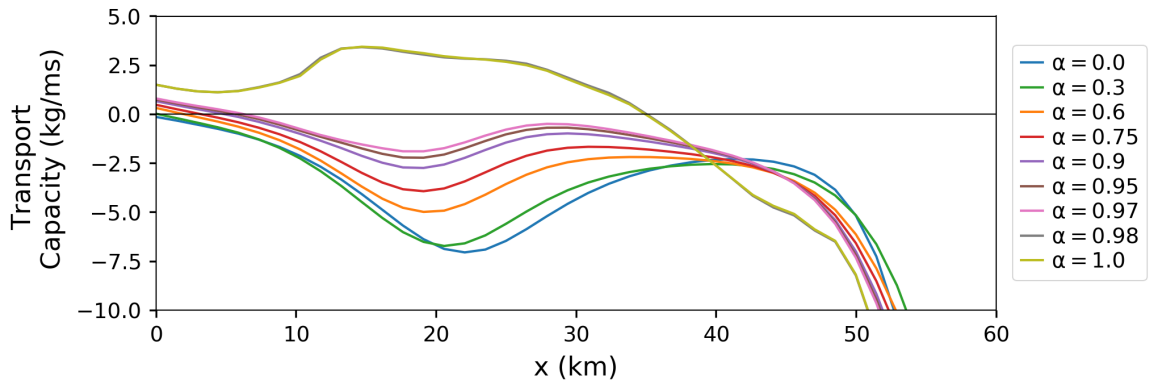

Figure 5.5: The total transport capacity considering neap tidal conditions and an average summer discharge of 250 m^3/s for an increasing depth, with $\alpha = 0$ representing the bathymetry in 1900 and $\alpha = 1$ representing the Thalweg levels in the year 2000.

5

For the 6 most important mechanisms in the year 1900, their contribution to the total transport capacity is shown in Figure 5.6 for the 4 key-years as mentioned in Figure 3.5. To visually capture the effect of the high sediment concentrations, the transport contributions for an alpha-value of 0.95 are plotted as well. Furthermore, in contrast to the analysis of the current state of the estuary presented in chapter 4, the contributions due to tidal return flow and velocity-depth asymmetry are considered in this analysis as well (explained below). Regarding development over time, especially these two contributions were subject to significant changes. For each of the six contributions to the total transport, the changes over time are discussed below:

- At first we look at the *baroclinic* contribution to the transport capacity (Figure 5.6a). While increasing the depth, the transport capacity caused by density driven flows increases as well. The increase in transport capacity is gradual up to $\alpha = 0.95$, after which the contribution got amplified significantly. The gradual increase is caused by the strengthening of the gravitational circulation due to deepening, while the sudden amplification is due to the strong sediment stratification once the estuary is hyperturbid.
- If we look at the contribution of the transport capacity due to the *external* M_4*-tide* (Figure 5.6b) deepening has had pronounced effects. Starting with $\alpha = 0$, the tidal asymmetry caused sediment import in the first 10 km, but export of sediments in the rest of the estuary. This exporting character tends to shift to an importing character for increasing alpha. For alpha-values exceeding 0.3, the external M_4 tide causes import of sediments in the first 50 km of the estuary. Once the estuary turns hyperturbid, a strong amplification of this contribution can be observed along the entire first 60 km.
- Changes in depth only had limited effects on the contribution due to *sediment advection* (Figure 5.6c). Its tendency to move sediments towards the location with minimal tidal velocities results in equally shaped transport capacity curves. As a consequence of the increasing depth, tidal velocities increased, which in turn caused the contribution to sediment advection to increase gradually. Once high sediment concentrations are found, the velocity profile along the estuary changes resulting in a shifted, but similarly shaped transport capacity curve.
- The exporting contribution due to the *river* (Figure 5.6d) remained fairly constant over the years. As a consequence of deepening, river induced velocities are reduced for equal river discharge. However, as long as the sediments stirred up by the tidal motion are distributed fairly uniformly over the water column, the integral of the velocities over depth times the uniform distributed sediment profile remains equal. This explains why the contribution to the transport capacity due to the river remains constant. Nevertheless, once the sediment distribution over the water column gets more stratified, changes in the velocity profile got important as well. This is why the exporting contribution slightly decreases once high sediment concentrations are found.
- Within iFlow, the contribution due to Stokes drift and a corresponding return flow is captured by the *tidal return flow* contribution (Figure 5.6e). Stokes drift, firstly described by Stokes (1847), is the residual motion of a water particle in the direction of the wave caused by the difference in velocities in its orbital motion. Water particles moving slightly faster under the crest of the wave than under the through causing a net mass transport, accompanied by import of sediment. This net mass transport is com-

pensated by the tidal return flow, which typically causes export of sediments (Longuet-Higgins, 1969). Figure 5.6e shows that this tidal return flow is dominating the transport capacity for $\alpha < 0.95$. However, the exporting capacity reduces significantly for increasing depth over the first 30 km. For $\alpha = 1$, the contribution due to the Stokes drift becomes dominating, hence sediments import can be observed.

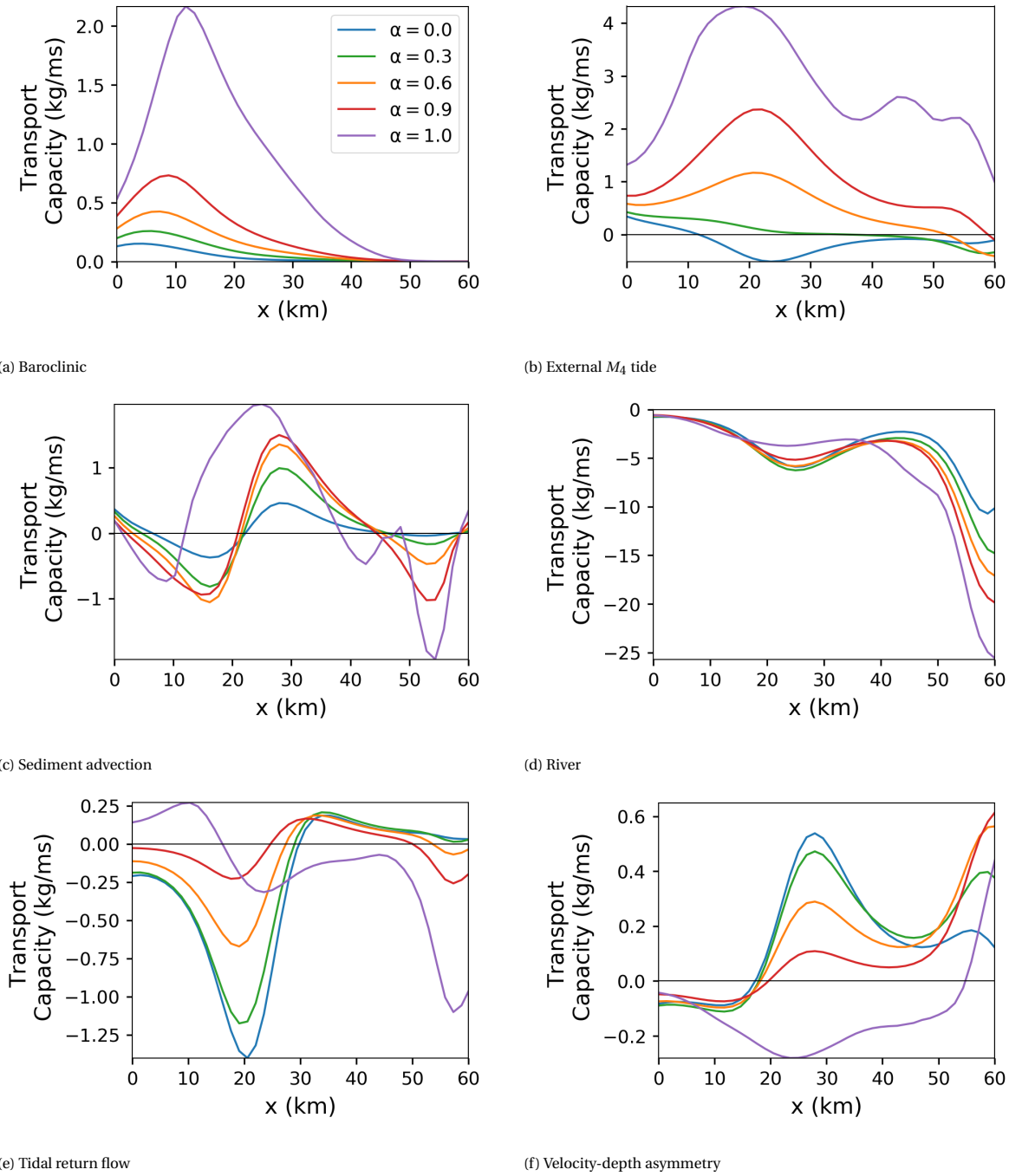

(a) Baroclinic

(b) External M_4 tide

(c) Sediment advection

(d) River

(e) Tidal return flow

(f) Velocity-depth asymmetry

Figure 5.6: The development over time of the various contributions to the total transport capacity indicated with α-values corresponding to the key-years from Figure 3.5. In each sub figure, the transport capacity corresponding to $\alpha = 0$ is depicted in blue, for $\alpha = 0.25$ in green, for $\alpha = 0.60$ in orange and for $\alpha = 1.00$ in red.

- The water level varies over a ebb-flood cycle, and hence the depth changes. Due to this depth variation, the velocity profile varies. This is captured in the transport capacity by the *velocity-depth asymmetry* (Figure 5.6f). For all values of alpha, the contribution to the transport capacity has an exporting char-

acter between km 0 and 15. From km 15 onwards, the transport capacity due to the velocity-depth asymmetry becomes importing as long as sediment concentrations remain low. For $\alpha = 1$, its contribution becomes exporting along the entire first 50 km. With respect to the other contributions to the total transport capacity, the contribution due to velocity-depth asymmetry is only important for small α-values.

To conclude this section, we stepwise summarize the effects of deepening on the different physical processes in the Loire estuary. At first we restrict ourselves to the first 20 km of the estuary and only look at cases with low sediment concentrations ($\alpha \leq 0.95$). All described changes, except sediment advection, have a positive or neutral effect on the import of sediments. If we look at the section of the estuary between km 20 and 50, only the changing velocity-depth asymmetry acts unfavourable regarding sediment import. These changes in the different contributions explain the changes in the total transport capacity as presented before in Figure 5.5. At some point, the sediment supply becomes large enough for the estuary to turn hyperturbid. At that point, the importing contributions due to the baroclinic transport and the external M_4 tide got amplified, the export by the river got dampened and the contributions to the total transport capacity due to the tidal return flow and the velocity-depth asymmetry got reversed.

5

5.3. SENSITIVITY STUDY

We have seen that the estuary had a strong exporting character before the deepening activities took place. This exporting character decreased gradually for increasing depth, and at some point the estuary turned hyperturbid. When this transition happened in reality is hard to determine from the data. In addition to that, we have seen that different model settings may make the modelled system more susceptible to high sediment concentrations.

To investigate for which α hyperturbid conditions could be found in the estuary, an extensive sensitivity study has been performed for neap tidal conditions by varying multiple input parameters. Besides the depth α ,the other parameters that have been varied are the clear water settling velocity $w_{s,0}$, the seaward depth averaged sediment concentration c_{sea} and the river discharge Q_1. The ranges between which these parameters have been varied are chosen in the same way to the single-parameter sensitivity studies discussed in section 4.4. For every experiment, with a total number of experiments equal to 14.157 (1287 different conditions for 11 depth-profiles), we are interested in the location and the magnitude of the ETM. For stability reasons of the iFlow model, the α values are run from high to low, hence starting with a recent bathymetry towards a historical bathymetry. As a consequence of the hysteresis which we observed before (see Figure 5.4), when hyperturbid conditions are found for $\alpha = 1$, these hyperturbid are more likely to be found for lower values of α as well. Therefore, results should be treated with care.

The maximum near-bed sediment concentrations along the estuary for all single experiments have been collected in a 2D histogram which is presented in Figure 5.7. The darker the colour of the bin, the more experiments fell in that bin, hence the higher the probability of occurrence of that near-bed suspended sediment concentration. Distinction can be made between several zones. At first, the first bin in the vertical (0-1 kg/m^3) represents most of the experiments. From left to right, so for increasing depth, the intensity of the colour decreases. This means that a deeper estuary is less likely to have a low maximum concentration. Another typical zone is 1-5 kg/m^3. Sediment concentrations within this range are likely to occur for low values of alpha, and the likelihood to find such concentrations decreases while alpha increases. Further analysis shows that experiments within this band corresponds to experiments with an ETM between 0-20 km (not shown). Apparently for certain input parameters and low alpha-values, sediment concentrations in this range could occur without initiating the sediment-induced turbulence damping, and therefore without shifting to the hyperturbid state. The third typical zone covers maximum concentrations larger than 5 kg/m^3. We can see that for low values of alpha, there are no experiments that resulted in sediment concentrations larger than 5 kg/m^3. For increasing alpha, starting at $\alpha = 0.2$, we can observe a gradual increase in colour intensity, indicating that it becomes more likely to find sediment concentrations in this range. Though the colour is not so intense, indicating a low probability of occurrence, sediment concentrations up to 50 kg/m^3 are found for certain input parameters.

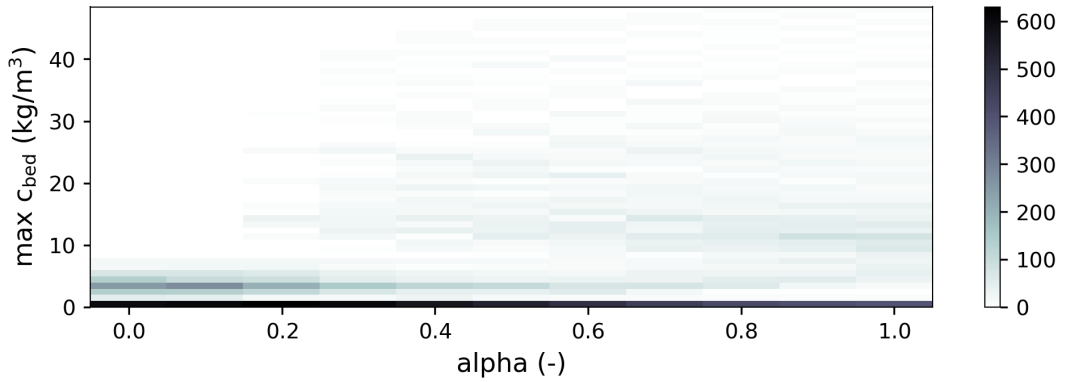

Figure 5.7: 2D histogram indicating for every value of alpha (0, 0.1, 0.2 and so on) the number of experiments for which the maximum near-bed sediment fell in a certain range. The bins on the y-axis have a size of 1 g/l.

Figure 5.8 shows a similar 2D histogram for the location of the ETM. Like we found for the maximum sediment concentration, the highest colour intensity is found in the lowest bin (0-1 km). When the location of the ETM is found in the first km of the estuary, the ETM is washed out of the estuary entirely. For increasing values of alpha, distinction can be made between two bands. The first band ranges between 1-20 km, while the second can be found between 25-40 km. Both bands have an increasing colour intensity for increasing values of alpha, which means that a deeper estuary is more likely to have an ETM more landward. Regarding the lower band, we see that increasing the depth results in a landward shift of the ETM. Similar results have been found in Figure 5.3a, where we observed a gradual landward shift of the ETM followed by an accelerated shift around α = 0.95. The higher band captures the simulations for which the ETM was located between km 25 and 40. Using the default settings, we have seen that once the estuary turned hyperturbid, the ETM shifted towards this region. Nevertheless, for increasing alpha, a gradual seaward shift of the ETM can be observed. The seaward shift for larger depth follows from the balance between the importing contribution due to the external M_4-tide and the exporting contribution due to the river. For a highly stratified estuary, a larger depth reduces the exporting contribution due to the river, since the river-induced velocities near the bottom are reduced. Nevertheless, the importing contribution due to the external M_4 tide got damped even more, resulting in a net seaward shift of the ETM.

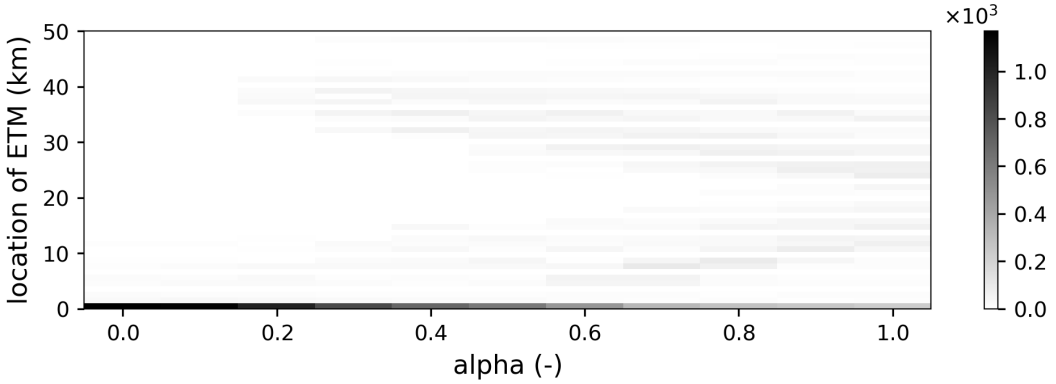

Figure 5.8: Number of experiments per value of alpha for which the ETM is located at a certain location. The bins on the y-axis have a size of 1km.

When hyperturbidity in the Loire is discussed in literature, the location of the ETM is always considered to be around Cordemais (km 26) or further landward. For that reason, we will investigate the experiments causing an ETM in the upper band in more detail. By restricting the experiments of interest even more while only focussing at the experiments that actually resulted in hyperturbid conditions (max $c_{bed} > 5$ g/l), some insight

could be obtained in the importance of the different input parameters.

For the alpha-values 0, 0.3, 0.6, 0.9 and 1, the model input ($Q_1, c_{sea} and w_{s,0}$) has been analysed of the experiments that resulted in near-bed concentrations larger than 5 g/l between 25 and 40 km from the mouth. For each value that these three input parameters could obtain, the number of experiments fulfilling these restrictions has been plotted in Figure 5.9. Starting with the river discharge, it can be seen that for discharges below 200 m^3/s, hyperturbid conditions already could occur for α = 0.3. However, for discharges larger than 200 m^3/s, hyperturbidity is not found any more for α = 0.3, and the number of experiments resulting in hyperturbidity for larger values of alpha also reduces significantly. For a river discharge of 450 m^3/s, only for α = 0.9 and α = 1.0, very limited experiments with high sediment concentrations are found.

The same analysis has been done for the depth-averaged sediment concentration at the seaward boundary. The larger this concentration, the more simulations resulted in high sediment concentrations between km 25 and 40. Besides that, we can clearly see that the likelihood that the system is hyperturbid increases for increasing alpha. Even for simulations with c_{sea} = 0.01, high sediment concentrations could be found for sufficiently large depth ($\alpha > 0.9$).

The last input parameter that has been analysed is the clear-water settling velocity $w_{s,0}$. For very small settling velocities, no high sediment concentrations are found. However, where we found the shift towards high sediment concentrations in the single-parameter sensitivity study of section 4.4 exactly at 0.002 m/s, this study shows that this regime shift could also be obtained with smaller settling velocities.

In this section, we have seen that an increasing depth always leads to an increased likelihood to find high sediment concentrations, independent of the conditions. A similar sensitivity study is performed for spring tidal conditions. Since qualitatively similar results are found, these are not treated in detail here. The main result that followed from the spring tidal analysis is that also for spring tidal conditions no hyperturbid state could be found for low values of α, and for $\alpha > 0.5$, the likelihood to find hyperturbid conditions increased with increasing α, accompanied by a landward shift of the ETM. Detailed results can be found in Appendix E.

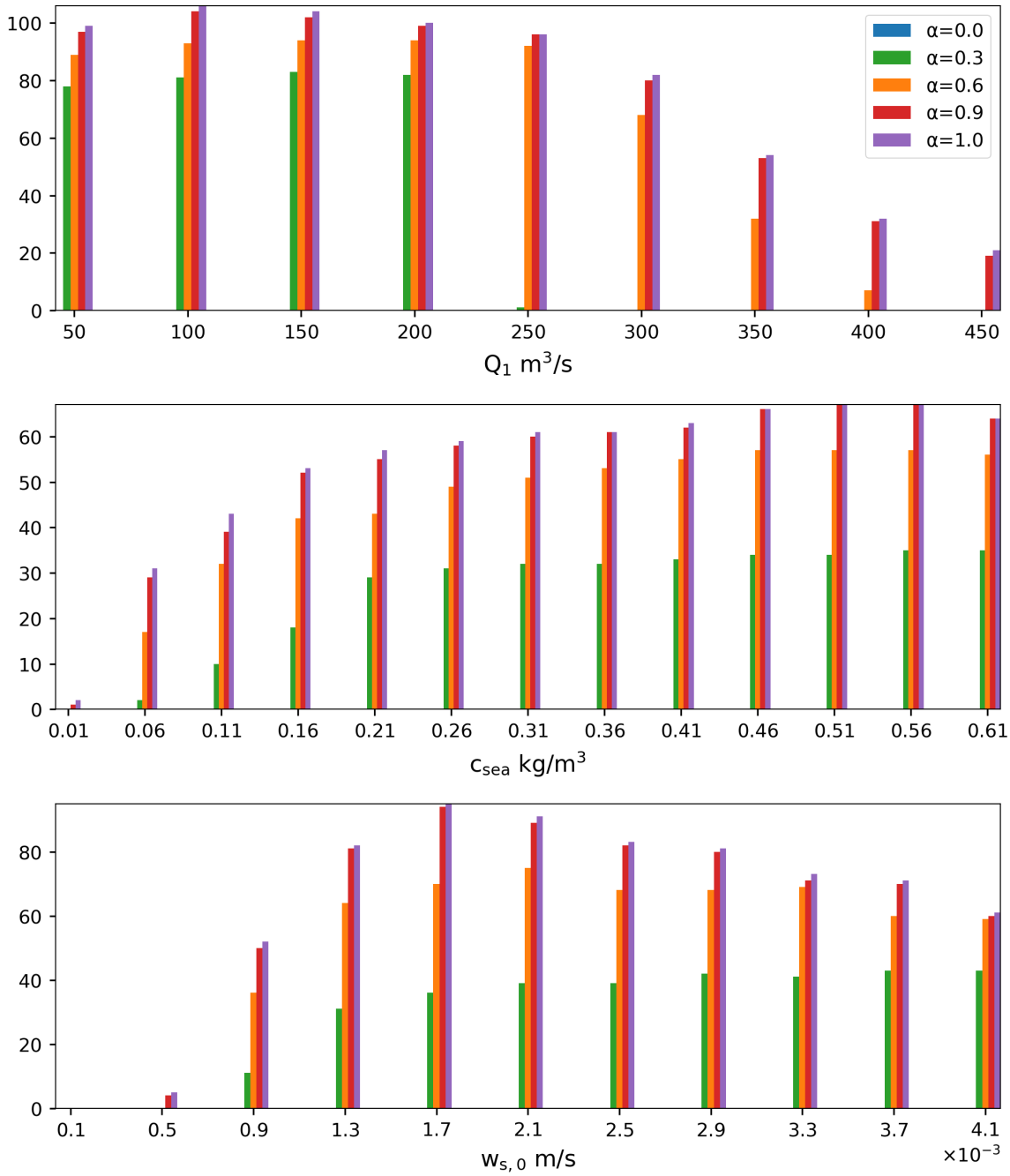

Figure 5.9: Number of simulations that have a near-bed sediment concentration larger than 5 g/l between km 25 and 40, sorted for 5 different values of alpha and 3 different input parameters.

6

DISCUSSION AND CONCLUSIONS

6.1. DISCUSSION

The goal of this research was to investigate the role deepening played in the observed regime shift to high sediment concentrations in the Loire estuary. Drawing robust conclusions despite the large range of uncertainty and variability in reported observations and model parameters asked for an innovative approach. Extensive sensitivity studies are used to map the influence of these uncertainties on the sediment dynamics on a global scale in a qualitative way (i.e. location and the order of magnitude of the ETM). The large amount of simulations that needed to be performed and the interest in processes on a global scale justify the choice for an idealised model. Nevertheless, idealised models are characterised by a high degree of simplification with accompanying inadequacies. This section discusses the robustness of the results by considering the effects of several of these simplifications.

6.1.1. SIMPLIFIED GEOMETRY

The first simplification that is considered is the use of a simplified geometry. In reality, the Loire is a river with multiple bends that turns into an estuary (while approaching the sea) which includes a main channel, shallow zones and several intertidal areas. In this research, the Loire has been schematised as a straight channel with a rectangular cross-section of which the depth and width may smoothly vary in along-channel direction. As a consequence, bend-induced spiral motions and small-scale turbulence near sharp transitions in the bottom and/or width are not accounted for. The model formally averages over small scales, parametrizing the effect on the small scales (e.g. the horizontal eddy diffusivity). So although such processes certainly play a role on a local scale, the scaling approach used to derive the governing equations as presented in chapter 2 only holds on a global scale. Hence, the results can be used to describe global patterns in a qualitative way, but a more detailed modelling approach is desired when detailed local processes are of interest.

Furthermore, a width-averaged approach has been applied, i.e. processes and variations in the lateral direction are not considered. Since water levels are reproduced well, one might think, based on continuity, that velocities should be reproduced too. However, though not presented in the results, a comparison of reported velocity observations (probably taken in the main channel) and model results showed an underestimation of the velocities in the model. This is likely caused by the width-averaging of the flow, resulting in an underestimation of the flow velocities in the main channel and an overestimation of the flow velocity in the shallow parts. Consequentially, flow induced shear-stresses and turbulence (both measures of local resuspension) are likely to be underestimated in the main channel and overestimated in the shallow parts as well. A more precise description of the geometry may result in a better reproduction of local velocities (e.g. Friedrichs and Hamrick (1996)), and a different distribution of the sediment in the lateral direction. Using a self-developed semi-idealised 3D model for estuarine turbidity, Kumar et al. (2017) showed that easy erodible sediment tends to accumulate at the sides as a consequence of lateral processes. Nevertheless, the highest concentrations of suspended sediment were still found in the middle of the channel and the location of the ETM hardly changed. On the one hand, since we have seen that sediment concentrations are important for the tipping point of the regime shift, we could argue that a better representation might provide more insight.

On the other hand, the large amount of experiments treated in this research all show, despite the large range of uncertainty, the same global tendency towards a more importing system as a consequence of deepening. Therefore, to predict the exact tipping point, a more detailed approach might be desired, but for investigating the potential role of deepening, I would argue that the approach used in this research already suffices.

6.1.2. SIMPLIFIED SALINITY

Within this thesis, a subtidally constant, well-mixed salinity field is assumed. Observations by the SYVEL network (GIP (2011b)) confirm that the Loire estuary is well-mixed during spring tide and low river discharge. During neap tide conditions however, already some stratification can be observed. This stratification becomes much stronger for high river discharges. Salinity induced stratification could result in damping of turbulence in a similar way as sediment induced stratification, which was found the be of crucial importance for the system to turn hyperturbid. From this, we could argue that if salinity stratification contributes to the turbulence damping, a regime shift possible could be found in an earlier stage for default settings. However, this hypothesis should be investigated in further research.

Furthermore, while investigating the effects of deepening, the prescribed salinity field remained constant. However, although there is hardly any quantitative data about historical salinity, multiple sources (e.g. CSEEL (1984); Paape (1994); GIP (2017)) qualitatively describe enhanced saline intrusion over the 20th century. Using the present-day salinity field for the historical depths probably results in an overestimation of the sediment import due to the baroclinic contribution, hence an overestimation of the historical likelihood of hyperturbidity. Therefore, it is safe to say that this simplification does not affect the main conclusions of this research.

6.1.3. TRANSITION TO HYPERTURBIDITY

The set of equations as presented in chapter 2 holds for the low concentration regime and the transition towards the hyperturbid regime. However, certain assumptions become debatable once the system turns to the state with high sediment concentrations. For example, we neglected the influence of suspended sediment on the density, whereas the contribution to the density of salinity and hyperturbid sediment concentrations are approximately of the same order. Besides that, iFlow lacks some essential processes to capture the sediment dynamics within the ETM in the hyperturbid regime (Dijkstra et al., 2019c). Therefore, conclusions should be restricted to the low-concentrations regime and the transition towards the hyperturbid regime, whereas the results within the hyperturbid conditions should be considered with care.

6.1.4. DYNAMIC FORCING

In this research, the sediment concentration equilibrium condition is modelled with a constant tidal forcing and constant river discharge. In reality however, the river discharge varies on a seasonal timescale and the tide shows a spring-neap variation on a bi-monthly timescale. Though not considered in this research, iFlow has been extended to include such dynamical forcing on a seasonal timescale (Brouwer et al., 2018) and to include spring-neap tidal variations (Bouwman, 2019).

Considering spring tidal conditions, we have seen that although the estuary tends to form an inland ETM, sediment concentrations in the Loire estuary are limited by supply of sediments from the sea. We have also seen that in the present day situation, the estuary tends to import sediment during neap tidal conditions. By including a spring-neap tidal variation of the tidal forcing, we could argue that sediments are imported during neap tide, and resuspended during spring tide, resulting in the high sediment concentrations near the surface as observed during spring tide. Although strong indications are found for this hypothesis, it still needs to be further investigated.

6.2. CONCLUSIONS

According to the hypothesis of Winterwerp and Wang (2013), channel deepening in the Loire estuary would have led to a regime shift towards a hyperturbid state in the Loire estuary. Three research questions were posed in chapter 1, together providing a systematic approach of understanding the mechanisms in the Loire estuary, and verifying the hypothesis of Winterwerp and Wang (2013). The answers to these research questions are discussed below.

"What are the governing processes regarding sediment dynamics in the current state of the Loire estuary?"
In chapter 4, we have identified the governing processes in the Loire estuary using an iFlow model. By defining a sufficiently high erosion parameter, the model is capable of qualitatively reproducing observed water levels and sediment concentrations for neap tidal conditions. The contributions of different physical processes varied significantly for spring and neap tide, as well as for high and low sediment concentrations.

- At first, we consider the regime with low concentrations of suspended sediment. The contributions to the transport capacity forced by the tidal asymmetry induced by the *river* and *external* M_4 *tide* are important exporting and importing contributions respectively. In the first 10 km of the estuary, they balance each other, which makes the transport contribution due to *spatial settling lag* governing the total transport capacity. Consequentially, an ETM is found around km 5 for both spring and neap tide. From 10 km onwards, the exporting river contribution dominates the import due to the external M_4 tide for both spring and neap tide. This results in an exporting transport capacity in the rest of the estuary for neap tidal conditions. The total transport capacity for spring tidal conditions however is governed by the contribution due to spatial settling lag. As a consequence, an ETM is found around km 35, but also a strong exporting capacity is found in the first 20 km of the estuary. From km 50 onwards, the exporting *river* contribution is dominating for both spring and neap tide.
- Secondly, the hyperturbid state of the estuary is considered. As a consequence of the sediment induced turbulence damping, the contributions due to a *baroclinic* pressure gradient and the *ext.* M_4 *tide* are amplified, whereas the other contributions remained more or less equal for neap tide. Consequentially, the total transport capacity shows an importing tendency in the first 35 km resulting in an ETM around km 35. A similar amplification of the *baroclinic* and *ext.* M_4 *tide* is found for spring tide, but in contrast to neap tide, the other contributions are amplified as well. Consequentially, for spring tide similar processes are found to govern the distribution of sediments with and without high concentrations of suspended sediment. Whether hyperturbid conditions are found depends on the amount of easy erodible sediment near the ETM at km 35, which is probably governed by the import during neap tidal conditions (topic for further research, see subsection 6.1.4).

"How are these processes affected by deepening in the Loire?"
The effects of deepening on the physical processes are investigated using a sensitivity study in which only the depth is varied (see chapter 5). Regarding the transport capacity for the 1900 state, next to the *baroclinic, ext.* M_4 *tide, sediment advection* and the *river* contributions, the contributions due to the *tidal return flow* and *velocity-depth asymmetry* played a role as well. Within the first 20 km of the estuary, deepening either increased the import, reduced the export or had no effects for all specific contributions to the total transport capacity, except for the exporting contribution due to *sediment advection* which increased. In the second part of the estuary (km 20-50), deepening only decreased the import caused by *velocity-depth asymmetry*, where the effects on the other contributions either enhanced sediment import or were neutral regarding sediment import. Once the estuary turns hyperturbid, the import by the *baroclinic* and ext. M_4 tide are dominant as stated before. Although deepening sometimes locally resulted in an increased exporting contribution due to one of the physical processes, it generally resulted in enhanced sediment import or decreased sediment export.

"Can these effects be held responsible for the regime shift in the Loire estuary?"
In the previous sub-question, we concluded that, as a consequence of deepening, the transport capacity in the Loire became much more favourable for the import of sediment. In order to determine the robustness of these findings, an extensive sensitivity study is presented in section 5.3, which contained 14.157 simulations (1287 conditions for 11 bottom profiles over time) to capture the influence of uncertainties in multiple input parameters (clear-water settling velocity, river discharge and seaward sediment concentration). For bathymetrical profiles representing the 1900 state, no hyperturbid concentrations are found, whereas the likelihood to find hyperturbidity clearly increases for increasing depth, independent of the 1287 different

conditions. From this we can conclude, that the observed regime shift towards high sediment concentrations, would not have happened without the deepening of the Loire estuary.

"Does the hypothesis of Winterwerp and Wang (2013) hold for the Loire estuary?"
According to the hypothesis of Winterwerp and Wang (2013), deepening of the estuary reduces river flushing and enhances tidal amplification which could initiate a positive feedback loop. Although a slight dampening of the river flushing is observed for the hyperturbid state of the Loire estuary, river flushing remained more or less equal for different depth profiles as long as the sediment concentrations remained low. Hence, reduced river flushing played a minor role in the regime shift towards a hyperturbid state. Nevertheless, deepening clearly resulted in amplification of the tide. An amplification of the M_4 tidal velocities enhanced sediment import, due to an increased tidal asymmetry. The combination of the increased sediment concentrations and the sediment induced turbulence damping results in a positive feedback loop, which further enhances the sediment import. Eventually, hyperturbid conditions are found. This confirms the existence of a positive feedback loop as suggested by Winterwerp and Wang (2013).

REFERENCES

Abril, G., Etcheber, H., Delille, B., and Borges, M. F. A. V. (2003). Carbonate dissolution in the turbid and eutrophic loire estuary. *Marine Ecology Progress Series*, 259:129–138.

Adams, J., Bate, G., and O'Callaghan, M. (1999). *Chapter 5: Estuarine Primary producers. In: Estuaries of South Africa*, pages 91–119.

Artelia (2013). Atlas des submersions marines de l'estuaire de la Loire - Analyse Hydrogeomorphologique. Technical Report 4-53-0990, Direction départementale des territoires et de la mer (DDTM).

Berthois, L. (1954). La sédimentation en loire en grande marée de vive eau. *Comptes Rendus hebdomadaires des séances de l'Académie des Sciences*, 240:106–108.

Berthois, L. (1955a). Evalution du tonnage des sables apportés en suspension pendant les crues de la loire en 1955. *Comptes Rendus hebdomadaires des séances de l'Académie des Sciences*, 241:1605–1607.

Berthois, L. (1955b). Sédimentation dans l'estuaire de la Loire en période hivernale. *Comptes Rendus hebdomadaires des séances de l'Académie des Sciences*, 236:1984.

Berthois, L. (1958). Les modalités d'envasement dans l'estuaire de la Loire (inflexion de belle-île). *Comptes Rendus hebdomadaires des séances de l'Académie des Sciences*, 246:141–142.

Berthois, L. and Barbier, M. (1953). La sedimentation en Loire maritime en période d'étiage. *Comptes Rendus hebdomadaires des s/éances de l'Acad/émie des Sciences*, 236:1984–1986.

Bosboom, J. and Stive, M. J. (2012). *Coastal dynamics I: lectures notes CIE4305*.

Bouwman, D. (2019). The influence of spring-neap cycles on sediment trapping in tide-dominated estuaries. Master's thesis, Delft University of Technology.

Briere, C., Giardino, A., , and Winterwerp, J. (2011). Analyse de la morphologie du chenal de Nantes et étude de sa restauration : phase 1: evolutions passées et fonctionnement actuel. Technical Report 1201695, Deltares.

Brouwer, R. L., Schramkowski, G. P., Dijkstra, Y. M., and Schuttelaars, H. M. (2018). Time evolution of estuarine turbidity maxima in well-mixed, tidally dominated estuaries: the role of availability-and erosion-limited conditions. *Journal of Physical Oceanography*, 48(8):1629–1650.

Bruens, A. (2003). *Entraining mud suspensions*. Delft University of Technology, Faculty of Civil Engineering and Geosciences.

Burchard, H. and Baumert, H. (1998). The formation of estuarine turbidity maxima due to density effects in the salt wedge. a hydrodynamic process study. *Journal of Physical Oceanography*, 28(2):309–321.

Burchard, H. and Schuttelaars, H. (2012). Analysis of tidal straining as driver for estuarine circulation in well-mixed estuaries. *Journal of Physical Oceanography*, 42:261–271.

Burchard, H., Schuttelaars, H. M., and Ralston, D. K. (2018). Sediment trapping in estuaries. *Annual review of marine science*, 10:371–395.

Charrier, P. (2000). Entre Anjou et Pays Nantais, interventions humaines et transformations hydro-morphologiques en Loire armoricaine (1750-1960)//Between Anjou and Pays Nantais, human interventions and hydro-morphology of the Armorican Loire (1750-1960). In *Annales de géographie*, volume 109, pages 115–131. Société de géographie.

Chernetsky, A. S., Schuttelaars, H. M., and Talke, S. A. (2010). The effect of tidal asymmetry and temporal settling lag on sediment trapping in tidal estuaries. *Ocean Dynamics*, 60(5):1219–1241.

Cloern, J. E., Foster, S., and Kleckner, A. (2014). Phytoplankton primary production in the world's estuarine-coastal ecosystems. *Biogeosciences*, 11(9):2477–2501.

CSEEL (1984). Rapport final du comité scientifique pour l'environnement de l'estuaire de la loire, rapports scientifiques et techniques, n° 55, publications du centre national pour l'exploitation des océans, brest, france.

Dijksta, Y. (2017). *iFlow modelling framework. User manual & technical description.*

Dijkstra, Y. M. (2019). *Regime shifts in sediment concentrations in tide-dominated estuaries.* PhD thesis, Delft University of Technology.

Dijkstra, Y. M., Brouwer, R. L., Schuttelaars, H. M., and Schramkowski, G. P. (2017). The iflow modelling framework v2. 4: a modular idealized process-based model for flow and transport in estuaries. *Geoscientific Model Development*, 10(7):2691–2713.

Dijkstra, Y. M., Schuttelaars, H. M., and Schramkowski, G. P. (2019a). Can the scheldt river estuary become hyperturbid? *Ocean Dynamics*, 69(7):809–827.

Dijkstra, Y. M., Schuttelaars, H. M., and Schramkowski, G. P. (2019b). A regime shift from low to high sediment concentrations in a tide-dominated estuary. *Geophysical Research Letters*, 46(8):4338–4345.

Dijkstra, Y. M., Schuttelaars, H. M., Schramkowski, G. P., and Brouwer, R. L. (2019c). Modeling the transition to high sediment concentrations as a response to channel deepening in the ems river estuary. *Journal of Geophysical Research: Oceans*, 124(3):1578–1594.

Dijkstra, Y. M., Schuttelaars, H. M., and Winterwerp, J. C. (2018). The hyperturbid state of the water column in estuaries and rivers: the importance of hindered settling. *Ocean Dynamics*, 68(3):377–389.

DREAL (2019). La Loire à Montjean-sur-Loire - Synthese: données hydrologiques de synthèse (1863-2019). http://www.hydro.eaufrance.fr/.

Etcheber, H., Taillez, A., Abril, G., Garnier, J., Servais, P., Moatar, F., and Commarieu, M.-V. (2007). Particulate organic carbon in the estuarine turbidity maxima of the gironde, loire and seine estuaries: origin and lability. *Hydrobiologia*, 588(1):245–259.

Fairbridge, R. (1980). The estuary: its definition and geodynamic cycle. *Chemistry and biochemistry of estuaries*.

Friedrichs, C. T. and Aubrey, D. G. (1988). Non-linear tidal distortion in shallow well-mixed estuaries: a synthesis. *Estuarine, Coastal and Shelf Science*, 27(5):521–545.

Friedrichs, C. T. and Hamrick, J. M. (1996). Effects of channel geometry on cross-sectional variations in along-channel velocity in partially stratified estuaries. *Coastal and Estuarine Studies*, pages 283–300.

Gallenne, B. (1974a). *Les accumulations turbides de l'estuaire de la Loire. Etude de la" crème de vase"*. PhD thesis, University of Nantes.

Gallenne, B. (1974b). Study of fine material in suspension in the estuary of the loire and its dynamic grading. *Estuarine and Coastal Marine Science*, 2(3):261–272.

Gasquet, H. and Wootton, A. (1997). Variable-frequency complex demodulation technique for extracting amplitude and phase information. *Review of scientific instruments*, 68(1):1111–1114.

Gernez, P., Lafon, V., Lerouxel, A., Curti, C., Lubac, B., Cerisier, S., and Barillé, L. (2015). Toward sentinel-2 high resolution remote sensing of suspended particulate matter in very turbid waters: Spot4 (take5) experiment in the loire and gironde estuaries. *Remote Sensing*, 7(8):9507–9528.

Geyer, W. R. (1993). The importance of suppression of turbulence by stratification on the estuarine turbidity maximum. *Estuaries*, 16(1):113–125.

GIP (2002a). Cahier Indicateur n1 - Géometrie des fonds. Available online: http://www.loire-estuaire.org/upload/iedit/1/pj/51842_2856_L1E5CMB_206106_L1E5.pdf. In French.

GIP (2002b). Cahier Indicateur n1 - Les lignes d'eau du fleuve. Available online: http://www.loire-estuaire.org/upload/iedit/1/pj/43680_2850_CMB_206106_L1C2.pdf In French.

GIP (2004). Les niveaux d'eau de la Maine à la Mer. Available online: http://www.loire-estuaire.org/upload/iedit/1/pj/43662_1922_panneau_NiveauxEaux.pdf. In French.

GIP (2011a). Equilibre du lit de la Loire estuarienne - Lancement d'un programma d'actions 2012-2020. Available online: http://www.loire-estuaire.org/upload/espace/1/pj/44124_2657_dossier_lettre14.pdf. In French.

GIP (2011b). SYVEL - Bulletin n2 du 22 décembre 2011. Available online: http://www.loire-estuaire.org/accueil/nos_ressources/publications. In French.

GIP (2013). Les amplitudes de l'onde de marée. Available online: http://www.loire-estuaire.org/upload/iedit/1/pj/44138_4069_l1a1_onde_maree_maj.pdf. In French. Figure L1 A1 - 1.

GIP (2014a). Atlas morpho-bathymétrique la Loire de Nantes à Saint-Nazaire. Available online: http://www.loire-estuaire.org/accueil/nos_ressources/publications. In French.

GIP (2014b). Atlas morpho-bathymétrique la Loire des Ponts-de-Cé à Nantes. Available online: http://www.loire-estuaire.org/accueil/nos_ressources/publications. In French.

GIP (2017). Les programmes, études et modélisations en aval de Nantes - Synthèse. PowerPoint.

Guilcher, A. (1988). Léopold berthois (1900-1986). une carrière exemplaire au service de la mer, ses côtes, ses fonds et ses sédiments. *Norois*, 138(1):191–200.

Guo, L., Van der Wegen, M., Roelvink, J., and He, Q. (2014). The role of river flow and tidal asymmetry on 1-d estuarine morphodynamics. *Journal of Geophysical Research: Earth Surface*, 119(11):2315–2334.

Hamm, L. and Walther, R. (2009). Morphodynamic coupling of bottom roughness and fluid mud for modelling tidal propagation in the loire estuary (france). In *Coastal Engineering 2008: (In 5 Volumes)*, pages 2832–2841. World Scientific.

Hubiche, J.-L., editor (2002). *La marée dynamicque - Les amplitudes de l'onde de marée*, volume 1. Loire Estuaire Cellule de Mesures et de Bilans.

Jalón-Rojas, I., Schmidt, S., Sottolichio, A., and Bertier, C. (2016). Tracking the turbidity maximum zone in the Loire estuary (France) based on a long-term, high-resolution and high-frequency monitoring network. *Continental Shelf Research*, 117.

Joint, I. and Pomroy, A. (1981). Primary production in a turbid estuary. *Estuarine, Coastal and Shelf Science*, 13(3):303–316.

Kandiah, A. (1976). Fundamental aspects of surface erosion of cohesive soils.

Klaassen, K. (2015). Life expectation of wooden foundations—a non-destructive approach. In *Proceedings of the International Symposium Non-Destructive Testing in Civil Engineering (NDT-CE), Berlin, Germany*.

Kumar, M., Schuttelaars, H. M., and Roos, P. C. (2017). Three-dimensional semi-idealized model for estuarine turbidity maxima in tidally dominated estuaries. *Ocean Modelling*, 113:1–21.

Le Hir, P. and Karlikow, N. (1992). Sediment transport modelling in a macrotidal estuary: do we need to account for consolidation processes? *Coastal Engineering Proceedings*, 1(23).

Lefort, P. (2010). La Loire des Ponts de Cé à Nantes - expertise hydro-sédimentaire. Technical report, GIP Loire Estuaire.

Longuet-Higgins, M. (1969). On the transport of mass by time-varying ocean currents. In *Deep Sea Research and Oceanographic Abstracts*, volume 16, pages 431–447. Elsevier.

Manickam, S. and Barbaroux, L. (1987). Variations in the surface texture of suspended quartz grains in the loire river: an sem study. *Sedimentology*, 34(3):495–510.

Maquet, J. (1974). Aménagement de l'estuaire de la Loire. *La Houille Blanche*, (1/2):79–89.

Mays, L. W. (2008). A very brief history of hydraulic technology during antiquity. *Environmental Fluid Mechanics*, 8(5-6):471–484.

Migniot, C. (1993). Bilan de l'hydrologie et de l'hydrosédimentaire de l'estuaire de la Loire au cours des deux dernières décénnies. *Association pour la Protection de l'Environnement de l'Estuaire de la Loire, Port Autonome de Nantes-St Nazaire, Nantes*.

Millennium Ecosystem Assessment (2005). *Ecosystems and human well-being*, volume 5. Island press Washington, DC:.

Moatar, F. and Dupont, N. (2016). *La Loire fluviale et estuarienne - Un milieu en évolution*. Éditions Quae, RD 10 - 78026 Versailles Cedex.

Munk, W. and Anderson, E. (1948). Notes on a theory of the thermocline. *Journal of Marine Research*, 7.

Murray, A. B. (2003). Contrasting the goals, strategies, and predictions associated with simplified numerical models and detailed simulations. *Geophysical Monograph-American Geophysical Union*, 135:151–168.

Normant, C. L. (2000). Three-dimensional modelling of cohesive sediment transport in the loire estuary. *Hydrological processes*, 14(13):2231–2243.

O'Higgins, T., Ferraro, S., Dantin, D., Jordan, S., and Chintala, M. (2010). Habitat scale mapping of fisheries ecosystem service values in estuaries. *Ecology and Society*, 15(4).

Paape (1994). Etude hydrologique de l'estuaire de la Loire. Technical Report T1109/Z581, WL | Delft Hydraulics.

Postma, H. (1954). Hydrography of the dutch wadden sea. *Arch. Neerl. Zool*, 10(4):405–511.

Postma, H. and Kalle, K. (1955). Die entstehung von trübungszonen im unterlauf der flüsse, speziell im hinblick auf die verhältnisse in der unterelbe. *Deutsche Hydrografische Zeitschrift*, 8(4):137–144.

Pritchard, D. and Hogg, A. J. (2003). Models of settling lag in coastal and estuarine settings. In *Proceedings of the 3rd IAHR Symposium on River, Coastal and Estuarine Morphodynamics*, pages 29–39.

Pritchard, D. W. (1967). What is an estuary: physical viewpoint. American Association for the Advancement of Science.

Relexans, J.-C., Meybeck, M., Billen, G., Brugeaille, M., Etcheber, H., and Somville, M. (1988). Algal and microbial processes involved in particulate organic matter dynamics in the loire estuary. *Estuarine, Coastal and Shelf Science*, 27(6):625–644.

Richardson, J. and Zaki, W. (1954). The sedimentation of a suspension of uniform spheres under conditions of viscous flow. *Chemical Engineering Science*, 3(2):65–73.

Rincé, Y., Martin-Jézéquel, V., and Ravail, B. (1989). Ecological observations on plankton of the loire estuary (france). *Cahiers de biologie marine*, 30(2):201–216.

Ross, D. (1995). *Introduction to Oceanography*. Harper Collins College Publishers.

Rouse, H. (1938). Nomogram for the settling velocity of spheres.

Saliot, A., Lorre, A., Marty, J.-C., Scribe, P., Tronczynski, J., Meybeck, M., Dessery, S., Marchand, M., Caprais, J.-C., Cauwet, G., et al. (1984). Biogéochimie de la matière organique en milieu estuarien: stratégies d'échantillonnage et de recherche élaborées en Loire (France). *Oceanologica acta*, 7(2):191–207.

SAR (1993). Historique et analyse de l'évolution du cours de la Loire entre Nantes et Angers. Technical Report CAD 354, Sabliers Angevins Reunis.

Savenije, H. H. G. (1992). *Rapid assessment technique for salt intrusion in alluvial estuaries*. PhD thesis, Delft University of Technology.

Scheffer, M., Carpenter, S., Foley, J. A., Folke, C., and Walker, B. (2001). Catastrophic shifts in ecosystems. *Nature*, 413(6856):591.

Schuttelaars, H. M., de Jonge, V. N., and Chernetsky, A. (2013). Improving the predictive power when modelling physical effects of human interventions in estuarine systems. *Ocean & coastal management*, 79:70–82.

Simpson, J. H., Brown, J., Matthews, J., and Allen, G. (1990). Tidal straining, density currents, and stirring in the control of estuarine stratification. *Estuaries*, 13(2):125–132.

Sogreah (2006). Mission d'étude, d'approfondissement et d'évaluation de scénarios visant à améliorer le fonctionnement hydro seédimentaire de l'estuaire de la Loire. expertise et connaisance du système estuarien. Tome 1 - Analyse historique. Technical Report 1 71 1457 R2, Sogreah.

Sogreah (2010). Développement et exploitation d'un modèle hydrosédimentaire en trois dimensions sur l'estuaire de la Loire. Technical Report 1 71 1822 R10, Sogreah.

Stokes, G. (1847). On the theory of oscillatory waves. transaction of the cambridge society 8. 441-455. reprinted in stokes, gg (1880). mathematical and physical papers.

Talke, S. A., de Swart, H. E., and De Jonge, V. (2009a). An idealized model and systematic process study of oxygen depletion in highly turbid estuaries. *Estuaries and coasts*, 32(4):602–620.

Talke, S. A., de Swart, H. E., and Schuttelaars, H. (2009b). Feedback between residual circulations and sediment distribution in highly turbid estuaries: an analytical model. *Continental Shelf Research*, 29(1):119–135.

Van Maren, D., Van Kessel, T., Cronin, K., and Sittoni, L. (2015). The impact of channel deepening and dredging on estuarine sediment concentration. *Continental Shelf Research*, 95:1–14.

van Maren, D. S., Winterwerp, J. C., and Vroom, J. (2015). Fine sediment transport into the hyper-turbid lower ems river: the role of channel deepening and sediment-induced drag reduction. *Ocean Dynamics*, 65(4):589–605.

Walther, R., Schaguene, J., Hamm, L., and David, E. (2012). Coupled 3d modeling of turbidity maximum dynamics in the loire estuary, france. *Coastal Engineering Proceedings*, 1(33):22.

Wang, X. and Andutta, F. (2013). Sediment transport dynamics in ports, estuaries and other coastal environments. In *Sediment Transport Processes and Their Modelling Applications*. IntechOpen.

Wang, Z., Jeuken, C., and De Vriend, H. (1999). Tidal asymmetry and residual sediment transport in estuaries. *Delft Hydraulics report Z2749*.

Wang, Z., Van Maren, D., Ding, P., Yang, S., Van Prooijen, B., De Vet, P., Winterwerp, J., De Vriend, H., Stive, M., and He, Q. (2015). Human impacts on morphodynamic thresholds in estuarine systems. *Continental Shelf Research*, 111:174–183.

Wilson, M. A., Costanza, R., Boumans, R., and Liu, S. (2005). Integrated assessment and valuation of ecosystem goods and services provided by coastal systems. *The intertidal ecosystem: the value of Ireland's shores. Royal Irish Academy, Dublin, Ireland*, pages 1–24.

Winterwerp, J. (2001). Stratification effects by cohesive and noncohesive sediment (paper 2000jc000435). *JOURNAL OF GEOPHYSICAL RESEARCH-ALL SERIES-*, 106(10; SECT 3):22–559.

Winterwerp, J. C. (2011). Fine sediment transport by tidal asymmetry in the high-concentrated ems river: indications for a regime shift in response to channel deepening. *Ocean Dynamics*, 61(2):203–215.

Winterwerp, J. C. and Van Kesteren, W. G. (2004). *Introduction to the physics of cohesive sediment dynamics in the marine environment*, volume 56. Elsevier.

Winterwerp, J. C. and Wang, Z. B. (2013). Man-induced regime shifts in small estuaries - 1: theory. *Ocean Dynamics*, 63:1279 – 1292.

Wofsy, S. (1983). A simple model to predict extinction coefficients and phytoplankton biomass in eutrophic waters 1. *Limnology and Oceanography*, 28(6):1144–1155.

Yoshiyama, K. and Sharp, J. H. (2006). Phytoplankton response to nutrient enrichment in an urbanized estuary: Apparent inhibition of primary production by overeutrophication. *Limnology and Oceanography*, 51(1part2):424–434.

A

HYDRODYNAMICS

This model will be used to evaluate the hydrodynamics within the Loire estuary. The governing equations are already presented in chapter 2. At first, a short derivation for the relative phase difference between the M_2 and M_4 water level elevations is discussed. The remainder of this appendix elaborates on the perturbation approach. Firstly, the scaling of the equations is presented. Secondly, leading-order and first-order equations are derived. And finally, derivations regarding the typical forcing of the sediment dynamics are discussed. This appendix provides additional information to chapter 2, and should not be read on its own.

A.1. EQUATIONS

A.1.1. HORIZONTAL BOUNDARY CONDITIONS

The relative phase difference can be expressed in terms of the distinct phases of the M_2 and M_4 components. At first, the observed tidal motion at the seaward boundary is considered as the sum of a semi-diurnal and a quarter-diurnal signal, each with their own phases ϕ:

$$\zeta = \zeta_{M2} + \zeta_{M4} \tag{A.1}$$

with:

$$\zeta_{M2} = A_{M2}\cos(\sigma t - \varphi_{M2}) = A_{M2}\cdot e^{i\sigma t - \frac{\varphi_{M2}}{\sigma}} \tag{A.2}$$

$$\zeta_{M4} = A_{M4}\cos(2\sigma t - \varphi_{M4}) = A_{M4}\cdot e^{2i\sigma t - \frac{\varphi_{M4}}{2\sigma}} \tag{A.3}$$

In order to achieve a zero phase of the semi-diurnal signal at the seaward boundary, the M2 signal should be shifted with φ_{M2}/σ (multiplying with $e^{\frac{\varphi_{M2}}{\sigma}}$). However, to keep the result of Equation A.1 equal, the M4 signal should be shifted equally:

$$\zeta_{M2} \rightarrow A_{M2}\cdot e^{i\sigma t - \frac{\varphi_{M2}}{\sigma}}\cdot e^{\frac{\varphi_{M2}}{\sigma}} = A_{M2}\cdot e^{i\sigma t} \tag{A.4}$$

$$\zeta_{M4} \rightarrow A_{M4}\cdot e^{2i\sigma t - \frac{\varphi_{M4}}{2\sigma}}\cdot e^{\frac{\varphi_{M2}}{\sigma}} = A_{M4}\cdot e^{2i\sigma t} e^{-\frac{\varphi_{M4}}{2\sigma}+\frac{\varphi_{M2}}{\sigma}} \tag{A.5}$$

Substituting Equation A.4 and Equation A.5 into equation Equation A.1 and rewriting in the traditional cosine form gives us:

$$\zeta = A_{M2}\cos(\sigma t) + A_{M4}\cos(2\sigma t - (\varphi_{M4} - 2\varphi_{M2})) \tag{A.6}$$

$$\rightarrow \phi = \varphi_{M4} - 2\varphi_{M2} \tag{A.7}$$

A

A.2. SCALING

A.2.1. OVERVIEW OF PARAMETERS

A mathematical scaling analysis, a perturbation approach, will be used to identify the importance of the individual terms in the equations. For this purpose, the equations need to be transformed to a dimensionless system which can be done using scaling arguments. Typical scales (of parameters present in the equations) are presented in Table A.1

Table A.1: Typical scales of individual parameters

Scale		Dimensionless quantity
T_{M2}	M_2 tidal period	$t = T_{M2}\,t^*$
A_{M2}	M_2 tidal amplitude at the seaward side	$\zeta = A_{M2}\zeta^*$
H_0	Average depth at seaward side	$z = H_0 z^*$ and $R = A_{M2}R^*$
L_{tide}	Tidal wave length	$x = L_{tide}x^*$ for u_x, w_x, ζ_x
L_{conv}	Convergence length	$x = L_{conv}x^*$ for H_x, B_x
$\mathscr{R}_x$	Typical density gradient	$\rho_x = \mathscr{R}_x \rho^*_{x^*}$

To get a feeling about the magnitude of the different parameters, a list with typical values for the Loire estuary is presented in Table A.2.

Table A.2: Typical values of physical parameters in the Loire Estuary

Parameter	Typical value	Typical Order
T_{M2}	44712 s	$\mathcal{O}(10^4)$
$\sigma_{M2} = \frac{2\pi}{T_{M2}}$	$(1/44712)$ s^{-1}	$\mathcal{O}(10^{-4})$
L_{tide}	100km = 10^5m	$\mathcal{O}(10^5)$
A_{M2}	1 m	$\mathcal{O}(1)$
H_0	10-20 m	$\mathcal{O}(10)$
g	9.81 m/s^2	$\mathcal{O}(10)$

With these typical scales, scales of other parameters can be derived. This is done below for the horizontal and vertical velocities (U and W respectively). At first, the depth averaged continuity equation (Equation 2.7) is made dimensionless:

$$\frac{A_{M2}}{T}\underbrace{\zeta^*_{t^*}}_{=1} + \frac{(H_0 + A_{M2})U}{L_{tide}}\underbrace{\frac{1}{B^*}\left(B^*\int_{-z^*}^{R^*+\zeta^*} u^*\,dz^*\right)_{x^*}}_{=1} = 0 \tag{A.8}$$

So:

$$\frac{A_{M2}}{T} \sim \frac{(H_0 + A_{M2})U}{L_{tide}} \tag{A.9}$$

$$\rightarrow U \sim \frac{A_{M2}L}{T(H_0 + A_{M2})} \tag{A.10}$$

Deriving an expression for W using the continuity equation Equation 2.2:

$$w_z + \frac{1}{B}(Bu)_x = 0 \tag{A.11}$$

$$\frac{W}{H_0}w^*_{z^*} + \frac{BU}{BL_{tide}}(B^*u^*)_{x^*} = 0 \tag{A.12}$$

$$\rightarrow W \sim \frac{UH}{L_{tide}} = \frac{A_{M2}H_0}{T(H_0 + A_{M2})} \tag{A.13}$$

Table A.3: Derived scales for parameters in momentum equation

Derived Scale		Dimensionless quantity
U	Typical horizontal velocity of the M_2 tide	$u = Uu^*$
W	Typical vertical velocity of the M_2 tide	$w = Ww^*$
$\mathcal{N}$	Typical eddy viscosity	$A_v = \mathcal{N}A_v^*$

Table A.4: Typical values of physical parameters in the Loire Estuary

Parameter	Typical Order
$U \sim \frac{A_{M2}L}{T(H_0+A_{M2})}$	$\mathcal{O}(1)$
$W \sim \frac{UH}{L_{tide}}$	$\mathcal{O}(10^{-4})$
$\mathcal{N}\frac{H_0^2}{T_{M2}}$	$\mathcal{O}(10^5)$

To compare the order of magnitude of different terms, the order of magnitude ϵ is defined

$$\epsilon = \frac{A_{M2}}{H_0} \ll 1 \tag{A.14}$$

Furthermore, it is assumed that the typical length scales of tidal waves and bathymetrical changes are of the same order. As a consequence, non-linear advection terms become of $\mathcal{O}(\epsilon)$, and hence all leading order terms become linear. Moreover, the horizontal density gradient is assumed to be small, resulting in a baroclinic pressure term of $\mathcal{O}(\epsilon)$. Finally, it is assumed that the horizontal diffusion term is of $\mathcal{O}(\epsilon^2)$.

A.2.2. MOMENTUM EQUATION

The next step in the perturbation approach is rewriting the equations in a dimensionless form using the dimensionless quantitities from Table A.1 and Table A.3, starting with the width-averaged momentum equation:

$$\frac{U}{T}u^*_{t^*} + \frac{UU}{L}u^*u^*_{x^*} + \frac{WU}{H}w^*u^*_{z^*} = -g\frac{A}{L}\zeta^*_{x^*} - \frac{g\mathcal{R}_x(H_0+A_{M2})}{\rho_0}\int_{-z^*}^{R+\epsilon\zeta^*}\rho^*_{x^*} + \frac{\mathcal{N}U}{H^2}(A_v^*u^*_{z^*})_{z^*} \tag{A.15}$$

Secondly, the whole equation is divided by $\frac{U}{T}$

$$u^*_{t^*} + \frac{TU}{L}u^*u^*_{x^*} + \frac{WT}{H}w^*u^*_{z^*} = -g\frac{AT}{UL}\zeta^*_{x^*} - \frac{g\mathcal{R}_x(H_0+A_{M2})T}{\rho_0 U}\int_{-z^*}^{R+\epsilon\zeta^*}\rho^*_{x^*} + \frac{\mathcal{N}T}{H^2}(A_v^*u^*_{z^*})_{z^*} \tag{A.16}$$

Substituting the expressions for U and W (presented in Equation A.10 & Equation A.13) into Equation A.16, results in:

$$\underbrace{u^*_{t^*}}_{\mathcal{O}(1)} + \underbrace{\frac{A}{H+A}}_{\mathcal{O}(\epsilon)}\underbrace{u^*u^*_{x^*}}_{\mathcal{O}(1)} + \underbrace{\frac{A}{H+A}}_{\mathcal{O}(\epsilon)}\underbrace{w^*u^*_{z^*}}_{\mathcal{O}(1)} = -\underbrace{g(H+A)\frac{T^2}{L^2}}_{\mathcal{O}(?)}\underbrace{\zeta^*_{x^*}}_{\mathcal{O}(1)} - \underbrace{\frac{g\mathcal{R}_x(H_0+A_{M2})T}{\rho_0 U}}_{\mathcal{O}(?)}\underbrace{\int_{-z^*}^{R+\epsilon\zeta^*}\rho^*_{x^*}}_{\mathcal{O}(1)} + \underbrace{\frac{\mathcal{N}T}{H^2}}_{\mathcal{O}(?)}\underbrace{(A_v^*u^*_{z^*})_{z^*}}_{\mathcal{O}(1)} \tag{A.17}$$

Further investigation of the unknown terms in Equation A.17 is presented below:

$$g(H+A)\frac{T^2}{L^2} = g(H+A)\frac{1}{\sqrt{gH}^2} \approx \frac{gH}{gH} \to \mathcal{O}(1) \tag{A.18}$$

$$\mathcal{N}[m^2/s] \sim \frac{H^2}{T} \to \frac{\mathcal{N}T}{H^2} = \mathcal{O}(1) \tag{A.19}$$

A

The last remaining term is a bit harder to estimate. For this we need to remember that the wave celerity c_E can be estimated with $c_E = \frac{L}{T_{M2}}$ as well as $c_E = \sqrt{gH_0}$. Moreover, the internal wave celerity c_I can be approximated with $c_I = c_E \cdot \frac{\mathscr{R}_x L}{\rho_0}$. With this, and replacing U by Equation A.10 and neglecting the amplitude A_{M2} with respect to the water depth H_0, the unknown term can be rewritten as:

$$\frac{\overbrace{gH_0}^{=c_E^2}\mathscr{R}_x \overbrace{T}^{=L/c_E}}{\rho_0 \underbrace{U}_{=\frac{A_{M2}L}{TH_0}}} = \frac{c_E \mathscr{R}_x \overbrace{T}^{=L/c_E}}{\rho_0}\frac{H_0}{A_{M2}} = \frac{\mathscr{R}_x L}{\rho_0}\underbrace{\frac{H_0}{A_{M2}}}_{\mathscr{O}(\epsilon^{-1})} = \frac{c_I}{U} \tag{A.20}$$

The term $\frac{c_I}{U}$ is also known as the internal Froude number and is estimated to be of order ϵ. Knowing this, an order of magnitude for the density gradient $\mathscr{R}_x$ can be estimated with

$$\frac{\mathscr{R}_x L}{\rho_0} = \mathscr{O}(\epsilon^2) \tag{A.21}$$

However, the integration boundaries in this term contain the water surface elevation ζ which is of order ϵ. The integral boundary should therefore be linearised around $\zeta = R$ by use of a Taylor expansion. This is presented below:

$$\int_{z^*}^{R^*+\epsilon\zeta^*} \rho^*_{x^*}\, d\tilde{z} = \int_{z^*}^{R^*} \rho^*_{x^*}\, d\tilde{z} + \epsilon \rho^*_{x^*}(R^*)\zeta^* + \dots \tag{A.22}$$

Now the magnitude of all the terms of the momentum equation are known, the dimensional momentum equation can be written as:

$$\underbrace{u_t}_{\mathscr{O}(1)} + \underbrace{uu_x}_{\mathscr{O}(\epsilon)} + \underbrace{wu_z}_{\mathscr{O}(\epsilon)} = -\underbrace{g(R_x+\zeta_x)}_{\mathscr{O}(1)} - \underbrace{g\int_z^R \frac{\rho_x}{\rho_0}d\tilde{z}}_{\mathscr{O}(\epsilon)} - \underbrace{g\zeta\frac{\rho_x(R)}{\rho_0}}_{\mathscr{O}(\epsilon^2)} + \underbrace{(A_v u_z)_z}_{\mathscr{O}(1)} \tag{A.23}$$

BOUNDARY CONDITIONS

The boundary conditions for the width-averaged momentum equation are presented by Equation 2.3-Equation 2.6. The dimensionless boundary conditions at the surface $\tilde{z} = R^* + \epsilon\zeta^*$, are found using again a Taylor expansion around $\tilde{z} = R^*$ for u and w:

$$w^* + \epsilon\zeta^* w^*_z = \zeta^*_{t^*} + \epsilon\left(u^* + \epsilon\zeta^* u^*_z\right)\zeta^*_{x^*} \tag{A.24}$$

$$A^*_v u^*_z + \epsilon A^*_v u^*_{z^* z^*}\zeta^* = 0 \tag{A.25}$$

Resulting in the dimensional form of the boundary conditions with the following typical order of magnitude

$$\underbrace{w}_{\mathscr{O}(1)} = \underbrace{\zeta_t}_{\mathscr{O}(1)} + \underbrace{u\zeta_x - \zeta w_z}_{\mathscr{O}(\epsilon)} + \underbrace{u_z\zeta}_{\mathscr{O}(\epsilon^2)} \tag{A.26}$$

$$\underbrace{A_v u_z}_{\mathscr{O}(1)} = -\underbrace{A_v u_{zz}\zeta}_{\mathscr{O}(\epsilon)} \tag{A.27}$$

Since the boundary equations near the bed only contain two terms, we now up front that these terms are of equal order of magnitude:

$$\underbrace{w}_{\mathscr{O}(1)} = -\underbrace{uH_x}_{\mathscr{O}(1)} \tag{A.28}$$

$$\underbrace{A_v u_z}_{\mathscr{O}(1)} = \underbrace{s_f u}_{\mathscr{O}(1)} \tag{A.29}$$

A.2.3. DEPTH AVERAGED CONTINUITY EQUATION

The dimensionless form of the depth-averaged continuity equations already has been presented in Equation A.8. To derive an expression for the typical horizontal velocity, we already used that all terms are of the same order. However, the integration boundary $\epsilon\zeta^*$ forms an exception, and should therefore again be linearised using a Taylor expansion around $\zeta = R$:

$$\int_{z^*}^{R^*+\epsilon\zeta^*} u^* d\tilde{z} = \int_{z^*}^{R^*} u^* d\tilde{z} + \epsilon\zeta^* u^*(R^*) + \ldots \tag{A.30}$$

Using this linearisation, the terms in the depth-averaged continuity equation typical scale like

$$\underbrace{\zeta_t}_{\mathcal{O}(1)} + \underbrace{\frac{1}{B}\left(B\int_{-H}^{R} u dz\right)_x}_{\mathcal{O}(1)} + \underbrace{(B\zeta u_{z=R})_x}_{\mathcal{O}(\epsilon)} = 0 \tag{A.31}$$

BOUNDARY CONDITIONS

The horizontal boundary conditions corresponding to the depth-averaged continuity equation can also be written in a dimensionless form. At first, the tidal forcing on the seaward boundary is considered (i.e. $x^* = 0$):

$$\zeta^* = \cos t^* + \frac{A_{M4}}{A_{M2}}\cos(t^* - \phi) \tag{A.32}$$

in which A_{M4}/A_{M2} is assumed to be of order ϵ, such that the terms in the seaward boundary condition typically have the following order of magnitude

$$\zeta(0,t) = \underbrace{A_{M2}\cos t}_{\mathcal{O}(1)} + \underbrace{A_{M4}\cos(t-\phi)}_{\mathcal{O}(\epsilon)} \tag{A.33}$$

The boundary condition at the landward side, $x^* = 1$, written in a dimensionless form reads

$$B^* H_0 U \int_{-H^*}^{R^*+\epsilon\zeta^*} u^* d\tilde{z} = -Q \tag{A.34}$$

Again using a Taylor expansion around $z = R^*$ to linearise the upper bound of the integral, and rewriting the equation results in

$$\int_{-H^*}^{R^*} u^* d\tilde{z} + \epsilon\zeta^* u^*_{z=R^*} = -\frac{Q}{B^* H_0 U} \tag{A.35}$$

in which can be seen that the ratio of the river discharge to the typical tidally induced horizontal discharge determines whether the river discharge is a leading-order or first-order forcing mechanism to the system. The dimensional expression with typical order of magnitudes per term becomes

$$\underbrace{\int_{-H}^{R} u dz}_{\mathcal{O}(1)} + \underbrace{\zeta u_{z=R}}_{\mathcal{O}(\epsilon)} = -\underbrace{\frac{Q}{B}}_{\mathcal{O}(1)\text{ or }\mathcal{O}(\epsilon)} \tag{A.36}$$

A.3. ORDERING

The solutions u, w and ζ are written as a power series of the small parameter ϵ

$$\begin{aligned} u &= u^0 + u^1 + u^2 + \ldots \\ w &= w^0 + w^1 + w^2 + \ldots \\ \zeta &= \zeta^0 + \zeta^1 + \zeta^2 + \ldots \end{aligned}$$

in which u^0, w^0 and ζ^0 are of $\mathcal{O}(1)$, u^1, w^1 and ζ^1 of $\mathcal{O}(\epsilon)$ and so on. Additionally, partial slip parameter s_f, eddy viscosity A_v and the forcing by the tide A and river discharge Q are written as similar series. By substituting these expressions into the momentum equation (Equation A.23), a system of equations is found in leading order

A

$$\mathcal{O}(1): u_t^0 = -g(R_x + \zeta_x^0) + (A_v u_z^0)_z \tag{A.37}$$

with boundary conditions

$$A_v^0 u_z^0 = 0 \qquad \text{at } z = R \tag{A.38}$$
$$A_v^0 u_z^0 = s_f^0 u^0 \qquad \text{at } z = -H \tag{A.39}$$

And first order:

$$\mathcal{O}(\epsilon): u_t^1 + u^0 u_x^0 + w^0 w_z^0 = -g\zeta_x^1 - g\int_z^0 \frac{\rho_x}{\rho_0} dz + (A_v u_z^1)_z \tag{A.40}$$

with boundary conditions

$$A_v^0 u_z^1 = -(A_v^0 u_z^0)_z \zeta^0 \qquad \text{at } z = R \tag{A.41}$$
$$A_v^0 u_z^1 = s_f^0 u^1 \qquad \text{at } z = -H \tag{A.42}$$

Since the leading order terms already can be solved with the leading order equations, the only unknowns in the first order equation are u^1, w^1 and ζ^1. Rewriting the first order equation such that known 'forcing' terms are on the right hand side gives:

$$u_t^1 + g\zeta_x^1 - (A_v u_z^1)_z = -(u^0 u_x^0 + w^0 w_z^0) - g\int_z^R \frac{\rho_x}{\rho_0} dz \tag{A.43}$$

By substituting the power series into Equation 2.7, the leading-order depth-averaged continuity equation reads

$$\zeta_t^0 + \frac{1}{B}\left(B\int_{-H}^R u^0 dz\right)_x = 0 \tag{A.44}$$

with boundary conditions

$$\zeta^0 = A^0 \qquad \text{at } x = 0 \tag{A.45}$$
$$B\int_{-H}^R u^0 dz = -Q^0 \qquad \text{at } x = L \tag{A.46}$$

Using the same approach, the first-order depth-averaged continuity equation can be formulated as

$$\zeta_t^1 + \frac{1}{B}\left(B\int_{-H}^R u^1 dz + B u_{z=R}^0 \zeta^0\right)_x = 0 \tag{A.47}$$

for which the following boundary conditions apply

$$\zeta^1 = A^1 \qquad \text{at } x = 0 \tag{A.48}$$
$$B\int_{-H}^R u^1 dz = -Q^1 - B u_{z=R}^0 \zeta^0 \qquad \text{at } x = L \tag{A.49}$$

A.4. TYPICAL FORCING

By making certain assumptions about the external forcing (tides and river discharge), the solutions of these equations become well-analysable. At first we restrict the external forcing to only consist of a subtidal signal and a semi-diurnal signal plus corresponding overtimes. Secondly, we assume that the only forcing at leading-order is an M_2 tidal constituent. Thirdly, the first-order hydrodyanmics forced by an M_4 tidal constituent (approximated to be of $\mathcal{O}(\epsilon)$). And finally, the river discharge is assumed to only appear at first-order as well.

Due to these assumptions, the leading-order velocity can be described with the M_2 velocity component, which can be written as:

$$u^0 = \hat{u}^0 \cos(\sigma t) \tag{A.50}$$

with $\sigma = \frac{2\pi}{T}$

Furthermore, we assumed that the external forcing for the first-order hydrodynamics are described by the river discharge and an M_4 tidal constituent. The rewritten form of the first-order equation (see Equation A.43) however shows that the first-order hydrodynamics also depend on the leading-order advection and a baroclinic pressure. By substituting the known leading-order velocity u^0 into this first- order solution, the advection part can be written as

$$u^0 \cdot u^0 = \left(\hat{u}^0\right)^2 \cos^2(\sigma t) \tag{A.51}$$

Which can be rewritten by making use of the trigonometric identities as

$$\left(\hat{u}^0\right)^2 \cos^2(\sigma t) = \left(\hat{u}^0\right)^2 \frac{1}{2}(\underbrace{1}_{\text{M0}} + \underbrace{cos(2\sigma t)}_{\text{M4}}) \tag{A.52}$$

Now it can be seen, that once the leading order velocity only depends on the M2 tidal signal, the advection term contains a subtidal (M_0) and a M_4 dependency, hence the entire first-order hydrodynamics can be described with a subtidal (M_0) and a M_4 signal. This analysis can be extended for second, third and higher orders in the same way, but that is out of the scope of this report and is therefore not presented here.

B

SEDIMENT DYNAMICS

Since the model will be used to evaluate sediment concentrations within the Loire estuary, the sediment dynamic equations will be elaborated as well. The governing equations are already presented in chapter 2. This appendix elaborates on the perturbation approach. At first, the scaling of the equations is presented. Secondly, leading-order and first-order equations are derived. And finally, derivations regarding the typical forcing of the sediment dynamics are discussed. This appendix provides additional information to chapter 2, and should not be read on its own.

B.1. SCALING

B.1.1. OVERVIEW OF PARAMETERS

A mathematical scaling analysis will be used to identify the importance of the individual terms in the equations. For this purpose, the equations need to be transformed to a dimensionless system which can be done using scaling arguments. Typical scales (of parameters present in the equations) are presented in Table B.1

Table B.1: Typical scales of individual parameters

Scale		Dimensionless quantity
T_{M2}	M_2 tidal period	$t = T_{M2}\, t^*$
A_{M2}	M_2 tidal amplitude at the seaward side	$\zeta = A_{M2}\zeta^*$
H_0	Average depth at seaward side	$z = H_0 z^*$ and $R = A_{M2}R^*$
L_{tide}	Tidal wave length	$x = L_{tide}x^*$ for u_x, w_x, ζ_x
L_{conv}	Convergence length	$x = L_{conv}x^*$ for H_x, B_x
$\mathscr{R}_x$	Typical density gradient	$\rho_x = \mathscr{R}_x \rho^*_{x^*}$

To get a feeling about the magnitude of the different parameters, a list with typical values for the Loire estuary is presented in Table B.2.

Table B.2: Typical values of physical parameters in the Loire Estuary. Typical value for w_s has been based on Walther et al. (2012).

Parameter	Typical value	Typical Order
T_{M2}	44712 s	$\mathcal{O}(10^4)$
σ_{M2}	$(1/44712)$ s^{-1}	$\mathcal{O}(10^{-4})$
L_{tide}	100km = 10^5m	$\mathcal{O}(10^5)$
A_{M2}	1 m	$\mathcal{O}(1)$
H_0	10-20 m	$\mathcal{O}(10)$
ρ	1000-1030 kg/m^3	$\mathcal{O}(10^3)$
ρ_s	2650 kg/m^3	$\mathcal{O}(10^3)$
w_s	$2 \cdot 10^{-3}$m/s	$\mathcal{O}(10^{-3})$
g	9.81 m/s^2	$\mathcal{O}(10)$
$U \sim \frac{A_{M2}L}{T(H_0+A_{M2})}$	1 m/s	$\mathcal{O}(1)$

With these typical scales, scales of other parameters can be derived.

Table B.3: Derived scales for parameters in sediment equation

Derived Scale		Dimensionless quantity
$C = \frac{\rho_s \mathscr{A}_v U a_\star}{H_0 g' d_s}$	Typical sediment concentration	$c = Cc^*$
$a_\star$	Typical amount of available sediment	$a = a_\star a^*$
$\mathscr{K}_v = \mathscr{A}_v = \frac{\sigma H_0^2}{\lambda^2}$	Typical vertical eddy diffusivity	$K_v = \mathscr{K}_v K_v^*$
$\mathscr{K}_h = \sigma L^2 \left(\frac{A_{M2}}{H_0}\right)^2$	Typical horizontal eddy diffusivity	$K_h = \mathscr{K}_h K_h^*$

B.1.2. WIDTH-AVERAGED SEDIMENT MASS BALANCE

Making dimensionless in a similar way as is done for the momentum equation:

$$\frac{C}{T}c^*_{t^*} + \frac{UC}{L_{tide}}u^* c^*_{x^*} + \frac{WC}{H}w^* c^*_{z^*} = \frac{C}{H}w_s c^*_{z^*} + \frac{\mathscr{K}_h C}{L^2_{tide}}(K^*_h c^*_{x^*})_{x^*} + \frac{\mathscr{K}_h C}{L^2_{tide}}\frac{B^*_{x^*}}{B^*}K^*_h c^*_{x^*} + \frac{\mathscr{K}_v C}{H^2}(K^*_v c^*_{z^*})_{z^*} \tag{B.1}$$

Divide by $\frac{C}{T}$

$$c^*_{t^*} + \frac{UT}{L_{tide}}u^* c^*_{x^*} + \frac{WT}{H}w^* c^*_{z^*} = \frac{T}{H}w_s c^*_{z^*} + \frac{\mathscr{K}_h T}{L^2_{tide}}(K^*_h c^*_{x^*})_{x^*} + \frac{\mathscr{K}_h T}{L^2_{tide}}\frac{B^*_{x^*}}{B^*}K^*_h c^*_{x^*} + \frac{\mathscr{K}_v T}{H^2}(K^*_v c^*_{z^*})_{z^*} \tag{B.2}$$

Substituting the expressions for U and W (presented in Equation A.10 & Equation A.13) into Equation B.2 and using $\sigma = \frac{1}{T}$ results in:

$$c^*_{t^*} + \frac{A_{M2}}{H_0}(u^* c^*_{x^*} + w^* c^*_{z^*}) = \frac{w_s \sigma}{H}c^*_{z^*} + \frac{\mathscr{K}_h T}{L^2_{tide}}(K^*_h c^*_{x^*})_{x^*} + \frac{\mathscr{K}_h T}{L^2_{tide}}\frac{B^*_{x^*}}{B^*}K^*_h c^*_{x^*} + \frac{\mathscr{K}_v T}{H^2}(K^*_v c^*_{z^*})_{z^*} \tag{B.3}$$

Substituting the expressions for $\mathscr{K}_v$ and $\mathscr{K}_h$ presented in Table B.3 into Equation B.3 results in the next equation in which the order of most of the terms can be easily recognised:

$$\underbrace{c^*_{t^*}}_{\mathscr{O}(1)} + \underbrace{\frac{A_{M2}}{H_0}(u^* c^*_{x^*} + w^* c^*_{z^*})}_{\mathscr{O}(\epsilon)} = \underbrace{\frac{w_s \sigma}{H}c^*_{z^*}}_{\mathscr{O}(?)} + \underbrace{\left(\frac{A_{M2}}{H_0}\right)^2 (K^*_h c^*_{x^*})_{x^*}}_{\mathscr{O}(\epsilon^2)} + \underbrace{\left(\frac{A_{M2}}{H_0}\right)^2 \frac{B^*_{x^*}}{B^*}K^*_h c^*_{x^*}}_{\mathscr{O}(\epsilon^2)} + \underbrace{\frac{1}{\lambda^2}(K^*_v c^*_{z^*})_{z^*}}_{\mathscr{O}(?)} \tag{B.4}$$

Using the typical orders of magnitude of the physical parameters governing in the Loire estuary, a rough estimate of the order can be made for the term $\frac{w_s}{\sigma H_0}$ as is done below:

$$\frac{w_s}{\sigma H_0} \sim \frac{\mathscr{O}(10^{-3})}{\mathscr{O}(10^{-4})\mathscr{O}(10)} = \mathscr{O}(1) \tag{B.5}$$

The same procedure can be repeated for the last unknown term:

$$\lambda \approx \frac{\sigma L}{\sqrt{g H_0}} \sim \frac{c_E}{c_E} = \mathscr{O}(1) \tag{B.6}$$

The latter is logical, since $\sigma \cdot L$ is an expression for the tidal wave velocity. The term in the numerator ($\sqrt{g H_0}$) is also recognised as an expression for the tidal velocity in shallow water, so in shallow water λ is approximately 1.

Now the order of all terms is known, the equation for the sediment concentration can be written as

$$\underbrace{c_t}_{\mathscr{O}(1)} + \underbrace{uc_x}_{\mathscr{O}(\epsilon)} + \underbrace{wc_z}_{\mathscr{O}(\epsilon)} = \underbrace{w_s c_z}_{(\mathscr{O}(1))} + \underbrace{(K_h c_x)_x}_{\mathscr{O}(\epsilon^2)} + \underbrace{\frac{B_x}{B}K_h c_x}_{\mathscr{O}(\epsilon^2)} + \underbrace{(K_v c_z)_z}_{\mathscr{O}(1)} \tag{B.7}$$

BOUNDARY CONDITIONS

The boundary conditions, which are presented by Equation 2.24 and Equation 2.25, can be written in a dimensionless form. At first, the dimensionless boundary condition at the surface $z = R + \zeta$ is derived

$$C w_s c^* + \frac{C\mathcal{K}_v}{H_0} K_v^* c_{z^*}^* - \frac{\mathcal{K}_h C A_{M2}}{L_{tide}^2} K_h^* c_{x^*}^* \zeta_{x^*}^* = 0 \tag{B.8}$$

If we then substitute the expressions for $\mathcal{K}_v$ and $\mathcal{K}_h$ from Table B.3 into the equation, we end up with:

$$C w_s c^* + \frac{C\sigma_{M2} H_0^2}{\lambda^2 H_0} K_v^* c_{z^*}^* - \frac{\sigma_{M2} L_{tide}^2 \left(\frac{A_{M2}}{H_0}\right)^2 C A_{M2}}{L_{tide}^2} K_h^* c_{x^*}^* \zeta_{x^*}^* = 0 \tag{B.9}$$

And by dividing all terms by $C\sigma_{M2} H_0$, the dimensionless boundary condition after simplifying reads

$$\underbrace{\frac{w_s}{\sigma_{M2} H_0}}_{\mathcal{O}(1)} c^* + \underbrace{\frac{1}{\lambda^2}}_{\mathcal{O}(1)} K_v^* c_{z^*}^* - \underbrace{\left(\frac{A_{M2}}{H_0}\right)^3}_{\mathcal{O}(\epsilon^3)} K_h^* c_{x^*}^* \zeta_{x^*}^* = 0 \tag{B.10}$$

in which the typical orders of magnitudes are found using Equation B.5 and Equation B.6.

The same can be done for the boundary condition near the bed, but first some assumptions about the scaling of the erosion term should be introduced. By combining Equation 2.26 and Equation 2.27, the erosion term can be expressed as

$$E = M|\rho_0 A_v u_z| f(a(x)) \tag{B.11}$$

in which the erosion parameter M is assumed to be of $\mathcal{O}(10^{-4})$ and the erodibility is approximated by:

$$f(a(x)) \sim \int_{-H}^{0} c\,dz \sim H_0 C z^* c^* \tag{B.12}$$

Using these expression for the erosion term, the boundary condition near the bed can be rewritten into a dimensionless form

$$\frac{\mathcal{K}_v C}{H_0} K_v^* c_{z^*}^* - \frac{\mathcal{K}_h C H_0}{L_{tide}^2} K_h^* c_{x^*}^* H_{x^*}^* = \frac{M\rho_0 \mathcal{A}_v U C H_0}{H_0} M^* * A_v^* u_{z^*}^* f^* \tag{B.13}$$

By dividing by $\mathcal{K}_v C / H_0$ and substituting the expressions for $\mathcal{K}_v$ and $\mathcal{K}_h$ from Table B.3, the following typical orders of magnitude are found for the terms in the sediment concentration equilibrium condition

$$\underbrace{K_v^* z_{z^*}^*}_{\mathcal{O}(1)} - \underbrace{\left(\frac{A_{M2}}{H_0}\right) \lambda^2 K_h^* c_{x^*}^* H_{x^*}^*}_{\mathcal{O}(\epsilon^2)} = \underbrace{\rho_0 M U H_0 M^* \rho_0^* A_v^* u_{z^*}^* f^*}_{\mathcal{O}(1)} \tag{B.14}$$

B.1.3. CONCENTRATION EQUILIBRIUM CONDITION

In subsection 2.3.2, we already concluded that either f_a should equal zero, or the sum of the tidally averaged advective and diffusive transport is divergence free with respect to x near the landward boundary. The derivative of f with respect to a equals zero for relatively large sediment stock (see Figure 2.2), which is unlikely to happen at the landward boundary, hence the other condition is governing and the terms outside the angle brackets can be omitted. If we then assume that the sediment influx from the river equals zero, which is the reasonable for this research, we know that not only the derivative of the total transport equals zero in x direction, but the transport itself as well. By leaving out the derivative to x, and omitting the constants outside the angle brackets, the sediment concentration equilibrium condition in a non-dimensional form reads

$$\left\langle \int_{-H^*}^{R^*+\epsilon\zeta^*} (\underbrace{U}_{\mathcal{O}(\epsilon)} u^* c^* - \underbrace{\frac{\mathcal{K}_h}{L_{tide}}}_{\mathcal{O}(\epsilon^2)} K_h^* c_{x^*}^*) d\tilde{z} \right\rangle = 0 \tag{B.15}$$

Note that B has been left out the equation as well, which can be done since $b \neq 0$ and hence the integral should equal zero.

B.2. ORDERING

By substituting the power series for u, w, ζ and c in the equations derived before as well, sets of equations at leading-order and first order are found using the typical orders of magnitude of the different terms:

$$c_t^0 - w_s^0 c_z^0 - (K_v^0 c_z^0)_z = 0 \tag{B.16}$$

with boundary conditions (linearised around the reference level R)

$$w_s^0 c^0 + K_v^0 c_z^0 = 0 \qquad \text{at } z = R \tag{B.17}$$

$$K_v^0 c_z^0 = E^0 \qquad \text{at } z = -H \tag{B.18}$$

At first order we find the governing equation

$$c_t^1 - w_s^0 c_z^1 - (K_v^0 c_z^1)_z = -(u^0 c_x^0 + w^0 c_z^0) + w_s^1 c_z^0 \tag{B.19}$$

with boundary conditions (linearised around the reference level R)

$$w_s^0 c^1 + K_v^0 c_z^1 = -(w_s^0 c^0 + K_v^0 c_z^0)_z \zeta^0 \qquad \text{at } z = R \tag{B.20}$$

$$K_v^0 c_z^1 = -E^1 \qquad \text{at } z = -H \tag{B.21}$$

B.3. TYPICAL FORCING

Both the leading-order and first-order sediment concentrations are forced by an erosive term. The erosion in turn depends on the bottom shear stress, of which the magnitude can be approximated using a power series for u (restricted to first order)

$$\begin{aligned}
|\tau_b| &= \rho_0 s_f |u| = \rho_0 s_f \sqrt{(u^0 + u^1)^2} \\
&= \rho_0 s_f \sqrt{(u^0)^2 + 2u^0 u^1 + \underbrace{(u^1)^2}_{=\mathcal{O}_{\epsilon^2}}} \\
&\approx \rho_0 s_f \sqrt{(u^0)^2 + 2u^0 u^1} \\
&= \rho_0 s_f |u^0| \sqrt{1 + 2\frac{u^1}{u^0}} \\
&\approx \rho_0 s_f |u^0| + \rho_0 s_f \frac{|u^0|}{u^0} u^1 = \underbrace{\rho_0 s_f |u^0|}_{\mathcal{O}(1)} + \underbrace{\rho_0 s_f \mathrm{sg}(u^0) u^1}_{\mathcal{O}(\epsilon)}
\end{aligned}$$

in which the last approximation was obtained using a Taylor expansion. So, we can rewrite the expression for the leading- and first-order erosion as

$$E^0 = M|u^0| f(a(x)) \tag{B.22}$$

$$E^1 = M s g(u^0) u^1 f(a(x)) \tag{B.23}$$

in which the unknown terms in the expressions are $|u^0|$ and $\mathrm{sg}(u^0)u^1$. These terms can be approximated with a Fouries series, which is done in Appendix C.

C

FOURIER SERIES

Each periodic signal can be represented by a weighted sum of simple sines and cosines. This way of representation is called a Fourier series. A general formulation of such a Fourier series for an arbitrary function f(t) on the interval $[-\pi, \pi]$ is given below

$$f(t) \sim \frac{1}{2}a_0 + \sum_{n=1}^{N} [a_n \cos(nt) + b_n \sin(nt)] \tag{C.1}$$

with

$$a_0 = \frac{1}{\pi}\int_{-\pi}^{\pi} f(t)dt \tag{C.2}$$

$$a_n = \frac{1}{\pi}\int_{-\pi}^{\pi} f(t)\cos(nt)dt \tag{C.3}$$

$$b_n = \frac{1}{\pi}\int_{-\pi}^{\pi} f(t)\sin(nt)dt \tag{C.4}$$

Now, we would like to evaluate $|u^{02}|$ and $\mathrm{sg}(u^{02})$, since the M2 tidal velocity is dominating the leading order velocities. The tidal velocity belonging to the M2 component can be written as $u^{02} = \hat{u}^{02}\cos(\sigma t)$. In terms of the general formulation of the Fourier series mentioned before, $f(t)$ becomes either $|u^{02}|$ or $\mathrm{sg}(u^{02})$. Both expressions will be evaluated in the following sections.

C.1. $|u^{02}|$

A Fourier series will be determined for the absolute value of the M2 tidal velocity component, with other words

$$f(t) = |u^{02}| = |\hat{u}^{02}\cos(\sigma t)| = |\hat{u}^{02}||\cos(\sigma t)| \tag{C.5}$$

Since the cosine function is an even function, the coefficient b_n is zero. The coefficients a_0 and a_n are calculated as follows

$$a_0 = \frac{1}{\pi}\int_{-\pi}^{\pi} |\hat{u}^{02}\cos(t)|dt \tag{C.6}$$

$$a_n = \frac{1}{\pi}\int_{-\pi}^{\pi} |\hat{u}^{02}\cos(t)|\cos(nt)dt \tag{C.7}$$

Note: σt is replaced by t only, for the sake of simplicity.

Making use of the fact that the cosine is symmetric around the y-axis (even function) and the fact that the sign of the cosine changes at $\pi/2$ as described in Equation C.8, makes it possible to rewrite these expressions.

$$|\cos(x)| = \begin{cases} \cos(x) & \text{for } 0 \le x \le \pi/2 \\ -\cos(x) & \text{for } \pi/2 \le x \le \pi \end{cases} \tag{C.8}$$

$$a_0 = \frac{2}{\pi}\int_0^{\pi/2} |\hat{u}^{02}|\cos(t)\,dt - \frac{2}{\pi}\int_{\pi/2}^{\pi} |\hat{u}^{02}|\cos(t)\,dt = 0 \tag{C.9}$$

$$a_n = \frac{2}{\pi}\int_0^{\pi/2} |\hat{u}^{02}|\cos(t)\cos(nt)\,dt - \frac{2}{\pi}\int_{\pi/2}^{\pi} |\hat{u}^{02}|\cos(t)\cos(nt)\,dt \tag{C.10}$$

Equation C.10 can be evaluated by making use of the trigonometric identity given in Equation C.11

C

$$\cos(u)\cdot\cos(v) = \frac{1}{2}\left[\cos(u-v)+\cos(u+v)\right] \tag{C.11}$$

Resulting in (after rewriting (t-nt) as ((1-n)t) and (t+nt) as ((1+n)t))

$$a_n = \frac{2}{\pi}|\hat{u}^{02}|\left(\int_0^{\pi/2}\frac{1}{2}[\cos((1-n)t)+\cos((1+n)t)]\,dt - \int_{\pi/2}^{\pi}\frac{1}{2}[\cos((1-n)t)+\cos((1+n)t)]\,dt\right) \tag{C.12}$$

Integrating results in

$$a_n = \frac{1}{\pi}|\hat{u}^{02}|\left(\left[\frac{\sin((1-n)t)}{(1-n)}+\frac{\sin((1+n)t)}{(1+n)}\right]_0^{\pi/2} - \left[\frac{\sin((1-n)t)}{(1-n)}+\frac{\sin((1+n)t)}{(1+n)}\right]_{\pi/2}^{\pi}\right) \tag{C.13}$$

Working out the integration results in

$$a_n = \frac{1}{\pi}|\hat{u}^{02}|\left(\left[\left(\frac{\sin((1-n)\frac{\pi}{2})}{(1-n)}+\frac{\sin((1+n)\frac{\pi}{2})}{(1+n)}\right)-(0)\right] - \left[(0)-\left(\frac{\sin((1-n)\frac{\pi}{2})}{(1-n)}+\frac{\sin((1+n)\frac{\pi}{2})}{(1+n)}\right)\right]\right) \tag{C.14}$$

Rewriting the equation gives

$$a_n = \frac{1}{\pi}|\hat{u}^{02}|\left(\left[\left(\frac{\sin(\frac{\pi}{2}-\frac{\pi n}{2})}{(1-n)}+\frac{\sin(\frac{\pi}{2}+\frac{\pi n}{2})}{(1+n)}\right)\right] - \left[-\left(\frac{\sin(\frac{\pi}{2}-\frac{\pi n}{2})}{(1-n)}+\frac{\sin(\frac{\pi}{2}+\frac{\pi n}{2})}{(1+n)}\right)\right]\right) \tag{C.15}$$

Again rewriting and making use of the fact that $sin(\frac{\pi}{2}-t) = \cos(t)$ makes this equation already much easier

$$a_n = \frac{1}{\pi}|\hat{u}^{02}|\left(\left[\frac{(1+n)\cos(-\frac{\pi n}{2})+(1-n)\cos(\frac{\pi n}{2})}{(1-n^2)}\right] + \left[\frac{(1+n)\cos(-\frac{\pi n}{2})+(1-n)\cos(\frac{\pi n}{2})}{(1-n^2)}\right]\right) \tag{C.16}$$

Final step is making use of the symmetry of the cosine around the y-axis and adding equal terms together

$$a_n = \frac{1}{\pi}|\hat{u}^{02}|\left(\frac{4}{(1-n^2)}\cos(\frac{\pi n}{2})\right) \tag{C.17}$$

For n=1,3,5 ... we find that the expression for a_n is zero, whereas the expression is nonzero for n=0,2,4 and so on. Since we are trying to write the absolute value of the M2 tidal velocity as a sum of other cosines, we are only interested in the multiples of the M2 tide. From this we can conclude, that for the leading order erosion $\hat{E}^0$, the residual M_0 (n=0) and M_4 (n=2) are the relevant forcings.

C.2. SIGN(u^{02})

A Fourier series is used to estimate the sign function of the M2 tidal velocity component:

$$f(t) = \mathrm{sg}(u^{02}) = \frac{|u^{02}|}{u^{02}} = \frac{|\hat{u}\cos(\sigma t)|}{\hat{u}\cos(\sigma t)} \tag{C.18}$$

In a similar way as is done in the preceding section, this term can be estimated using a harmonic decomposition with a Fourier series on the interval $[-\pi,\pi]$. It can be easily seen that a_0 equals zero for the sign function of the cosine. For the coefficient b_n, a graphical analysis has been done of which the result has been depicted in Figure C.1.

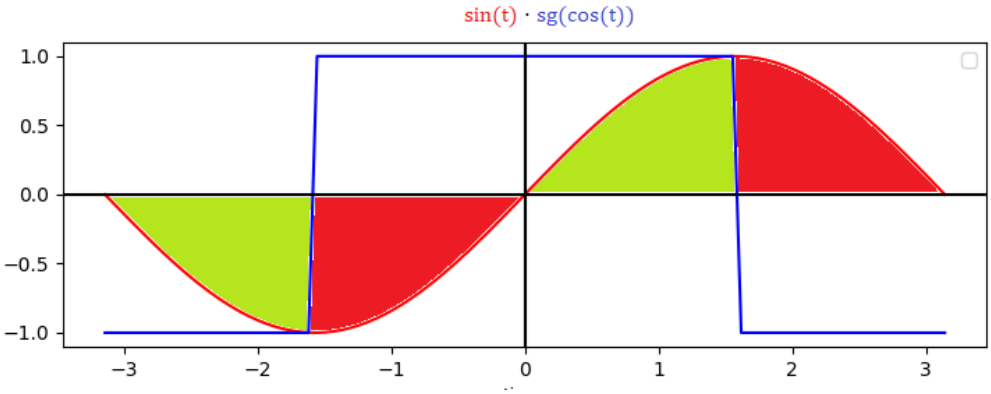

Figure C.1: A graphical analysis of the b_n parameter

A graphical representation of the multiplication of a sine function with the sign function of the cosine is given in Figure C.1. The green areas have a positive contribution to the result whereas the red areas have a negative contribution to the result. It can be easily seen that these areas balance each other, so the parameter b_n becomes zero again. The parameter a_n will be estimated in a similar way as is done in the preceding section.

$$a_n = \frac{1}{\pi}\int_{-\pi}^{\pi} \mathrm{sg}(\hat{u}^{02}\cos(t))\cos(nt)\,dt \tag{C.19}$$

Note: σt is replaced by t only, for the sake of simplicity.
Over the interval [-π, π], the sign-function of the cosine(x) has the following values:

$$\mathrm{sg}(\cos(x)) = \begin{cases} 1 & \text{for } 0 \le \mathrm{x} \le \pi/2 \\ -1 & \text{for } \pi/2 \le \mathrm{x} \le \pi \end{cases} \tag{C.20}$$

Using these typical values, and the symmetry of the sign-function of the cosine(t) around the y-axis the expression for a_n can be rewritten as follows:

$$a_n = \frac{2}{\pi}\int_0^{\pi/2} \mathrm{sg}(\cos(t))\cos(nt)\,dt - \frac{2}{\pi}\int_{\pi/2}^{\pi} \mathrm{sg}(\cos(t))\cos(nt)\,dt \tag{C.21}$$

$$a_n = \frac{2}{\pi}\int_0^{\pi/2} \cos(nt)\,dt - \frac{2}{\pi}\int_{\pi/2}^{\pi} \cos(nt)\,dt \tag{C.22}$$

This expression can be easily integrated:

$$a_n = \frac{2}{\pi}\left(\left[\frac{1}{n}\sin(nt)\right]_0^{\pi/2} - \left[\frac{1}{n}\sin(nt)\right]_{\pi/2}^{\pi}\right) \tag{C.23}$$

Substituting the integration boundaries into the equation gives

$$a_n = \frac{2}{\pi}\left(\left[\frac{1}{n}\sin\left(\frac{n\pi}{2}\right) - \underbrace{\frac{1}{n}\sin(0)}_{=0}\right] - \left[\underbrace{\frac{1}{n}\sin(n\pi)}_{=0} - \frac{1}{n}\sin\left(\frac{n\pi}{2}\right)\right]\right) \tag{C.24}$$

So,

$$a_n = \frac{4}{n\pi}\sin\left(\frac{n\pi}{2}\right) \tag{C.25}$$

From which we recognize that for n=0,2,4 ... this expression equals zero, whereas the expression is non-zero for n=1,3,5 and so on. Since we are trying to write the sign-function of the M2 tidal velocity as a sum of other cosines, we are only interested in the multiples of the M2 tide. From this we can conclude, that for the first-order erosion $\hat{E}^1$, the M_2 (n=1) and M_6 (n=3) are the relevant forcings.

D

COMBINED SENSITIVITY STUDIES

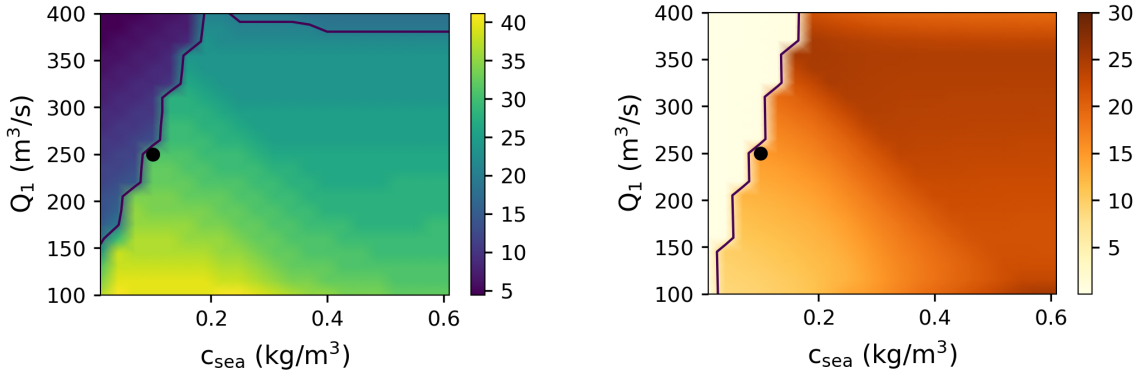

(a) ETM location (km)

(b) Maximum near-bed concentration (kg/m^3)

Figure D.1: Location of the ETM in km from the mouth (a) and the maximum near-bed concentration in kg/m^3 (b) for varying c_{sea} and Q_1, with in black contour lines for 20 km (a) and 5 kg/m^3 (b) and the black dot representing initial values.

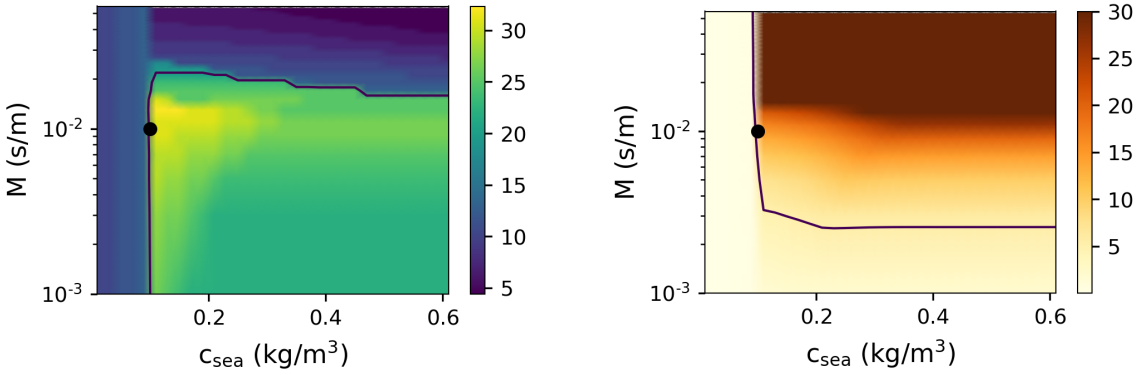

(a) ETM location (km)

(b) Maximum near-bed concentration (kg/m^3)

Figure D.2: Location of the ETM in km from the mouth (a) and the maximum near-bed concentration in kg/m^3 (b) for varying c_{sea} and M, with in black contour lines for 20 km (a) and 5 kg/m^3 (b) and the black dot representing initial values.

E

DEEPENING

Like for neap tidal conditions, an extensive sensitivity study has been performed for spring tidal conditions for decreasing α-values from 1 to 0, and including uncertainty in river discharge, settling velocity and seaward sediment concentration. The results are presented below. Also for spring tide, it can be seen that for every set of parameters, the likelihood to find high sediment concentrations in the Loire estuary increases for increasing depth.

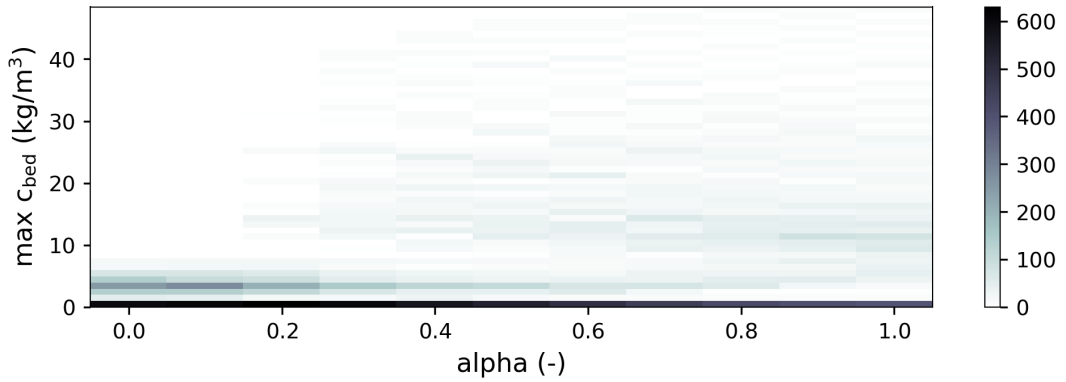

Figure E.1: 2D histogram indicating for every value of alpha (0, 0.1, 0.2 and so on) the number of experiments for which the maximum near-bed sediment fell in a certain range. The bins on the y-axis have a size of 1 g/l.

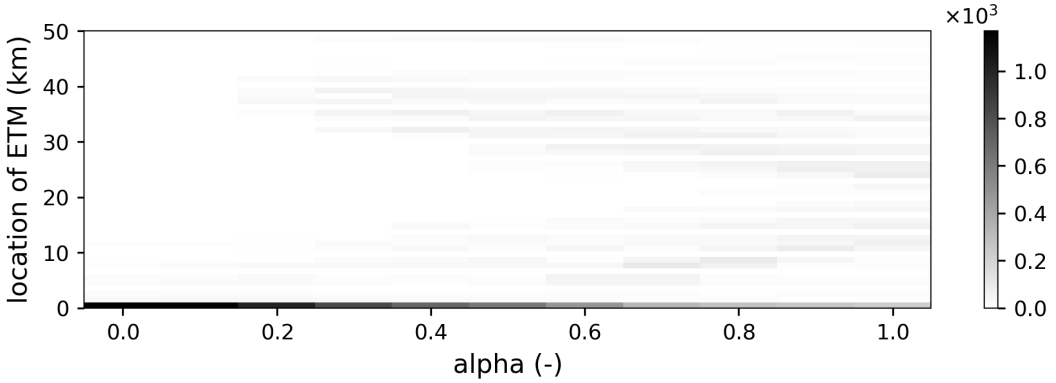

Figure E.2: Number of experiments per value of alpha for which the ETM is located at a certain location. The bins on the y-axis have a size of 1km.

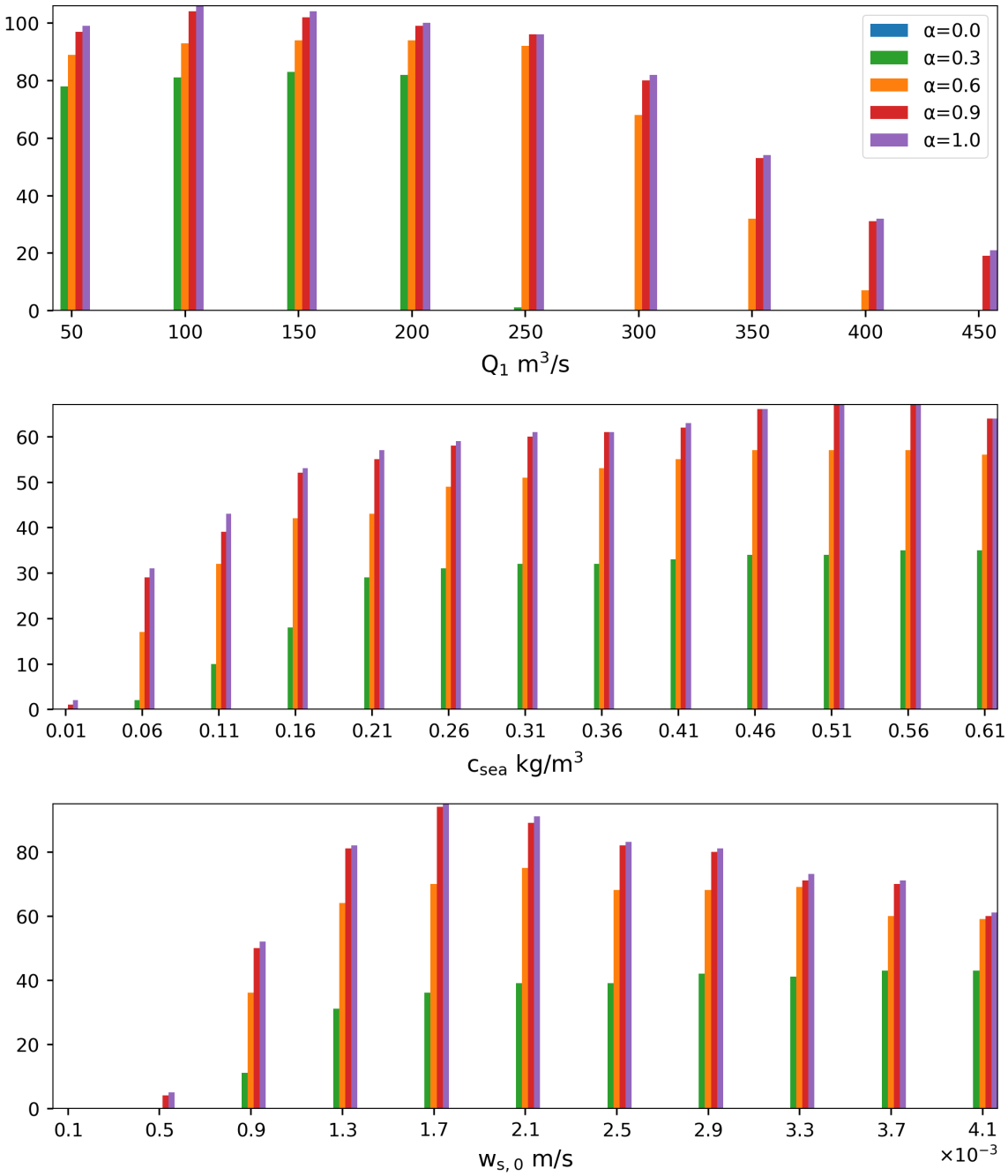

Figure E.3: Number of simulations that have a near-bed sediment concentration larger than 5 g/l between km 25 and 40, sorted for 5 different values of alpha and 3 different input parameters.